Dissertation Advisor: Professor John H. Shaw Amanda Nicole Hughes

# Insights into contractional fault-related folding processes based on mechanical, kinematic, and empirical studies

## Abstract

This dissertation investigates contractional fault-related folding, an important mechanism of deformation in the brittle crust, using a range of kinematic and mechanical models and data from natural structures. Fault-related folds are found in a wide range of tectonic settings, including mountain belts and accretionary prisms. There are several different classes of fault-related folds, including fault-bend, fault-propagation, shear-fault-bend, and detachment folds. They are distinguished by the geometric relationships between the fold and fault shape, which are driven by differences in the nature of fault and fold growth. The proper recognition of the folding style present in a natural structure, and the mechanical conditions that lead the development of these different styles, are the focus of this research. By taking advantage of recent increases in the availability of high-quality seismic reflection data and computational power, we seek to further develop the relationship between empirical observations of fault-related fold geometries and the kinematics and mechanics of how they form. In Chapter 1, we develop an independent means of determining the fault-related folding style of a natural structure through observation of the distribution of displacement along the fault. We derive expected displacements for kinematic models of end-member fault-related folding styles, and validate this approach for natural

structures imaged in seismic reflection data. We then use this tool to gain insight into the deformational history of more complex structures. In Chapter 2, we explore the mechanical and geometric conditions that lead to the transition between fault-bend and fault-propagation folds. Using the discrete element modeling (DEM) method, we investigate the relative importance of factors such as fault dip, mechanical layer strength and anisotropy, and fault friction on the style of structure that develops. We use these model results to gain insight into the development of transitional fault-related folds in the Niger Delta. In Chapter 3, we compare empirical observations of fault-propagation folds with results from mechanical models to gain insight into the factors that contribute to the wide range of structural geometries observed within this structural class. We find that mechanical layer anisotropy is an important factor in the development of different end-member fault-propagation folding styles.

# Contents

# List of Figures

# List of Tables

# Acknowledgements

The completion of this dissertation would not have been possible without the help and support of a great number of people. My advisor, John Shaw, has been a constant source of knowledge and guidance throughout my academic career. Aside from the great deal of wisdom about structural geology that he has imparted to me, I am also grateful for his patience and ability to keep me on task, when my natural instinct is to start working on the next exciting project before finishing the last one. My other current and past committee members, Brendan Meade, Jerry Mitrovica, Rick O'Connell and Jim Rice have been incredible resources and mentors. I will be forever grateful of our many stimulating scientific discussions, and of the generosity with which your shared your time and knowledge with me.

Additionally, I am grateful to the other members of the EPS Department. Special thanks go to Miaki Ishii and Renata Dmowska for their scientific perspectives and kindness. Additionally, I would like to thank the many people who make this department run smoothly, including Chenoweth Moffatt, Maryorie Grande, Alise Usher, Matt Nicholson, Josue Rivera, George Planansky, Paul Kelley, Sarah Colgan, and many others. The department is a warm and active place due to your constant efforts. Additionally, I have found constant inspiration in the many undergraduates that I have taught—I certainly learned as much from you as you did from me.

To my fellow members of the Structural Geology group—Nathan Benesh, Kristian

Bergen, Charlie Brankman, Pauline Durand-Riard, Chris Guzofski, Judith Hubbard, Andreas Plesch, Joe Stockmeyer, Karl Tape, Maomao Wang, Yichuan Li, Mohammed Fahmi, and others who have passed through—I wish to extend my sincerest thanks for all of your insightful discussions, willingness to help on research, and friendship. I would especially like to acknowledge Andreas, who knows how to fix seemingly everything, Charlie, for his sage wisdom and kindness, Nathan, for teaching me everything there is to know about DEM, and Kristian, for always being willing to help think through interesting research problems. Your camaraderie has been one of the biggest parts my time here, and I owe you all a debt of gratitude. And to our many visitors to the group–Julia Morgan, Tom Pratt, Tom Jordan, Frank Bilotti, and John Suppe and others–I have learned an enormous amount from each of you.

As friends, classmates, and colleagues, my fellow graduate students have been an incredible source of support and inspiration. I look forward to continuing the scientific relationships and friendships that I have developed with you. I would especially like to thank the active tectonics group—Eileen Evans, Meredith Langstaff, Phoebe Robinson, and Jack Loveless—you have been like an adopted second group, and I will always remember our great scientific exchanges and friendships. Finally, to the many friends we have made here, especially Allie Gale, Sarah Waterworth, and Megan Kremer, my time in New England has been that much richer because of you.

The Washington and Lee Geology Department played a critical role in my enthusiasm for the field of geology. I truly cherish the lifelong friends I made there–Ryan, Tyler, Amy, Whitney, Brendan, Mike, Barrett, Bill, Julie, Emily, Anne Lindsey, Katie, Erin, and Laura, to name a few—and I am especially grateful to my dedicated professors—Chris Connors, Linda Davis, Dave Harbor, Lisa Greer, Elizabeth Knapp, Ed Spencer, and Fred Schwab—for teaching me so much and for instilling in me their love for geology. I would especially like to thank Chris for his constant willingness to

discuss science and life, and his continued role as a mentor to me.

For the greater part of three decades, my family—my parents, Cheryl and Roger Hughes, my brother, Brad Hughes, my grandparents, Dale and Barbara Hughes, and my dear aunts and uncles, Frank and Diane Adams, Jan and Rob Critchlow, and Wanda and Bob Adams, and cousins, Michelle, Scott, Ava and Evan Jones, Steph and Shawn Gabborin, Stephanie, Tiffany, and Steve Adams—has been an incredible source of loving support, and I can't begin to thank them enough for everything they have done for me. Mom and dad–from driving me to countless practices to teaching me the right way to do things, you have sacrificed so much to help me succeed. My completion of this dissertation never would have been possible without your love and guidance, and I am thankful for you every single day. To my brother–I know I can always count on you for constant encouragement and support–particularly of the technical variety! And to my new family-in-law—Gail, David, Philip, Jenny, Johann and Joeseph Kiser—I am simply blessed to have you in my life. To my many dear friends, who are too numerous to name, but include the Parks, the D'Angelos, the Gallaghers, the Lockes, Kendall, Jenn, Adam, and many others—you have made my life incredibly rich and I am so thankful for your friendship.

To my dearest husband, Eric—words fail to describe how grateful I am of your constant love and support. As we went through the process of getting our degrees together, you have been the calming presence in my life that keeps me balanced. That we can share deep scientific conversations as easily as ones about basketball or dinner plans is a daily blessing. The long nights working and stressful deadlines have been made that much sweeter knowing you were there for me. I can't wait to move on to the next chapter of our lives together.

Finally, I am truly grateful for the opportunity to have completed my Ph.D. here at Harvard—it has been an honor to have shared in the experience with all of you.

# Chapter 1

# Introduction

Field geologists have recognized a genetic relationship between folds and faults since the early 20th century [Rich, 1934; Rodgers, 1950, and others]. Most efforts to understand the development of these structures has focused on characterizing the geometric relationships of the fold and fault shape over time through the development of geometric and kinematic models [Suppe, 1983; Jamison, 1987; Chester and Chester, 1990; Suppe and Medwedeff, 1990; Erslev, 1991; Kattenhorn, 1994; McConnell, 1994; Narr and Suppe, 1994; Erslev and Mayborn, 1997; Spang and McConnell, 1997; Allmendinger, 1998; Suppe et al., 2004; Shaw et al., 2005; Tavani et al., 2006, and others]. These models are based on assumptions of the preservation of cross-sectional area and, in many cases, layer thickness, throughout the deformation process. Thus, they are viewed to be valid first-order descriptions of folding related to fault displacements. While these models imply certain deformational processes (e.g., layer-parallel, or flexural, slip, penetrative shear, and localized shear), they are inherently geometric, and do not explicitly consider rock mechanics. As a result, some recent studies have focused on numerical modeling of the mechanics of deformation and comparing the resulting structures with kinematic models and natural structures in order to assess the role of mechanics in the fault-related folding process [Smart et al., 1999; Erickson

et al., 2001; Cardozo et al., 2003, 2005; Hardy and Finch, 2005, 2006; Benesh et al., 2007; Hardy and Finch, 2007; Benesh, 2010]. Motivated by field-based observations [Julian and Wiltschko, 1983; Morley, 1986; Woodward et al., 1988; Woodward and Rutherford Jr, 1989; Fischer and Jackson, 1999; Spratt et al., 2004] these studies have begun to explore the correlations between mechanical variations in rock type and stratigraphic layer thickness with changes in fault-related folding style.

There are a number of applications for which the proper identification of fault-related folding style is critically important. For example, assessment of the seismic hazard risk posed by thrust and reverse faults, including blind thrust faults, generally relies on the ability to relate uplift and folding that may be observed at the Earth's surface to fault geometry and slip at depth [Shaw and Suppe, 1994; Allmendinger and Shaw, 2000; Pratt et al., 2002; Shaw et al., 2002; Dolan et al., 2003; Yue et al., 2005; Gold et al., 2006; Yue et al., 2005, and others]. This requires a model relating fold geometry to fault geometry and slip, and the choice of the appropriate model is dependent on proper identification of the fault-related folding style. As uplift and slip are related in very different ways in each fault-related folding style [Hardy and Poblet, 2005], this choice has an important impact on the seismic hazard that is inferred for the structure.

An accurate assessment of structural style is also essential to the study of petroleum systems [e.g., Rowan and Linares, 2009; Corredor et al., 2005a; Shaw et al., 2005, and others]. Contractional fault-related folds are the most common type of structural trap in the world. Application of the most appropriate fault-related folding model to a structure can help to infer fold and fault geometries where data coverage is incomplete, reducing uncertainty in the estimation of reservoir volumes. The relative timing of fault and fold formation may also have important implications for the availability of charge pathways at the times of hydrocarbon maturation and migration. Finally, fold

and fault geometries, and how they evolve over time, dictate the distribution of strain (e.g., fractures, shear bands, secondary faults) throughout the stratigraphic sequence, which has important implications for reservoir permeability and seal integrity.

Finally, fault-related folding models are used to build balanced cross-sections in regional geologic studies that seek to define the timing and magnitudes of crustal deformation along convergent plate margins [for example, Zapata and Allmendinger, 1996]. Thus, the accuracy of tectonic interpretations and shortening estimates for fold-and-thrust belts depends on the proper application of fault-related folding models, as the different structural styles can accommodate vastly different amounts of shortening.

Motivated by this array of applications, the goal of our research is to develop an improved understanding of the geometry, kinematics, and mechanics of fault-related folds through empirical studies and mechanical models. For our mechanical modeling studies, we use the discrete element method (DEM). While this method is commonly applied in other disciplines, including granular mechanics, engineering, and material science, it has only recently been applied to large-scale geologic problems [Burbridge and Braun, 2002; Strayer and Suppe, 2002; Finch et al., 2003, 2004; Strayer et al., 2004; Hardy and Finch, 2005; Morgan and McGovern, 2005a,b; Hardy and Finch, 2006; Seyferth and Henk, 2006; Hardy and Finch, 2007; Hardy et al., 2009]. We chose this technique because it is well-suited to modeling high strains and the development of emergent localization during the deformation process without the complications inherent to other continuum methods.

In the first part of this dissertation (Chapter 2), we seek to develop an objective method of determining fault-related folding styles based on analysis of both kinematic models and natural structures from around the world. Our detailed analysis of natural structures is made possible by recent advances in the acquisition and processing of

seismic reflection datasets, which provide precise images of structural geometry and fault displacements that can be used to characterize fault-related folding styles. We determine the distribution of displacement along fault surfaces that is predicted by kinematic models of fault-bend, shear fault-bend, and fault-propagation folds, finding that the different kinematic models are characterized by distinct trends in displacement. We compare these predictions with examples of natural structures imaged in seismic reflection data and observe that the modeled characteristic displacement gradients are observed in natural structures. Based on this insight, we apply this method to a more complex set of natural structures and show that characterization of displacement patterns can be used to decipher complex, hybrid growth histories involving components of different fault-related folding styles. We anticipate that our method of displacement-distance analysis for fault-related folds will prove to be a useful tool in relating the observed distribution of displacement for natural structures to the structural style. This will help provide the justification for choosing the most appropriate kinematic model, thereby reducing uncertainties in the modeling of these structures for seismic hazard, petroleum, and regional tectonics applications.

While the role of specific mechanical and geometric factors have been examined in previous analog and numerical modeling studies, the relative importance of a range of factors in the transition between structural styles has not been investigated. We make use of the recent dramatic increase in computational power to run a large suite of discrete-element mechanical (DEM) models of contractional fault-related folds in order to investigate systematically the role of mechanics in the transition between fault-bend and fault-propagation folding (Chapter 3). We specifically test the effect of fault dip, fault friction, bulk material strength, material anisotropy, and boundary conditions on the style structural deformation that results. Detailed studies of distortion in the resulting models provide insight into the mechanisms by which the

deformation in the different models accommodates the strain, and how these patterns are related to the fault-related folding style that develops. We find that fault friction and boundary conditions are the most important factors that favor the development of either fault-bend or fault-propagation folds, the two most common classes of structures in fold-and-thrust belts. Fault dip, mechanical layer spacing, and the degree of mechanical layer anisotropy play important roles as well, while other factors (e.g., bulk strength) have a negligible impact on the resulting style of deformation. Based on these insights, we interpret two transitional structures in the Niger Delta, inferring that their observed hybrid structural styles are related to low mechanical anisotropy, high fault dip, and geometric limitation of activity of the upper detachment due to the interference of a structure to the foreland. Our assessment of the relative importance of different mechanical and geometric properties on the development of fault-bend and fault-propagation folds should provide insight into the interpretation of structural style, stratigraphic properties, or fault dip in locales where these factors are only partially known. Additionally, we hope that our findings on transitional fault-related folds may provide a context for interpreting the factors that led to the development of these structures.

Motivated by the wide range of geometries observed in natural examples of fault-propagation folds, we then focus on comparing empirical observations of these structures with kinematic and mechanical models in an effort to gain insight into the potential causes of the observed natural variability (Chapter 4). By taking advantage of the availability of high-quality seismic reflection data, we make detailed empirical measurements of a series of natural fault-propagation folds, finding that in spite of the wide range of geometric variability, trends in displacement gradient and displacement/structural relief relationships are robust amongst the range of structures observed. We construct discrete-element models of fully emergent fault-propagation

folds and find that the degree of mechanical layer anisotropy in the model is directly related to the resulting geometry of the fault-propagation fold that develops; isotropic models tend to form structures consistent with the trishear model, while strongly anisotropic models tend to form structures more consistent with kink-style models such as fixed-axis and constant-thickness fault-propagation folds. We conclude that mechanical layer anisotropy may be a significant contributor to the range of geometries observed in this class of structures. We anticipate that our empirical observations of fault slip and uplift relationships, and the consistency of displacement-distance relationships for fault-propagation folds may prove useful in relating uplift rates to slip rates on active structures. Additionally, we hope that our observation that mechanical strength anisotropy largely dictates the development of specific fault-propagation folding geometries will allow for a justification of the application of a particular kinematic model in seismic hazard and petroleum applications where independent constraints on rock properties are known.

# Chapter 2

# Fault Displacement-Distance Relationships as Indicators of Contractional Fault-related Folding Style

## 2.1 Abstract

We present a method of using fault displacement-distance profiles to distinguish fault-bend, shear fault-bend, and fault-propagation folds, and use these insights to guide balanced and retrodeformable interpretations of these structures. We first describe the displacement profiles associated with different end-member fault-related folding models, then provide examples of structures that are consistent with these model-based predictions. Natural examples are imaged in high resolution 2- and 3-D seismic reflection datasets from the Niger Delta, Sichuan Basin, Sierras Pampeanas, and Cascadia to record variations in displacement with distance updip along faults (termed distance-displacement profiles). Fault-bend folds exhibit constant displacement along fault segments and changes in displacement associated with bends in faults, shear fault-bend-folds show an increase in displacement through the shearing interval, and fault-propagation folds exhibit decreasing displacement toward the fault

tip. More complex structures are then investigated using this method, demonstrating that displacement-distance profiles can be used to provide insight into structures that involve multiple fault-related folding processes or have changed kinematic behavior over time. These interpretations are supported by comparison with the kinematics inferred from the geometry of growth strata overlying these structures. Collectively, these analyses illustrate that the distance-displacement approach can provide valuable insights into the styles of fault-related folding.

## 2.2 INTRODUCTION

The ability to classify the structural style of a fault-related fold is essential to many different applications. Understanding the kinematic history of fault-related folds can provide important constraints on the geometry and evolution of traps in petroleum geology. Similarly, various fault-related fold models make different predictions about rock strains that may affect reservoir properties. Moreover, properly characterizing fault-related folds can also be an important aspect of seismic hazard assessment. Various fault-related folding models predict characteristic relationships between uplift and displacement on the underlying fault, so the ability to identify the structural style of active fault-related folds is essential to properly defining the slip on an active fault based on the uplift pattern. This is especially important in cases where faults do not reach the surface and only fold patterns are observable at the surface.

Over the past two decades, kinematic models for several different types of contractional fault related folds have been developed and successfully applied to describe a variety of natural structures [e.g., Suppe, 1983; Suppe and Medwedeff, 1990; Erslev, 1991; Allmendinger, 1998; Suppe et al., 2004; Shaw et al., 2005, and others]. With this

An edited form of this manuscript was accepted for publication in the American Association of Petroleum Geologists Bulletin.

proliferation of fault-related fold models, it is often challenging to properly identify which class of models is most appropriate to describe a given structure. Additionally, there are many natural structures that are sufficiently complex, or have exhibited different fault-related folding mechanisms over their history, that they are not well explained by a single model. Thus, it is desirable to have an independent means of discerning the style of fault-related folding present in the structure. One way of achieving this is by observing displacement as a function of distance along the fault (termed the displacement-distance profile), because each of the major types of contractional fault-related fold model–fault-bend, shear fault-bend, and fault-propagation–has distinctive patterns in their displacement-distance profile (Figure 2.1).

This study will first illustrate the displacement-distance profiles expected for end-member fault-related folding models. These predictions will then be compared with a series of structures imaged with seismic reflection data to illustrate that the predicted displacement profile for each of these models is consistent with patterns of displacement observed in natural structures. By establishing that the displacement models characteristic of each folding model are unique and applicable to natural examples, we are then able to interpret the displacement-distance profile for a complex, multi-stage natural structure and restore portions of its deformation history that are consistent with the different fault-related-folding mechanisms indicated by the displacement profile. Analysis of the geometry of overlying growth strata further supports these interpretations, suggesting that analyzing displacement profiles may be used as an important independent means of identifying which fault-related-folding mechanisms may have been active throughout the deformation history of a given structure.

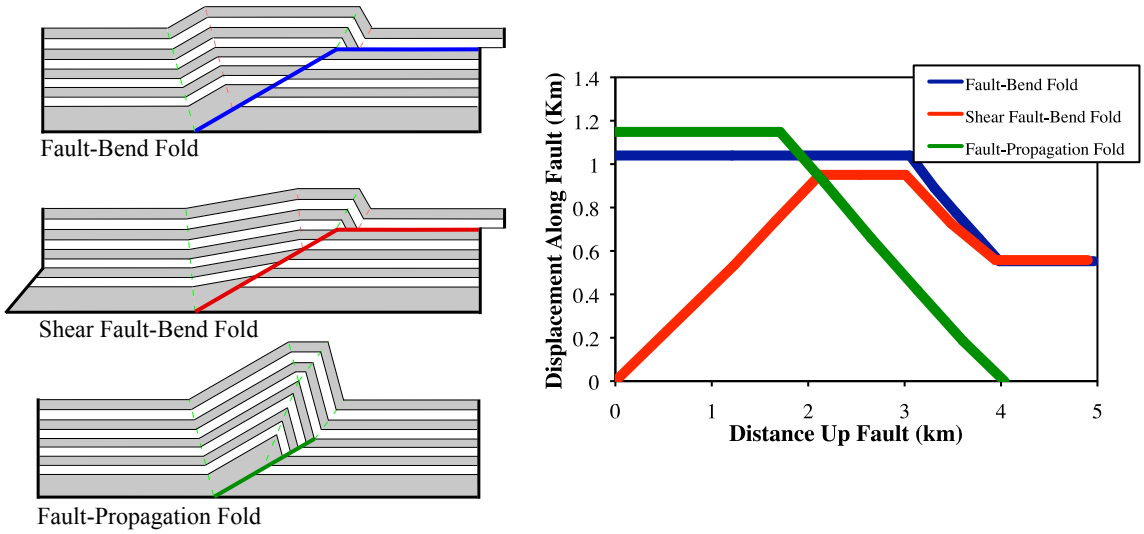


Figure 2.1: Kinematic models illustrating fault-bend, shear fault-bend, and fault-propagation folding. A plot of the displacement along the fault as a function of distance along the fault, termed the distance-displacement plot, illustrates the characteristic trends in displacement for each model.

### 2.2.1 Previous work on distance-displacement profiles

A displacement-distance plot is generated by measuring the offset between the footwall and hanging-wall cutoffs of a number of rock units (the displacement), and plotting it as a function of distance along the fault surface from a defined point along the fault (Figure 2.1). Previous quantitative work on displacement profiles has primarily focused on normal faults [e.g., Muraoka and Kamata, 1983; Kattenhorn and Pollard, 2001], although variation in displacement in contractional structures has also been measured in various studies. Williams and Chapman [1983] established the basic concept of a displacement profile for a thrust fault, which was extended by Hedlund [1997] to examining existing fault-propagation folding models. Other researchers have sought to characterize displacement profiles for natural structures. Rowan and Ratliff [1988] noted that displacement along thrust and reverse faults varies as a function of structural style and the presence of fault bends. McConnell et al. [1997]

made observations of displacement profiles in field outcrops in the Appalachians, whereas Briggs et al. [2006] measured variations in displacement on structures in the Niger Delta. The goal of our study is to develop a comprehensive understanding of the patterns of displacement along faults in the various classes of fault-related folds, in a manner that can inform interpretations of natural structures. We extend the analysis of displacements of end-member fault-propagation folds from previous studies [Hedlund, 1997] to a broader range of structural styles, and then compare these profiles to those of natural structures in a variety of geologic settings.

### 2.2.2 Data Sets

Structures that are used as examples in this paper come from a variety of geographic locations and contractional tectonic environments. The faults studied were mapped in two- and three-dimensional seismic reflection datasets from the Niger Delta, offshore Nigeria in the Gulf of Guinea (2-D and 3D), the Sichuan Basin, south-central China (2D), the Cascadian accretionary prism off the western shore of Vancouver Island, Canada (2D), and the Sierras Pampeanas, in the foreland of the Andean mountains in northern Argentina (2D). The locations of structures analyzed in this paper are highlighted in Figure 2.2.

Structures analyzed in this study were chosen based on the following characteristics: outstanding seismic imaging of the sedimentary layers, minimal ambiguity about fault geometry, and readily correlated stratigraphy on either side of the fault. The lattermost condition was ensured by either correlating stratigraphy across a 2d seismic grid survey or 3D seismic survey, where available. In cases where this was not possible, examples were chosen in which the stratigraphy has a sufficiently distinctive seismic character that correlation across the fault was unambiguous.

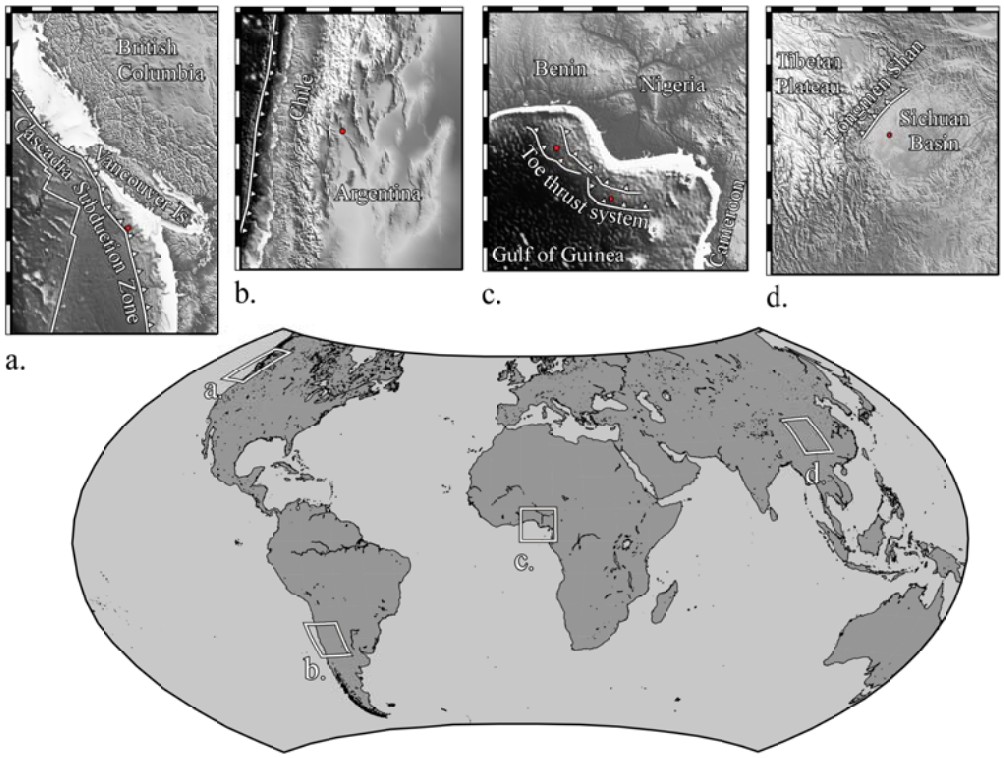


Figure 2.2: Locations of structures analyzed in this study, with inset maps of (*a*) Cascadia, western Canada, (*b*) the Sierras Pampeanas in Argentina, (*c*) the offshore Niger Delta in the Gulf of Guinea, and (*d*) the Sichuan Basin in China.

### 2.2.3 Regional Setting

The Sichuan Basin in south-central China is a continental basin in a continental convergent tectonic setting. The basin lies at the eastern margin of the Himalayan uplift, and is bounded on all sides by fold and thrust belts [Burchfiel et al., 1995; Royden et al., 1997]. The structure analyzed in this study is in the interior of the basin, but is associated with deformation propagating outwards from the Longmenshan fold-and-thrust belt, which defines the northwestern margin of the basin. The lithology of this portion of the basin consists of Paleozoic and Mesozoic carbonates interbedded with siliciclastics [Meng et al., 2005]. The fault in this study soles into a detachment localized in a Triassic evaporite layer [Hubbard et al., 2010].

The Niger Delta is a linked extensional and contractional passive-margin system that formed as a result of loading of sediments from the outflow of the Niger River into the Gulf of Guinea. The sediments in this system are composed of Cenozoic marine shales and more coarsely-grained turbidites that overlie the attenuated transition between African continental crust and oceanic crust [Damuth, 1994; Corredor et al., 2005a; Bilotti and Shaw, 2005]. Gravity-driven collapse of the sediments deposited in the Niger River Delta results in active extension onshore and on the continental shelf. This displacement is linked through a detachment in overpressured shale units to contractional deformation at the toe of the system in deep water. The lithologically weak marine shales promote the development of shear in many of the structures, which is manifest in the geometries of the structures that develop [Corredor et al., 2005b; Suppe et al., 2004].

Structures within the accretionary prism of the subduction zone in Cascadia, off the western coast of Canada, were also analyzed in this study. These data were acquired as part of a 2-D seismic reflection campaign on the portion of the accretionary prism offshore Vancouver Island in Ocean Drilling Program (ODP) Leg 146 [Hyndman et al., 1994]. Subduction of the Juan de Fuca oceanic plate (which is the remnant of the much more extensive Farallon plate) under continental North America at this location has persisted since the Eocene [Riddihough, 1984; Atwater, 1989; Hyndman and Hamilton, 1993, and others]. Current convergence rates are $\sim 45$ mm/yr, orthogonal to the plate margin and the coastline of British Columbia [Riddihough, 1984; Demets et al., 1990]. The structures investigated in this paper are the westernmost, frontal thrusts of the active accretionary prism overlying the subduction zone.

Finally, we include an example of a basement-involved structure from the western Sierras Pampeanas region of northern Argentina. In this section of the subduction zone, the Nazca plate subducts at a nearly horizontal angle [Barazangi and Isacks,

1976] at a rate of $\sim$ 10 cm/yr [Minster and Jordan, 1978; Demets et al., 1990, and others]. Associated with this shallow-angle subduction, contractional deformation extends several hundred kilometers further into the continent, and is characterized by predominantly thick-skinned thrust faulting. Deformation of late Paleozoic and Cenozoic-age sediments overlying a basement consisting of Precambrian metamorphic and Paleozoic plutonic rocks has taken place from 10 MYA to the present [Jordan and Allmendinger, 1986], primarily through what have been characterized as basement-involved fault propagation folds [Zapata and Allmendinger, 1996]. The particular structure analyzed for this study lies in the Bolsones embayment of the Bermejo basin, in the transitional region between the pre-Cordillera and the Sierras Pampeanas, north of San Juan, Argentina. Studies of syntectonic deposition of sediments suggest that thick-skinned thrust systems in this region have been active for the past 5 million years [Zapata and Allmendinger, 1996].

## 2.3 METHODS

Displacement was measured as the distance along the fault between the mapped terminations of a given stratigraphic layer at the fault surface, such as is done in Williams and Chapman [1983], and others. This is contrasted with a simple measurement of throw, the vertical component of displacement, which has been used as a proxy for displacement in some previous studies [e.g., Mansfield and Cartwright, 1996]. While the latter approach has the benefit of being measureable without relying on quality of imaging immediately adjacent to the fault surface, it is not appropriate for the structures in this study due to the non-planarity and dip of the faults and folding adjacent to the fault, which are essential considerations for this measurement. However, we have ensured that the quality of the seismic reflections is sufficiently high

that the uncertainty in the geometry of near-fault horizons is minimal and does not significantly impact the overall interpretations.

There are numerous factors that contribute to uncertainty when interpreting reflections. Because the faults analyzed in this study have shallow dips, the angle between the stratigraphic layers and the fault is small, so a small change in the fault dip can create a significant change in the apparent displacement measured along the fault. As a result, uncertainty in the fault dip is one of the largest potential sources of error in the measurement; this is the source of error quantified and reported in this study following the method described in Bergen and Shaw [2010]. The favored, or most likely fault geometry is plotted in blue on each displacement-distance plot. The minimum and maximum fault dips that are permissible from the seismic reflection data are then interpreted, and measurements of displacement of the stratigraphic layers across each of the end-member fault geometries are reported as the minimum and maximum fault-dip on each of the displacement-distance plots as a means of characterizing the uncertainty in the measurement.

While uncertainty due to fault geometry is the primary source for this measurement, there are additional sources of uncertainty that are difficult to quantify but may affect the reliability of the measurement. Special care must be taken to minimize contributions from these factors. For example, it is challenging to quantify how much uncertainty results from tracing a reflector through a poorly imaged zone; these shadow zones are common in the foot-wall near a fault due to perturbations to the velocity field in the hanging-wall and migration-related processing effects [Kleyn, 1983]. Additionally, changes in the thickness and internal structure of a stratigraphic unit can lead to the bifurcation of a seismic reflector [Sherriff, 1977], which can contribute to uncertainty in how to extend the interpretation of the stratigraphic layer through the bifurcated region. Both of these factors can contribute to local changes in ob-

served displacement gradients. The structures in this study were chosen specifically to have minimal contributions from both of these sources of error.

Other factors can contribute to uncertainty in the absolute value of the measured displacement, but have little effect on the overall trend of the displacement gradients; as this study is interested in the latter, these sources of error are not explicitly addressed in this study. These factors can include uncertainties in seismic velocity in the depth conversion process, or other artifacts of processing the seismic data, including the challenge of accounting for lateral variations in velocity and out-of-plane energy in 2D surveys. Uncertainties in the interval velocities used in converting the seismic data from time to depth can vary up to +/-5 percent [Sherriff, 1977], and could create variations in the absolute values of displacement measurements of up to 10 percent, though the relative smoothness of the velocities in these regions would ensure that the trends in displacement gradient observed in the study would remain unaltered. Additionally, the imaging resolution of the seismic data is a fundamental limit on the scale of measurement possible; given dominant wavelengths of seismic reflection data between 100 and 300 m (for the depth range of interest to this study) and the ability to resolve features with minimum vertical separation of one-quarter wavelength, features between 25 and 75 m in thickness represent the minimum resolvable feature. This source of uncertainty associated with the resolution limit of seismic data is sufficiently small compared to uncertainties in fault dips and cutoffs geometries that it is not explicitly considered in the calculation of error for this study.

## 2.4 Model Predictions and Examples

Fault-related folds develop as strata pass over bends in faults, are deformed above propagating fault tips, and/or are folded above detachment surfaces. These struc-

tures are common in ancient and active orogenic and passive margin fold-and-thrust belts throughout the world [for example, Rich, 1934; Rodgers, 1950; Suppe, 1983; Rodgers, 1990; Erslev, 1991; Rodgers, 1991; McConnell, 1994; Erslev and Mayborn, 1997; Suppe and Medwedeff, 1990; Shaw and Suppe, 1994; Yue et al., 2005; Hubert-Ferrari et al., 2007; Corredor et al., 2005a; Shaw et al., 2005]. In this study we examine the displacement/distance characteristics of three main types of fault-related folds: fault-bend folds, shear fault-bend folds, and fault-propagation folds. Each of these structural styles is characterized by a distinct fold geometry and distribution of displacement along the fault (Figure 2.1).

### 2.4.1 Fault-bend folding

Fault-bend folding theory was developed by Suppe [1983] as a geometrically and kinematically consistent way of predicting the geometry of parallel folds that develop as strata are displaced over a fault bend. The theory indicates that displacement remains constant along planar fault segments, and changes abruptly at fault bends. In the case of a simple thrust ramp extending to an upper detachment, the theory predicts constant displacement along the fault ramp. Similarly, displacement on the upper detachment above the bend is also the same everywhere, although it is generally less than displacement on the ramp. The magnitude of the change in displacement is dependent on the fault geometry and stratigraphic cutoff angles, and can be predicted by quantitative fault-bend-folding theory. Based on this, it might be expected that a displacement profile across a fault bend would be characterized by two zones of constant slip separated by an immediate change at the fault bend. However, what one actually measures are two zones of constant displacement, separated by a linear gradient of displacement in a finite zone beginning at the fault bend. This observation highlights the fact that displacement, and not slip, is what is actually measured along

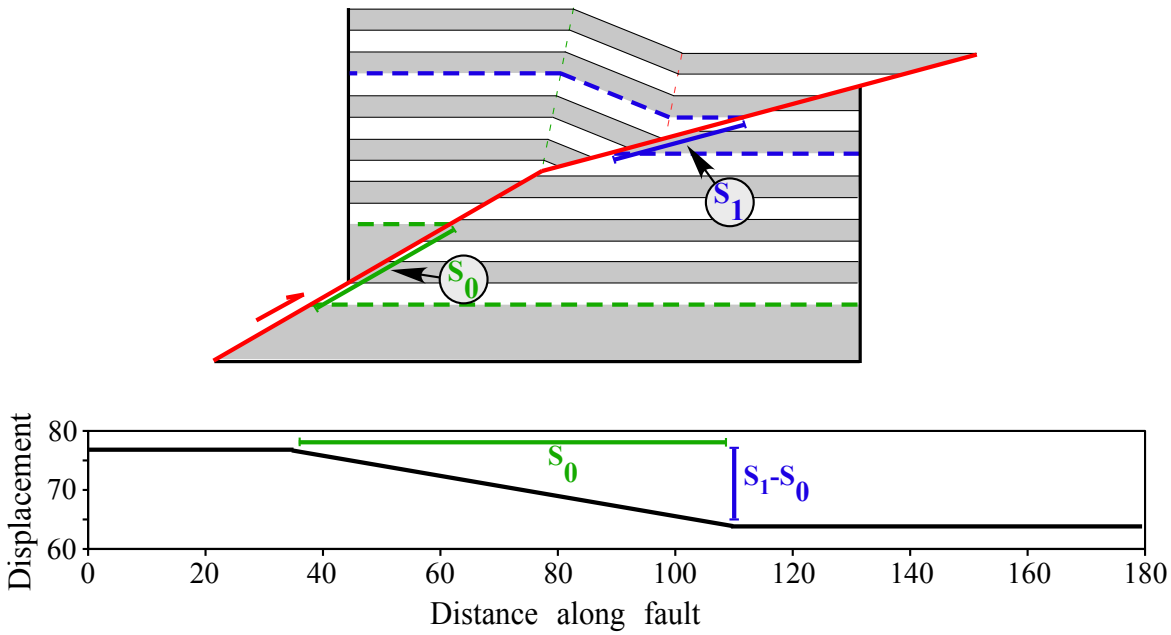


Figure 2.3: (*a*) A kinematic model of a fault bend fold demonstrates the decrease in displacement across an anticlinal fault bend, from $S_0$ below the bend to $S_1$ above the bend. (*b*) The distance displacement plot for this structure shows a linear gradient between these two displacement values, as material within the fold limb has only undergone folding for a portion of its structural history.

the fault when matching hanging-wall and foot-wall cutoffs. While slip along the fault changes instantaneously at the fault bend, displacement is the result of cumulative motion of the hanging-wall over the foot-wall. Material that is in the sloped region of the displacement profile began beneath the fault bend, but after some increment of slip, passed over the fault bend; therefore, its displacement reflects that it experienced deformation in both slip regimes over portions of its deformational history.

As fault bend folding theory prescribes a unique relationship between the displacement observed along the fault on either side of a fault bend (the $R$ value in Suppe [1983]) for a given fault geometry, the manner in which displacement changes at a fault bend is also predicted. The displacement observed for a given layer that is always above, or always below, the fault bend during the displacement history is

equal to the displacement on the underlying segment of the fault. The ratio of this displacement fully above and below the fault bend can be predicted by the $R$ value, or the ratio of the displacement above ($S_1$) to the displacement below ($S_0$) the fault bend, which is uniquely derived for a given structural geometry using fault bend folding theory. The zone of displacement gradient can also be quantified. On a plot of displacement as a function of distance up the fault, the displacement gradient region due to the fault bend begins at the location of the bend, and extends for a region equal in length to $S_0$. Given that the change in displacement across this region is $S_1 - S_0$, the slope of this displacement gradient is $(S_1 - S_0)/S_0$, which is equivalent to $R - 1$ (Figure 2.3). The displacement at any given point in the gradient is straightforward to predict, because the gradient is linear.

### 2.4.2 Examples of fault-bend-folding behavior

To test these predictions of fault-bend fold theory, we first generate a displacement distance profile of mechanical model of a fault-bend fold developed using the discrete-element approach after Benesh et al. [2007] and Benesh [2010]. This numerical model was developed using the Particle Flow Code in 2-Dimensions (PFC-2D), a commercial discrete-element modeling code distributed by the Itasca Consulting Group. Layers of rock are modeled as aggregates of circular particles that interact with elasticity, friction, and cohesion at their contacts based on the method described by Cundall and Strack [1979], with values assigned to emulate the bulk mechanical properties of rocks in laboratory settings [Itasca, 1999]. The aggregate material is contained by walls that serve to define a ramp/flat fault geometry necessary to produce an anticlinal fault-bend fold, to drive deformation from the hinterland, and to confine the particles to the region of interest. As the hinterland wall is displaced to the right, the rock material must deform and pass over the fault bend, and the foreland wall

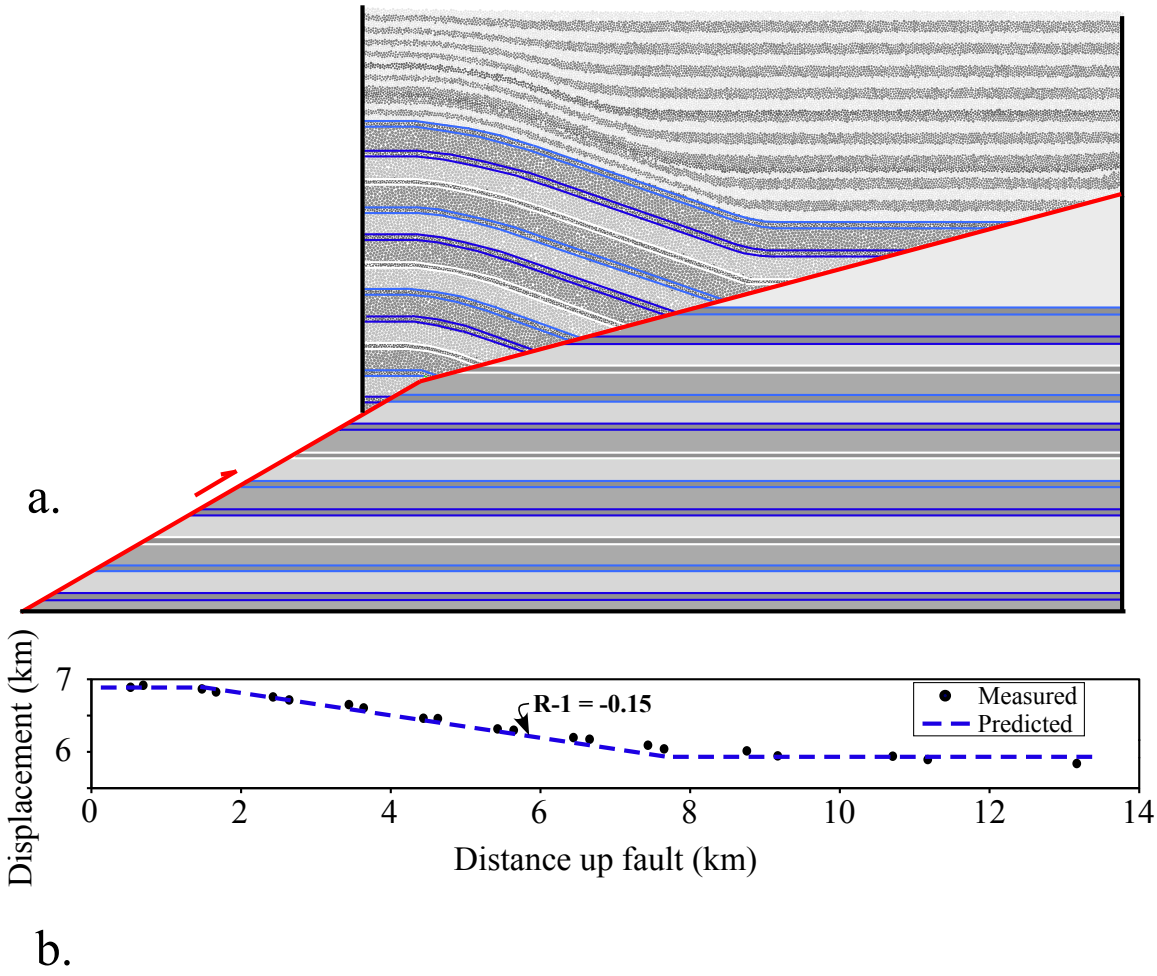


Figure 2.4: (*a*) A discrete element model (DEM) of a fault bend fold. (*b*) The distance-displacement plot for the DEM model (black dots) agrees very well with the decrease in displacement predicted by the (R-1) calculation associated with this fault geometry (blue dashed line).

moves such as to relieve tectonic stresses while maintaining the confining stress on the rocks adjacent to it (see Benesh [2010] for a more thorough description of the modeling approach).

The value of examining displacement patterns in a mechanical model is that both the displacements along the fault segments and the fold geometries are emergent model behaviors and can be measured very precisely. The model reproduces the primary features of fault-bend fold theory: a fold limb of relatively constant dip and constant layer thickness, with an anticlinal axial surface tied to the anticlinal fault bend and a passive synclinal axial surface that has been translated along the upper detachment (Figure 2.4A). Measurement of the offset of stratigraphic layers in the hanging-wall and foot-wall of the model display a constant displacement along the fault ramp and detachment, and a linearly decreasing displacement in the fold limb region. Fault-bend folding theory predicts constant displacement along the ramp and detachment, with a gradient of -0.15 in the fold limb region (calculated as $R - 1$ for the prescribed fault geometry), which is in excellent agreement with the observed displacement distribution (Figure 2.4B).

In addition, we evaluated the displacement-distance relationship for several natural fault-bend folds to assess how well they conformed to the kinematic theory. In the case of a simple thrust ramp from the Sichuan Basin, China (Figure 2.5), we observe within the uncertainty of the measurement that the displacement along the thrust ramp is constant, as predicted by the fault-bend-folding model.

In contrast, when material in the hanging-wall moves across a fault bend, the theory predicts that a fault bend fold is formed, and the amount of displacement along the fault varies as described in the section above. To examine this behavior, we analyzed an anticlinal fault-bend fold overlying a fault with two distinct anticlinal bends from the southern Niger Delta (Figure 2.6A). Measurement of the stratigraphic

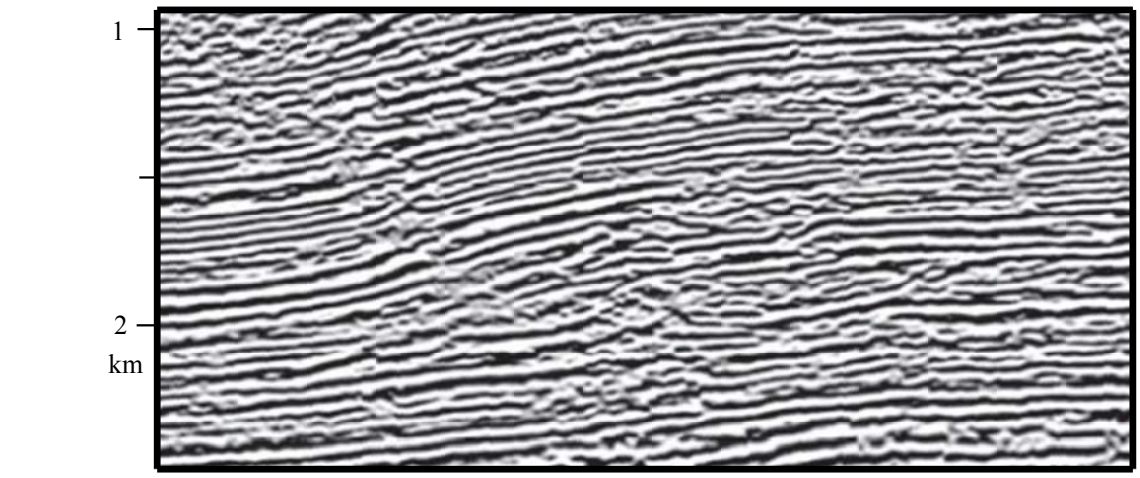


a.

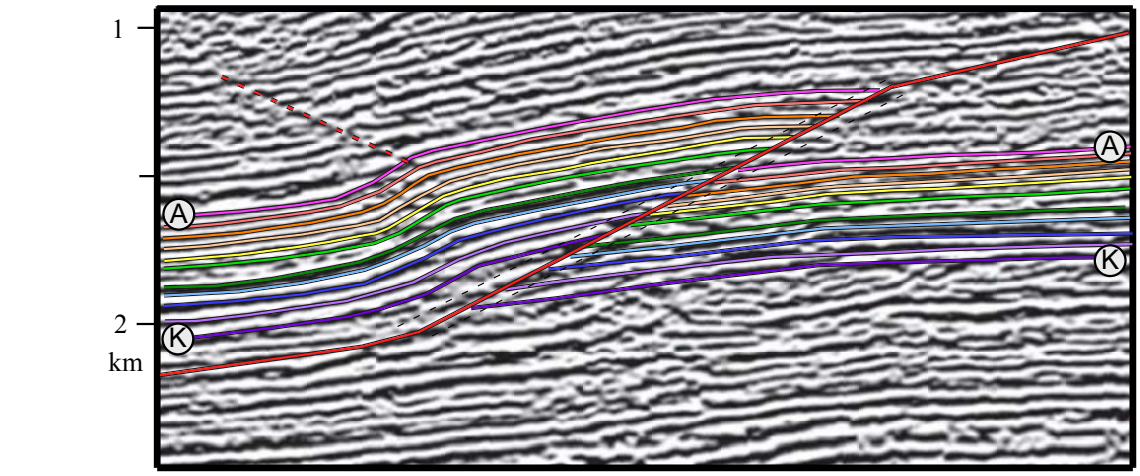


b.

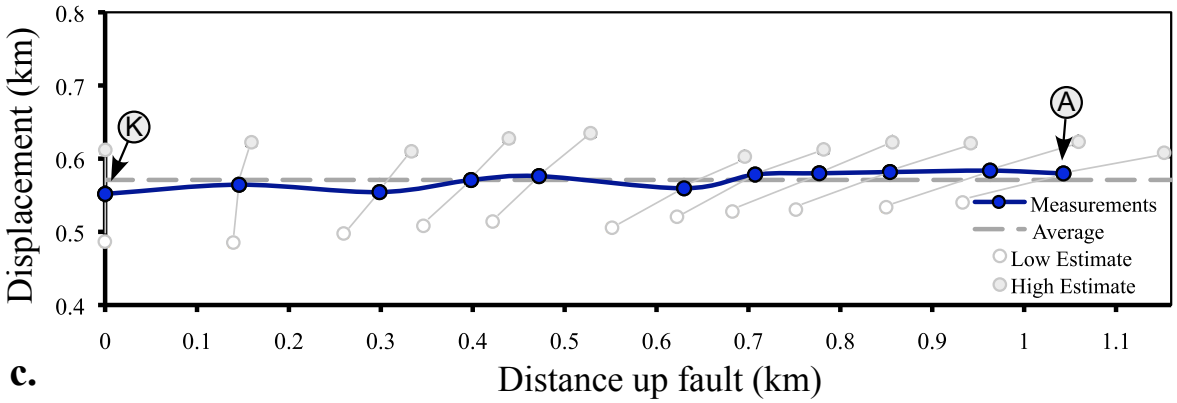


c.

*(Continued on next page)*

Figure 2.5: (*Continued from previous page*)(*a*) Uninterpreted, migrated, depth-converted seismic reflection data from the Sichuan Basin, China. (*b*) Interpretation of the seismic reflection data, with the faults (red), stratigraphic layers A-K, and uncertainty of fault location (black dashed lines). (*b*) Distance-displacement plot of data (blue), with minimum (white ) and maximum (gray ) measurements based on the range of possible fault dips, with light gray lines connecting minimum, preferred, and maximum displacement values for a given stratigraphic layer and a linear best fit to the preferred values (dark grey dashed line). Data from Shaw et al., 2005, courtesy of CNPC.

layers offset across this fault demonstrates that displacement decreases across each of the two anticlinal fault bends (Figure 2.6B). Based on geometric fault-bend-folding relationships, the angle between bedding and the fault below the bend ($\theta$) and the change in fault dip at the bend ($\phi$) define the expected R-value for the change in displacement at each fault bend, predicting gradients in displacement of -0.13 and -0.23 above the lower and upper fault bends, respectively. The measured displacements are consistent with these predictions of displacement gradients, within the uncertainty of the measurement, suggesting that this structure is consistent with fault-related folding theory. Furthermore, a fault-bend fold model generated from the observed fault geometry and back-limb dips that is consistent with these displacement gradients predicts the dips of the front-limb segments to within +/-1° (variation is due to the non-linearity of the limbs), indicating that the structural geometry is well represented by the fault-bend-folding model.

Figure 2.6: (*Continued on next page*)(*a*) Seimic reflection profile of an anticlinal fault-bend fold from the offshore Niger Delta, Nigeria. Interpretation of fault surface (red), fault bends (1 and 2) and stratigraphic horizons A-I. Distances are measured from the lowest layer (white point). (*b*) Measured distance displacement relationship (blue), with minimum (white ) and maximum (gray ) estimates. Displacement gradient for the modeled fault-bend fold (*c*) is also plotted (black dashed), with the locations of fault bends (1) and (2) highlighted. Data from Shaw et al., 2005, courtesy of Mabon Limited.

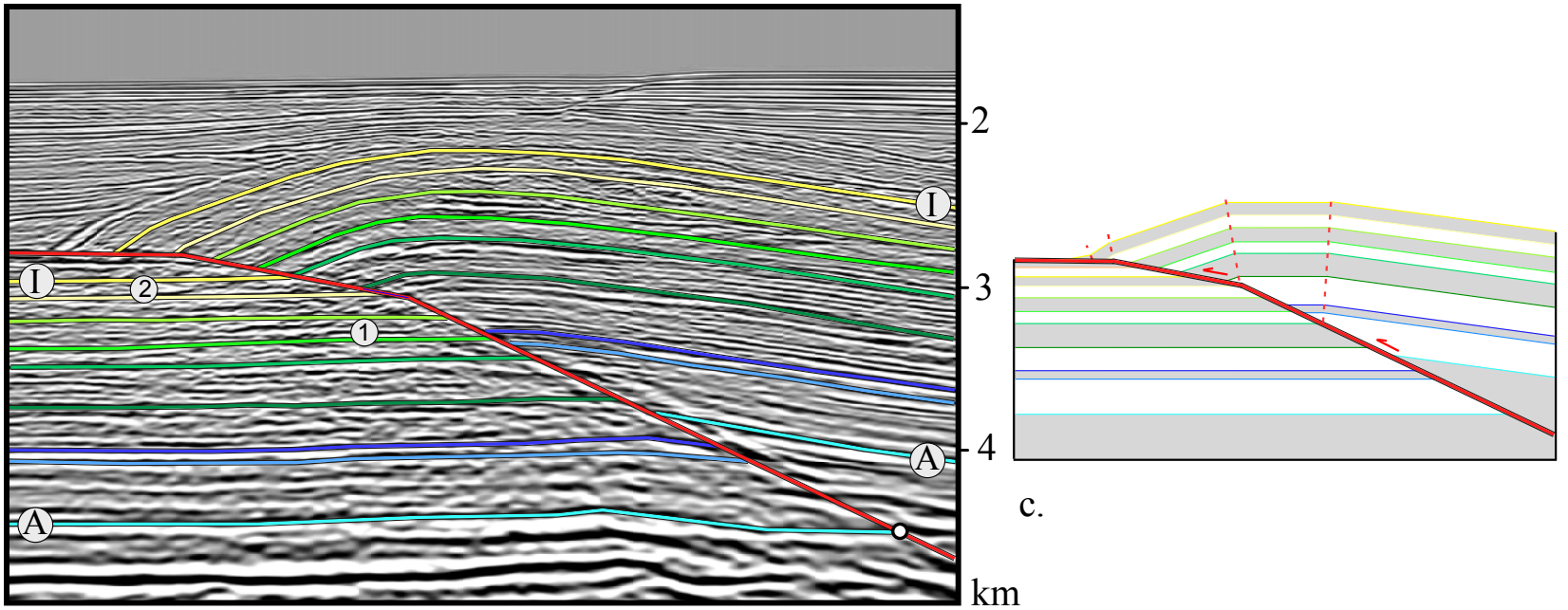


a.



c.

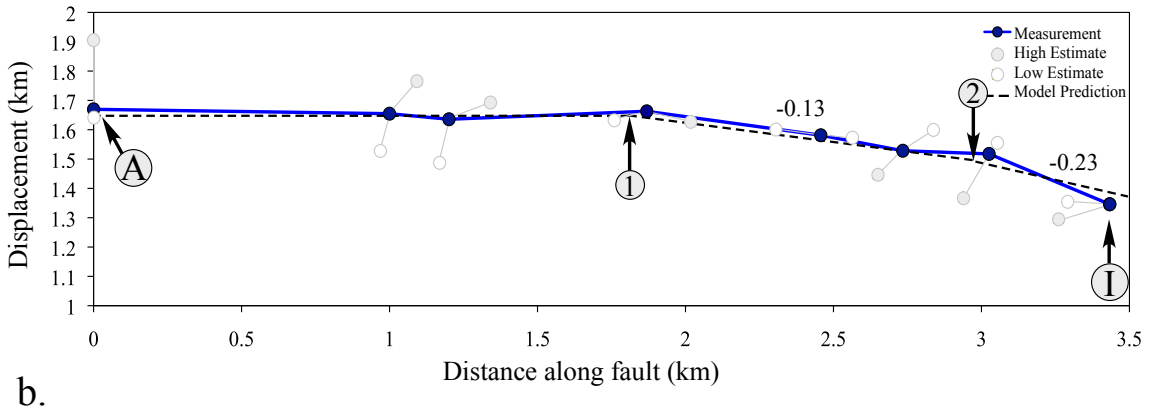


b.

*(Continued from previous page)*

### 2.4.3 Shear fault-bend folding

Structures in which a stratigraphic zone of finite thickness undergoes distributed shear deformation have been recognized in many regions in which a weak unit immediately overlies a detachment surface. This is often the case in regions in which a weak lithologic unit is involved in the deformation, such as salt (examples include offshore Brazil, Angola, Gulf of Mexico, Zagros) or over-pressured shale (southern Caribbean, Niger Delta, and others). Shearing in this stratigraphic interval generates a geometrically-distinct class of structures that are characterized by a back-limb that dips more shallowly than a fault-bend-folding model for the same fault geometry [Suppe et al., 2004]. Based on shear-fault-bend fold theory, the amount of displacement measured in this interval increases with distance up the fault ramp throughout the shearing interval. Above the shear interval, parallel folding results in constant displacement along the ramp (Figure 2.1B). This produces a pattern of changing slip and displacement along planar fault segments that strongly contrasts with standard fault-bend fold theory, which prescribes changes in slip and displacement only across fault bends.

For a given fault dip ($\theta$), back-limb dip ($\delta$), and height of the shearing layer above the detachment ($h$) (Figures 2.7A and B, sheared interval highlighted in light blue), a displacement gradient and maximum displacement can be calculated for a simple shear and pure shear fault-bend fold model that is consistent with the prescribed geometry. Based on these geometric parameters, the shear angle can be calculated:

$$\alpha = \cot^{-1}\left[\frac{\sin\,\delta}{2\,C}\left[\left(\frac{1}{\sin\,\delta\,\cot\,\theta\,+1\,-\cos\,\delta}\right)^{2}-\left(\frac{1}{\sin\,\delta\,\cot\,\theta\,+1\,-\cos\,\delta}\right)\right]\right]$$

where $C$ is 1 for pure shear and 1/2 for simple shear. Once the shear angle is known,

the slip ($s$) can be calculated as follows:

$$s = \frac{h \tan \alpha}{\cos \theta + \tan(\delta/2) \sin \theta}$$

as derived in in the appendix of Suppe et al. (2004). This slip value represents the displacement for the layer at the top of the shear interval and all layers above it, which undergo parallel folding in the model.

The displacement at the top of the shear section can then be used to determine the displacement gradient in the distance-displacement graph in the sheared interval (Figure 2.7C). For the end-member simple shear model, as described by Suppe et al. [2004], displacement along the fault is zero at the base of the thrust ramp and the slip value calculated above, $s$, at a distance of $h/sin\theta$ along the fault. Therefore, the change in displacement, $(s - 0)$, over the distance from the base of the ramp to a distance of $h/sin\theta$, results in a displacement gradient of $s{*}sin\theta/h$ in the shear interval. For pure shear, the displacement along the ramp does not decrease to zero, but rather, to a value defined by the amount of slip, $s_1$, at the base of the ramp. A graph of the relationship between back-limb dip ($\delta$) and displacement gradient for lines of constant fault dip is shown in Figures 2.7D and E, for pure and simple shear respectively. Given an observed fault dip and back-limb dip for a natural example, these graphs can be used to determine the displacement gradient for pure shear and simple shear models that match the prescribed fault and back-limb geometry. Thus, a comparison of the observed displacement gradient, in conjunction with other observations, can help to determine whether the structure in question is better modeled as a pure shear or simple shear fault bend fold. It should be noted that the existing pure shear fault-bend folding theory does not explicitly define the geometry of the layers in the shear interval. As such, a balanced, permissible, but non-unique solution is given here

(Figure 2.7B). Since the displacement gradient is dependent on the slip at the base of the ramp and the top of the shear interval, the displacement gradient is unlikely to change dramatically for other, perhaps equally valid solutions; however, one can envision a case where deformation in the sheared interval is accommodated in such a way that the increase in displacement is nonlinear.

### 2.4.4 Example of shear fault-bend-folding

To assess if the displacement pattern predicted by shear fault bend fold theory is present in natural structures, we analyze a contractional fault-related fold from Cascadia, off the western coast of Vancouver Island (Figure 2.8A) that illustrates the common features of this structural style. Measured displacement along the fault (Figure 2.8B, black) illustrate that displacement increases dramatically through stratigraphic layers P-K, increases gradually in layers K-F, and that above that interval (F-A), displacement along the fault ramp is relatively constant. A line-length, or palinspastic method [Shaw et al., 2005] of measuring the shear profile of a structure (Figure 2.8B, red) shows a similar trend. Thus, we conclude that the shear within this structure is responsible for the observed displacement gradient on the thrust ramp.

A shear-fault-bend fold model was constructed using the kinematic theory [Suppe et al., 2004] based on the fault geometry and the identification of the shear interval from the displacement gradient measurements (Figure 2.8, inset). As the distance-displacement plot indicates that displacement decreases to zero at the base of the fault, we conclude that a simple shear fault-bend folding solution is appropriate for this structure. The simple shear model is further supported by the fact that in the seismic data, the anticlinal axial trace appears to be linear and intersects the ramp at the point where it also intersects the detachment, which is the consistent with the prediction for a simple shear fault-bend fold, but not a pure shear fault-bend

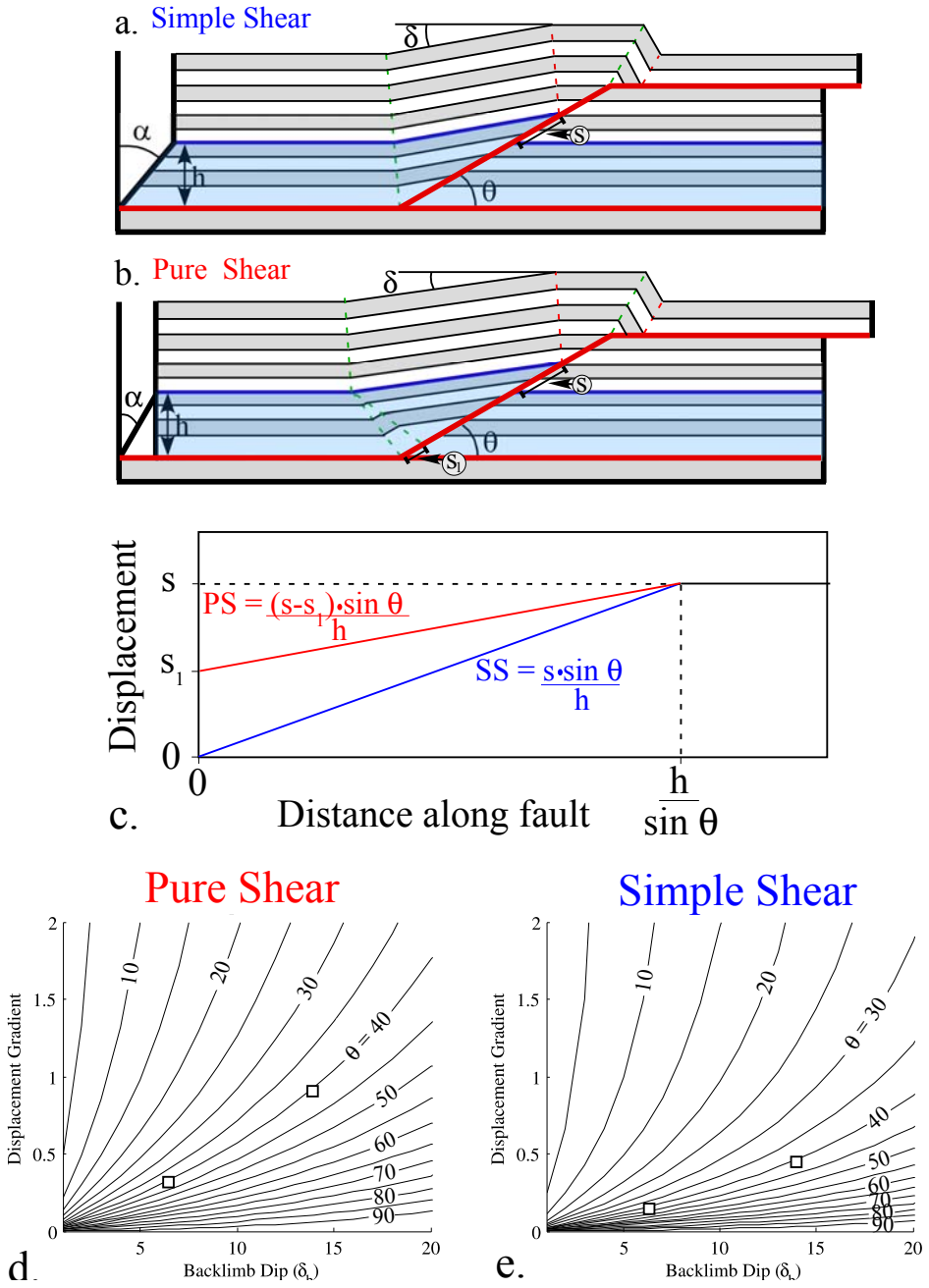


Figure 2.7: *(a)* and *(b)* Simple and pure shear fault-bend folding models, with various features labeled as referred to in the text. *(c)* Distance-displacement plot for simple (blue) and pure (red) shear models, with quantities used in the slope calculation for the layers in the shear interval highlighted. *(d)* and *(e)* Plots of the relationship between back-limb dip and displacement gradient in the sheared interval for lines of constant fault dip ($\theta$) for pure and simple shear, respectively. The locations of the fault and limb geometry for Figure 2.8 are plotted as white squares.

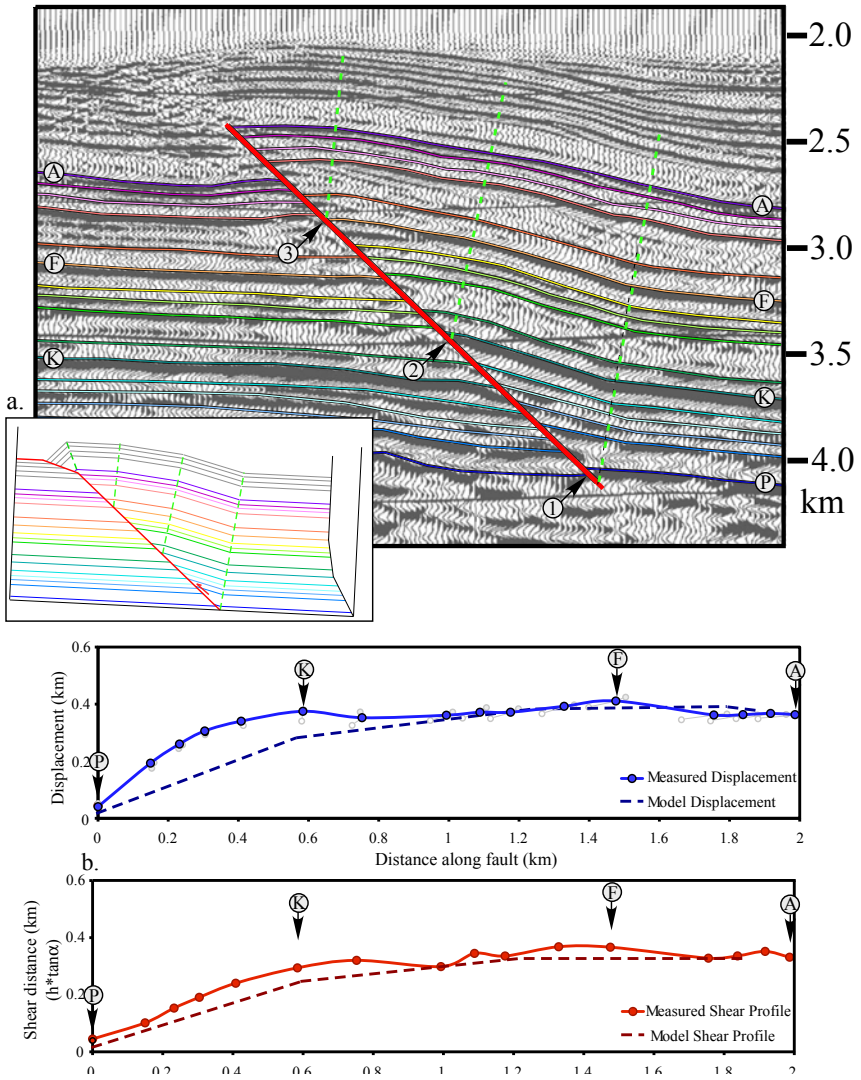


Figure 2.8: (*a*) Seismic reflection profile of a shear fault bend fold in the Cascadia accretionary prism, offshore Vancouver Island, western Canada, with interpreted fault (red) and stratigraphic layers A-P. Locations of axial surfaces (1),(2), and (3) indicate transitions in the shear interval, as discussed in text. A simple shear fault bend fold model was constructed based on these geometric observations (inset). (*b*) Distance-displacement plot for data (blue), minimum (white) and maximum (gray) estimates, the model displacement (dark blue, dashed). (*c*) Palinspastic estimate of shear (red) and model shear profile (dark red). Locations of stratigraphic layers that mark transitions in the shear interval (K and F) are highlighted. Data from line 89-04 of Hyndman et al., 1994, Shaw et al., 2005.

fold (e.g., Corredor et al. [2005b]; see figures 2.7A and B for a comparison). The model was constructed to match the observed fold limb dips of 14° (between the axial surfaces labeled 1 and 2) and 7° (between 2 and 3) in the back-limb, resulting in shear angles ($\alpha$) of 29° and 12°, and displacement gradients of 0.44 and 0.17, respectively. The distance-displacement plot for this model is broadly consistent with both the palinspastic approach and the displacement gradient approach, although it should be noted that the additional displacement measured in the P-K interval of the distance/displacement plot is due to deformation of the foot-wall, which is not accounted for in the model. Combining these two approaches highlights these aspects of the deformation in natural structures that are not captured in the kinematic model.

Many studies of fault displacement consider the location of the maximum displacement as representative of the point at which the fault initiated [Ellis and Dunlap, 1988; Briggs et al., 2006, and others]. This is based on the assumption that, as the fault grows and slip accumulates on the structure, the place where the fault first initiated will accumulate the greatest amount of slip. As the point of maximum displacement on many natural faults is observed to be in the center of the structure, this has led to the development of bilateral, or double-edged, fault propagation folding models [Kattenhorn, 1994; Tavani et al., 2006]. We propose that in some cases, pure or simple shear of a layer of finite thickness in the hanging-wall can produce a displacement maximum in the center of a fault, irrespective of where the fault nucleated. In the previous example (Figure 2.8A), the fold and fault geometry suggest that the structure is a shear fault-bend fold, and the displacement gradient observed is also consistent with that model. In a shear fault-bend folding model, the fault propagates to its full extent before significant displacement has accrued. This suggests that shear should be considered and tested before inferring that the location of maximum displacement is indicative of the location of fault nucleation.

### 2.4.5 Fault-propagation folding

Fault-propagation folds are an important class of structures that form at the tips of faults as they propagate upwards through sedimentary layers. These folds develop as slip is consumed, and the resulting folds often have steeply dipping or overturned forelimbs that are pinned to the fault tip. Most fault propagation folds have many qualitative similarities [Shaw et al., 2005]:

1. A highly asymmetric shape, with a relatively steep and narrow forelimb and a longer, more gently dipping back-limb,

2. Slip that decreases along the fault toward the fault tip, and,

3. A syncline pinned to the upward projection of the fault tip.

Many theories have been developed that provide a geometric and kinematic model of deformation for these structures, the most commonly applied of which include constant-thickness and fixed-axis fault propagation folding [Suppe and Medwedeff, 1990], and trishear folding [Erslev, 1991; Allmendinger, 1998]. These models make specific predictions about the shape of the fold in relationship to the amount of slip and the fault dip. In addition, a variety of other models have been developed to address a specific subset of the natural structures or to attempt to explain a specific observation (for example, basement-involved models [Narr and Suppe, 1994; McConnell, 1994; Spang and McConnell, 1997], variable front-limb thickness [Jamison, 1987; Chester and Chester, 1990], externally applied shear [Mitra, 1990], front-limb dip steepening with increasing slip [McConnell, 1994], complex geometries [Chester and Chester, 1990], mixed-mode structures [Erslev and Mayborn, 1997], and double-tipped fault propagation [Kattenhorn, 1994; Tavani et al., 2006].

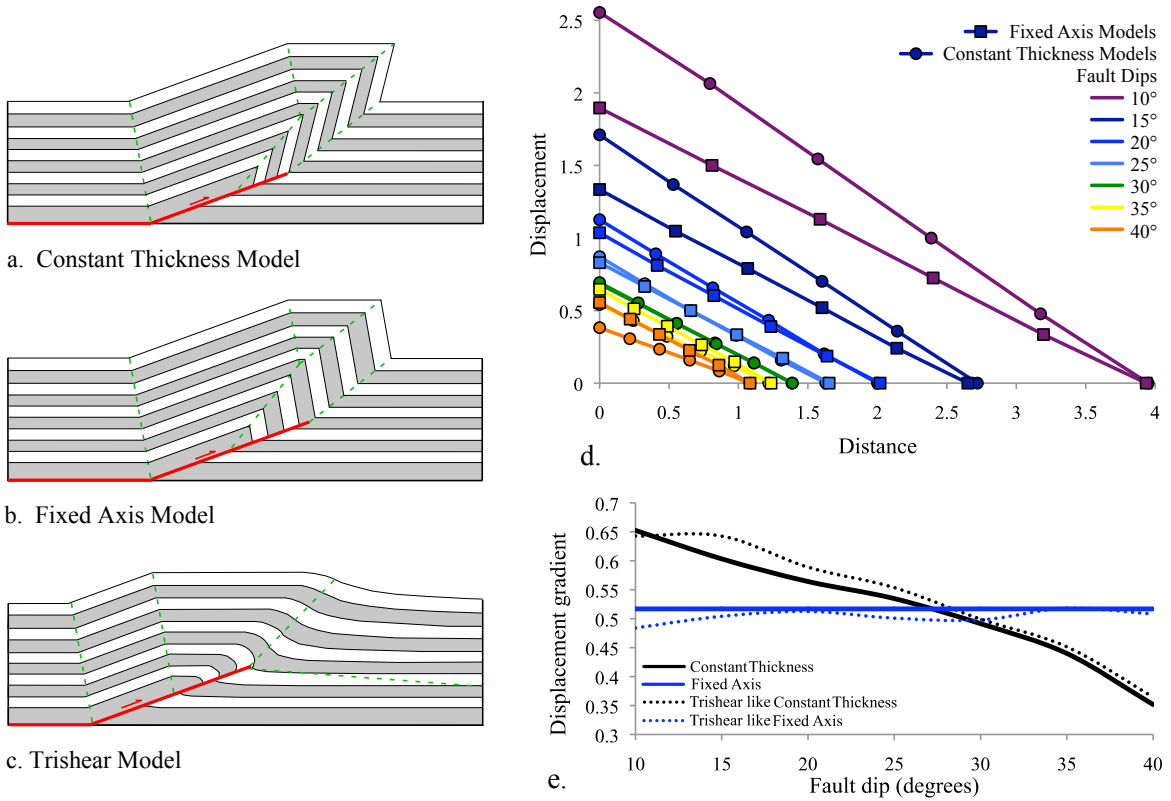


Figure 2.9: *(a)-(c)* Kinematic models of the most commonly applied fault-propagation folding models. *(d)* Displacement-distance plot for constant thickness (circles) and fixed axis (squares) models of varying fault dip, illustrating that the models are the same at 29°; at higher fault dips, constant thickness models have shallower gradients, and at lower dips, constant thickness models have steeper gradients. *(e)* Displacement gradient as a function of fault dip shows that fixed axis models have a constant displacement gradient (blue), while displacement gradient decreases as fault dip increases for constant thickness models (black). Trishear models with P/S ratios and fault geometries identical to the previous models show the same trends in displacement gradient, indicating that displacement gradient is a function of P/S ratio for trishear models.

Fault-propagation folds are generally characterized by regions of constant slip at the base of the thrust ramp, and decreasing displacement along the upper portion of the fault (Figure 2.1). Each of the existing kinematic models for fault-propagation-folding generates distinct predictions for fold geometry, uplift, and displacement (Figures 2.9A-C). However, for any model with a constant propagation-to-slip ratio (which is required by constant-thickness and fixed-axis models, and may be specified in trishear models), the gradient in displacement is linear (Figure 2.9D). In detail, the slope of this linear trend depends on model type, propagation-to-slip ($P/S$) ratio, and fault dip. We examine these relationships in more detail for the constant thickness, fixed axis, and trishear models.

For models of constant thickness fault-propagation folds developing from a fault stepping up from a detachment, displacement gradient changes as a function of fault dip because (1.) for a given amount of shortening, the distance between bed cutoffs that have been displaced along the fault varies as a function of fault dip, and (2.) fault-propagation-folding-related strain in the hanging-wall, reflected by the tightness of the fold, varies as a function of fault dip, as prescribed by the models. As fault dip increases, the first effect decreases the displacement gradient. However, the fold tightness also decreases, so the second factor increases the displacement gradient. These factors do not entirely offset, so overall, displacement gradient decreases with increasing fault dip. Additionally, propagation-to-slip ($P/S$) ratio increases with increasing fault dip for constant thickness models. In fixed-axis models, both of these factors are at play, but layer thickness changes in the front-limb of the fault-propagation-fold play an additional role. The effect of this additional factor is such that displacement gradients and $P/S$ ratios for fixed axis fault propagation folds are insensitive to fault dip (Figure 2.9E).

For fixed-axis and constant-thickness models, a given initial layer and fault geom-

etry leads to the development of a unique fault-propagation fold limb geometry, $P/S$ ratio, and displacement gradient. However, because the trishear model inherently has more variable parameters, a given fault and layer geometry does not determine a unique fold geometry, without specifying additional model attributes. Therefore, to compare this approach to the previous ones, trishear models with the same fault geometry, layer geometry, and $P/S$ ratios were generated. The displacement gradients for these models match those for the corresponding fixed axis and constant thickness models (Figure 2.9E), indicating that fault geometry and $P/S$ ratio are the factors that determine the displacement gradients for trishear fault-propagation fold models, as is true of other fault-propagation folding models.

### 2.4.6 Examples of fault-propagation folding

To assess if natural structures exhibit displacement gradients predicted by fault-propagation fold models, we examined a structure from the northern Niger Delta (Figure 2.10A) that is imaged in high-quality seismic reflection data. Qualitative observations, such as folding unassociated with a fault bend and an active synclinal axial surface tied to the upward extension of the fault, serve to identify this structure as a fault propagation fold. The displacement profile for this structure exhibits a distinctive linear negative gradient along the fault (Figure 2.10B), with displacement values that approach zero. This pattern is generally consistent with fault-propagation folding models, and thus helps confirm our interpretation of this structure.

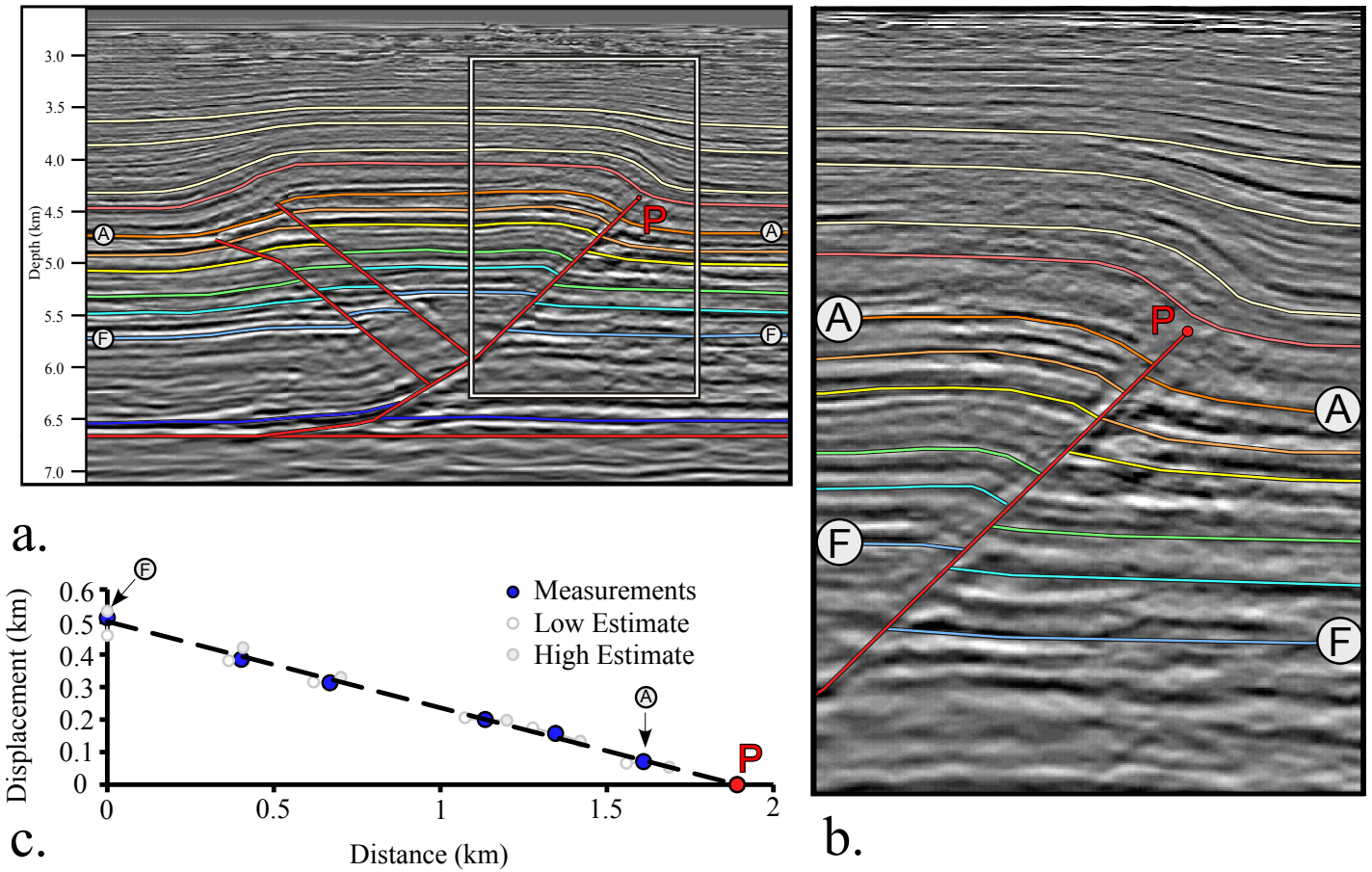


Figure 2.10: *(a)* Seismic reflection profile of a fault-propagation fold in the Niger Delta, offshore Nigeria, with fault (red) and stratigraphic layers (A-F) interpreted. *(b)* Higher resolution image of the fault tip area, with the predicted fault tip location labeled (P). *(c)* Distance displacement plot displays a linearly decreasing displacement for layers F-A (blue) with minimum (white) and maximum (gray) displacement estimates. The fault tip location is predicted by the point where the line intersects the X-axis (where displacement = 0), (P). Data is owned and provided courtesy of CGGVeritas, Crawley, UK.

The location of the fault tip may be predicted based on the observed displacement gradient based on where the displacement-distance curve projects to a zero displacement value. The predicted fault tip location is seemingly consistent with the seismic image, as there are truncated reflectors below the fault along this point but continuously folded horizons above. The ability to predict this location may be useful in cases where the delineation of a petroleum trap relies on the position of the fault tip. This approach may prove particularly useful in structures in which seismic reflection data quality near the fault tip is poor; since fault-propagation fold front-limbs are often steeply dipping (and difficult to image in seismic reflection), this situation is common for this class of structures. Special care must be taken to account for faults that propagate through growth stratigraphy or unconformities, as they will display more complex displacement patterns; specifically, fault propagation through the pregrowth/growth transition will be manifest as a decrease in displacement and displacement gradient, the details of which are dependent on sedimentation and fault propagation rates.

In some cases, the faults may propagate through the folded front-limb to the earths surface, forming what is typically called a breakthrough fault-propagation fold [Suppe and Medwedeff, 1990; Shaw et al., 2005]. These structures still display the folding associated with their fault-propagation folding history (Figure 2.11A), but the hanging-wall is translated up the fault ramp due to additional displacement (Figure 2.11B). This results in observed displacements that reflect the contributions from both parts of the structure's history; the expected negatively-sloping displacement/distance relationship due to fault propagation folding, which is offset by the amount of displacement accrued after the fault broke through to the surface. Thus, on a displacement/distance plot, a breakthrough fault-propagation fold has a negatively sloping region that transitions at greater distance up the fault to a roughly

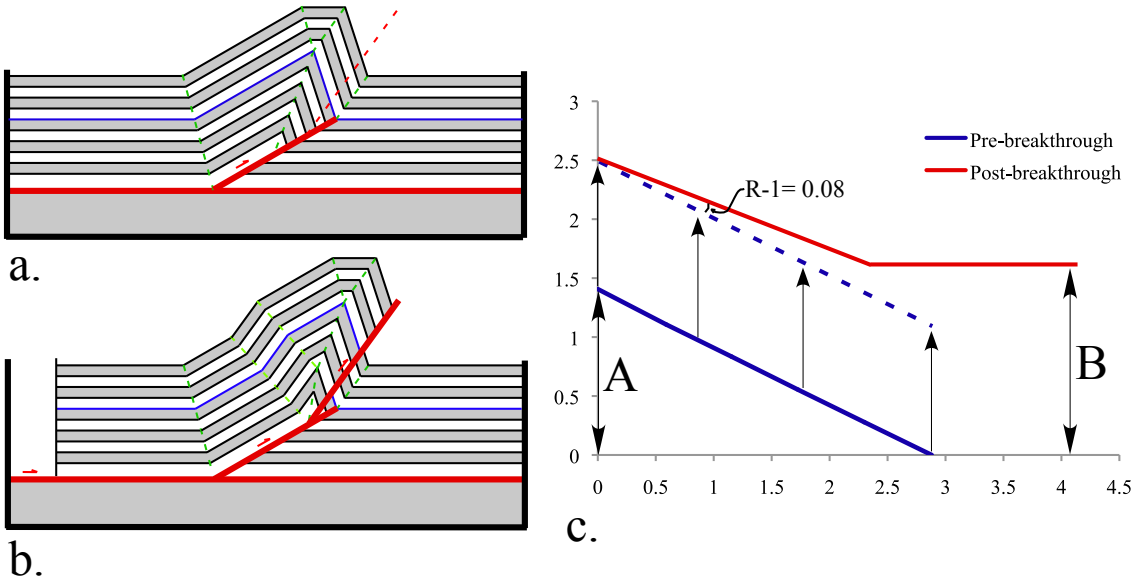


Figure 2.11: Kinematic model of a fault-propagation fold just prior to (*(a)*) and after breakthough (*(b)*). *(c)* Distance-displacement plot for *a* (blue) and *b* (red), illustrates that the breakthough fault-propagation fold by amount of displacement (B) preserves evidence for fault-propagation folding, with a slight modification of the slope due to fault-bend folding (R-1 = 0.08 for this fault model geometry).

horizontal line reflecting the slip that occurred after breakthrough (Figure 2.11C). The amount of slip that occurred after the breakthrough is defined by the height of this horizontal segment of the displacement/distance curve, and the maximum amount of slip that occurred during fault propagation folding can be estimated by the total slip minus the breakthrough slip, after accounting for any fault-bend-related changes in displacement. Notably, in these breakthrough structures the place where the negatively sloping portion of the displacement/distance curve would intersect with the X-axis corresponds to a fault tip position that is above the land surface or seafloor at the time of deformation. Thus, even in cases where the displacement/distance plot is incomplete due to poor data one can often distinguish fault-propagation folds that have and have not broken through. We illustrate the patterns of displacement in a breakthrough fault-propagation fold using an example from the Sierras Pampeanas

region of Argentina. The seismic image defines this structure as a tight, asymmetric fold with a steep forelimb fold that is not associated with a fault bend (i.e., is not a fault-bend fold) (Figure 2.12A). Measurement of the displacement variation with distance indicates a negative linear trend, which is consistent with the interpretation of this structure as a fault-propagation fold (Figure 2.12B). Although the data quality is insufficient to define the displacements above horizon A, the projection of the negatively sloping trend indicates that the location where displacement would reach zero is substantially above the land surface (Figures 2.12A and B). Thus, this structure can be reasonably interpreted as a breakthrough fault propagation fold, with up to 800 meters of slip occurring after the fault had broken through.

### 2.4.7 Applications to more complex structures

Previous sections have outlined the predicted displacements for different contractional fault-related folding styles and illustrated that these displacement/distance relationships are observed in natural structures from a variety of tectonic settings. Here, we illustrate the application of this method to structures with more complex deformation histories to highlight the utility of displacement/distance measurements in defining the structural style and history of displacement in structures that combine different fault-related folding processes.

Our example consists of two thrust sheets and associated fault-related folds from the deepwater fold-and-thrust belt of the Niger Delta (uninterpreted and interpreted seismic profiles, Figures 2.13 and 2.14). The hinterland structure (hereafter referred to as A) has a distance/displacement profile characterized by a region at the base of the fault with increasing displacement, a constant-displacement region in the middle of the fault, and decreasing displacement along the uppermost fault that is associated with a fault bend (Figure 2.15B). This pattern suggests that this structure involves

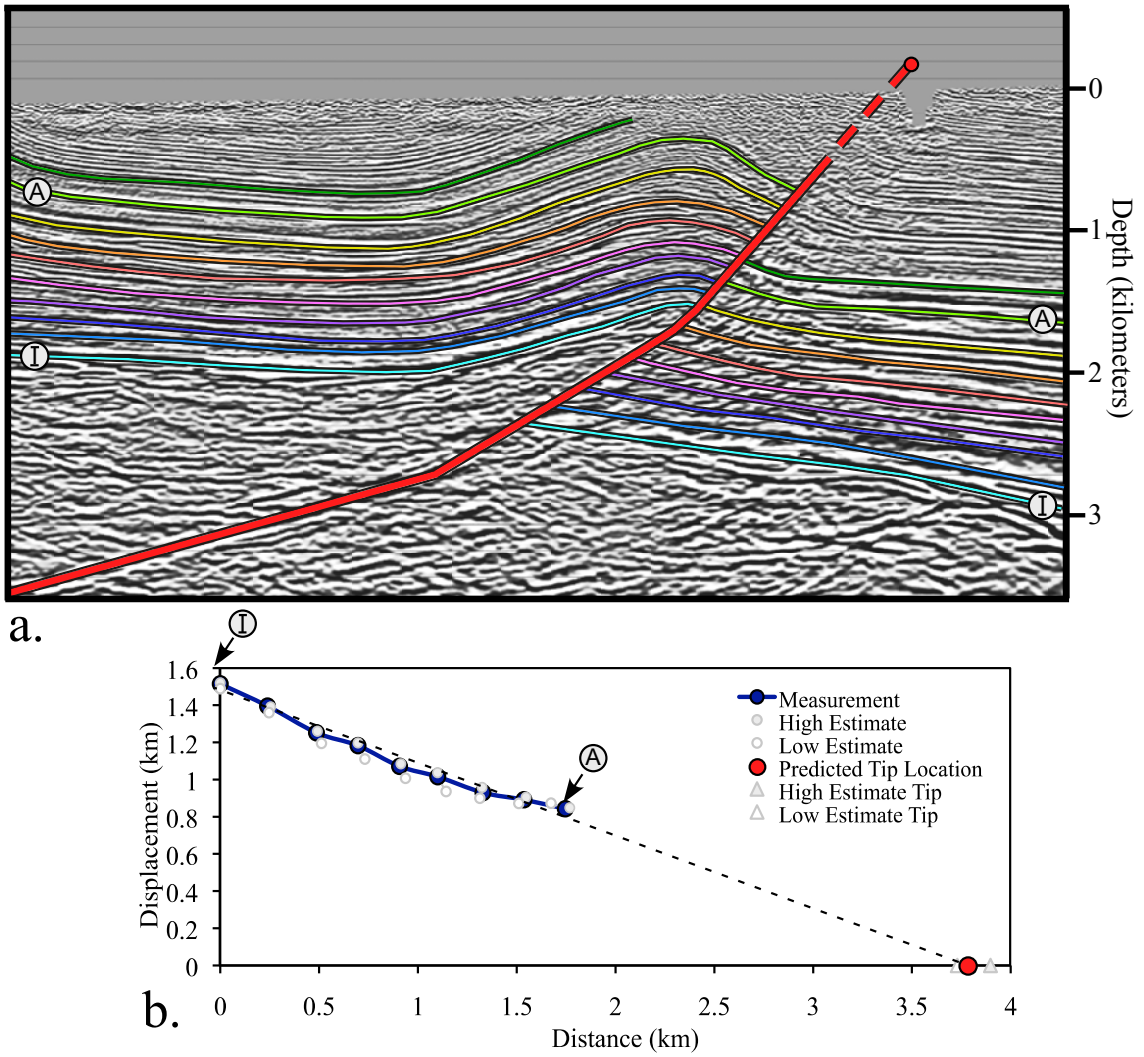


Figure 2.12: *(a)* Seismic reflection profile of a breakthrough fault-propagation fold from the Sierras Pampeanas, Argentina, with fault (red) and stratigraphic layers (A-I) interpreted, and predicted fault tip location (red point). *(b)* Measured displacement-distance relationship (blue), with minimum (white) and maximum (gray) estimates for layers A-I. Linear fit projects the fault tip location (red point). Data from Shaw et al., 2005, courtesy of BHP.

components of fault-bend folding and shear-fault-bend-folding. The upward increasing displacements at the base of the ramp are consistent with shear fault-bend folding in the back-limb of the structure associated with movement of hanging-wall strata above the fault bend defined by the base of the thrust ramp. The increasing displacement gradient occurs from horizons A to B, consistent with the region of shear defined by shear fault-bend folding theory. Based on the theory, the top of this shear interval is identified by the stratigraphic horizon (F) that intersects the fault at the location where the anticlinal axial surface (S') also meets the fault (Location (1) in Figure 2.14). Above this sheared interval, the displacement/distance plot indicates a constant displacement between layers B and D, which suggests that parallel folding occurs in this region. The region above this, from D to A, is characterized by a linearly decreasing displacement gradient. The location of this decrease in displacement is coincident with an anticlinal bend in the underlying fault, which suggests that fault-bend folding may account for at least part of this decrease in displacement. A fault dip change from 38° to 20° and displacement below the bend of 1.17 km, as observed from the seismic reflection data (2), predicts a gradient in displacement of greater than 0.33, or 19°. The rest of the decrease in displacement may be due to distributed shear in the front-limb; there are two compelling reasons that this may occur. This fault geometry is slightly beyond the boundary of the solution space for fault-bend-folding, which is to say that the folding due to this fault geometry cannot be modeled by preserving layer thickness and area, and thus, distributed layer thinning and thickening processes are required. Additionally, since these layers consist of weakly-lithified, near sea-floor sediments (confirmed by the observation that the upper detachment of the fault was the paleo-seafloor, indicated by the sediments that onlap onto the front-limb and exhibit geometries characteristic of drape sedimentation, 3), it is not surprising that they would not deform strictly in accordance with

fault-bend-folding theory, as the assumptions of the preservation of layer thickness and accommodation of folding by a flexural slip mechanism may not be preferred in weakly-lithified sediments. Despite these modest differences, the predicted decrease in displacement from the fault-bend fold theory clearly captures the first order displacement patterns in this structure.

By the same method of analysis, the foreland structure (B in Figure 2.14) exhibits constant displacement at depth, and decreasing displacement along the uppermost part of the fault that is not associated with a fault bend. This pattern of displacement is consistent with components of both standard fault-bend folding and fault-propagation folding. The region of constant slip on the lower portion of this thrust ramp is consistent with the back-limb of the structure forming by standard fault-bend folding. Notably, the beds in the back-limb of the structure are parallel to the underlying fault (fold limb, 4), consistent with standard fault-bend folding and distinct from structure A, which involved a component of shear fault-bend folding. On the upper part of thrust ramp B, the distance/displacement plot shows a negative slope reaching zero displacement at a distance of about 6 km (Figure 2.15A). Unlike in structure A, the decrease in displacement is not associated with an anticlinal fault bend (in contrast, a minor synclinal bend is present, indicated by 5), suggesting that the decrease in displacement observed in structure B is due to fault-propagation folding. Based on the interpretation of the forelimb of the structure as a fault-propagation fold, the fault tip (the location where displacement along the fault decreases to zero) would be located just below horizon F (6). This is broadly consistent with the observation of offset layers below this point, and continuous, folded layers above it. Based on the curved nature of the forelimb fold limb, changes in layer thickness, and the upward decrease in bed dips, this structure is interpreted as a trishear fold [Erslev, 1991; Allmendinger, 1998, and others]. Moreover, the growth strata indicate that

these two faults are part of a break-forward sequence. Thus, displacement along the foreland structure (B) imbricates and re-folds the hinterland structure (A). Despite this complexity, the displacement/distance plots maintain recognizable signatures of the basic fault-related folding components that generated these structures.

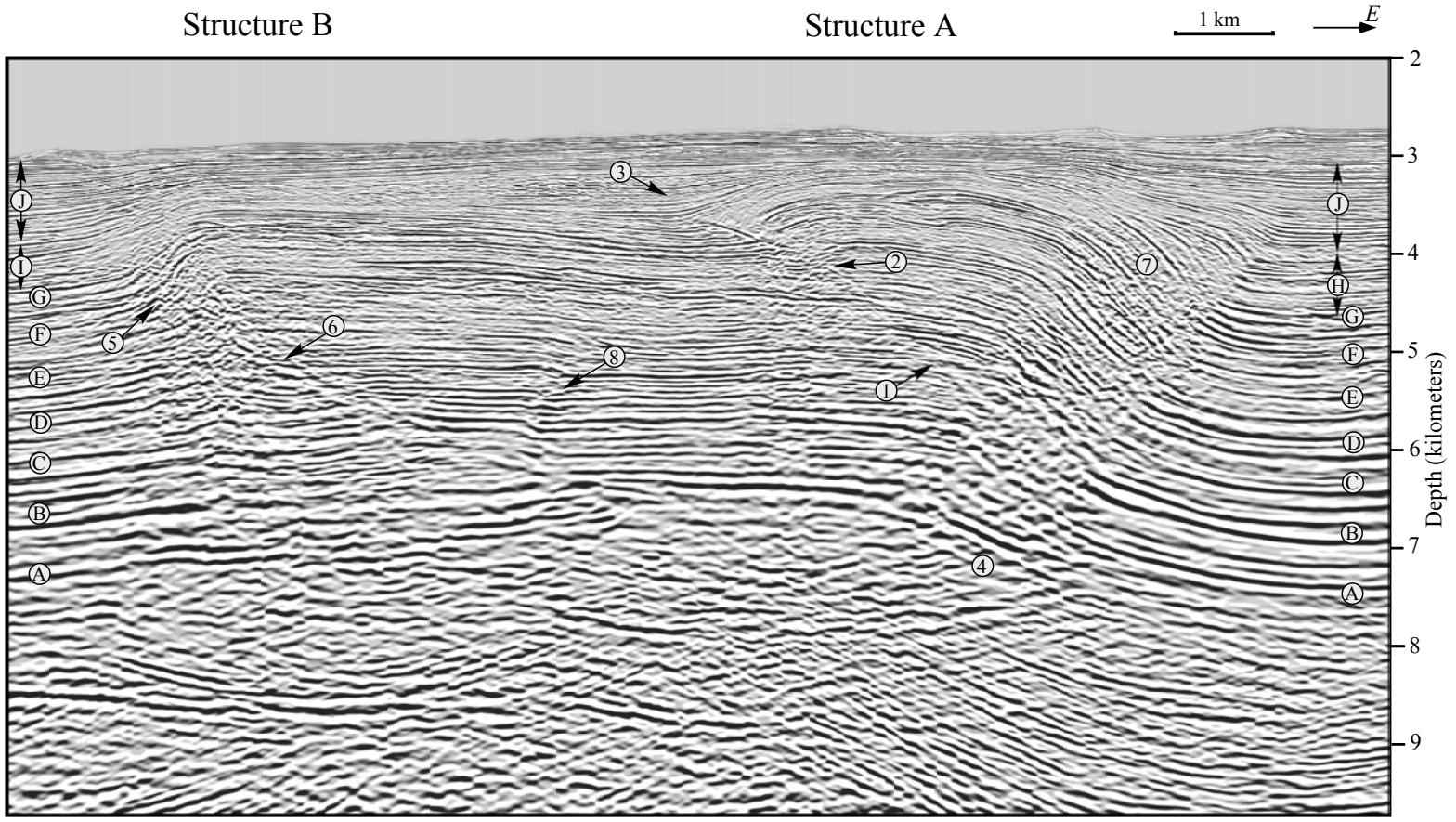


Figure 2.13: Seismic reflection profile of two contractional fault-related folds offshore Niger Delta, Nigeria. Pregrowth layers (A-G), growth layers (H,J), drape layers (I), and faults are denoted. Arrows point to features discussed in the text: (1) intersection of axial surface and fault, indicating the top of the shear interval, (2) anticlinal fault bend, (3) drape sedimentation, (4) fold limb, (5) projected fault tip location, (6) synclinal fault bend, (7) growth triangle, (8) minor backthrust. Data is owned and provided courtesy of CGGVeritas, Crawley, UK.

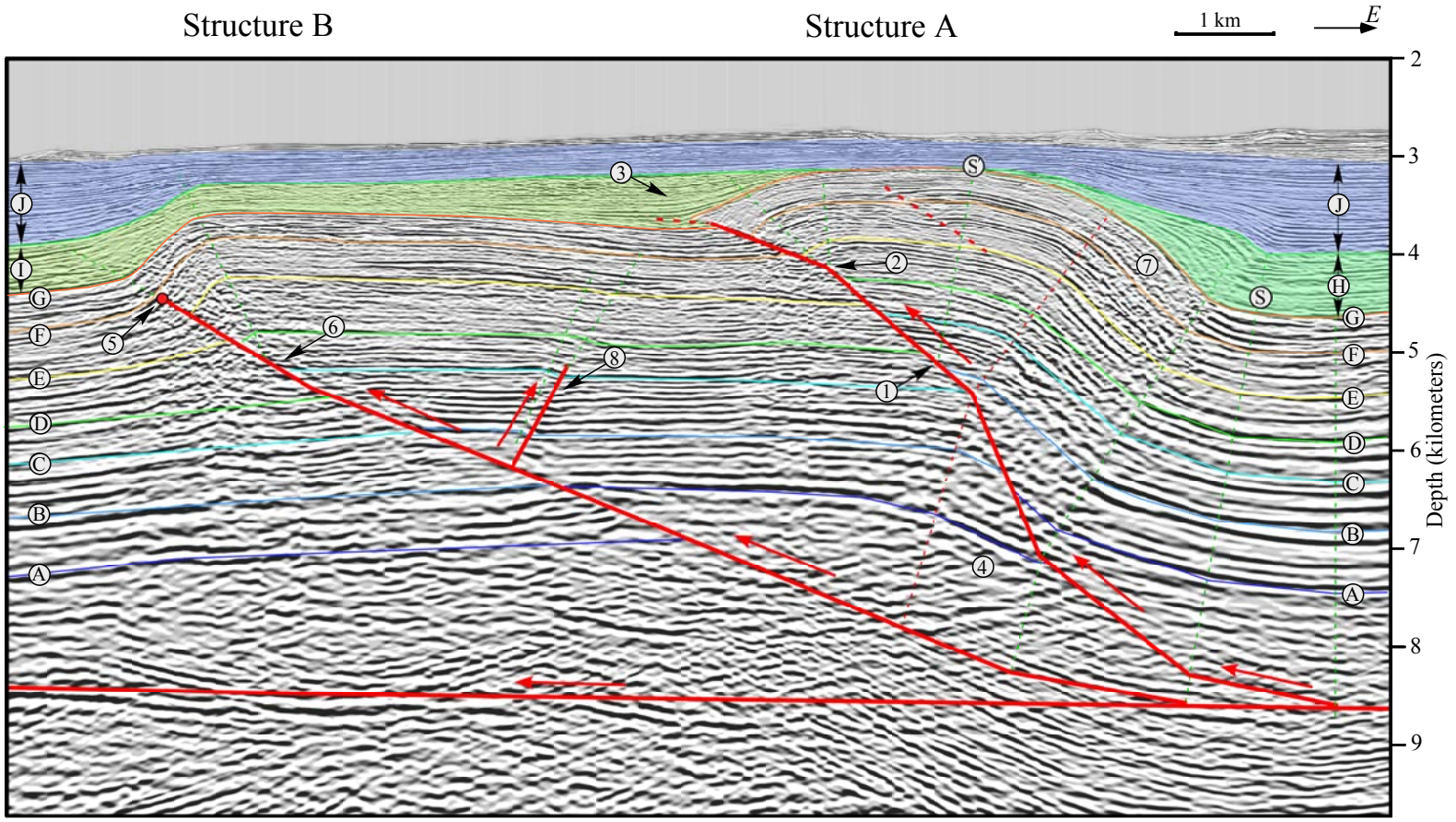


Figure 2.14: Interpreted seismic reflection profile of two contractional fault-related folds offshore Niger Delta, Nigeria. Annotations as described in Figure 1.13. Data is owned and provided courtesy of CGGVeritas, Crawley, UK.

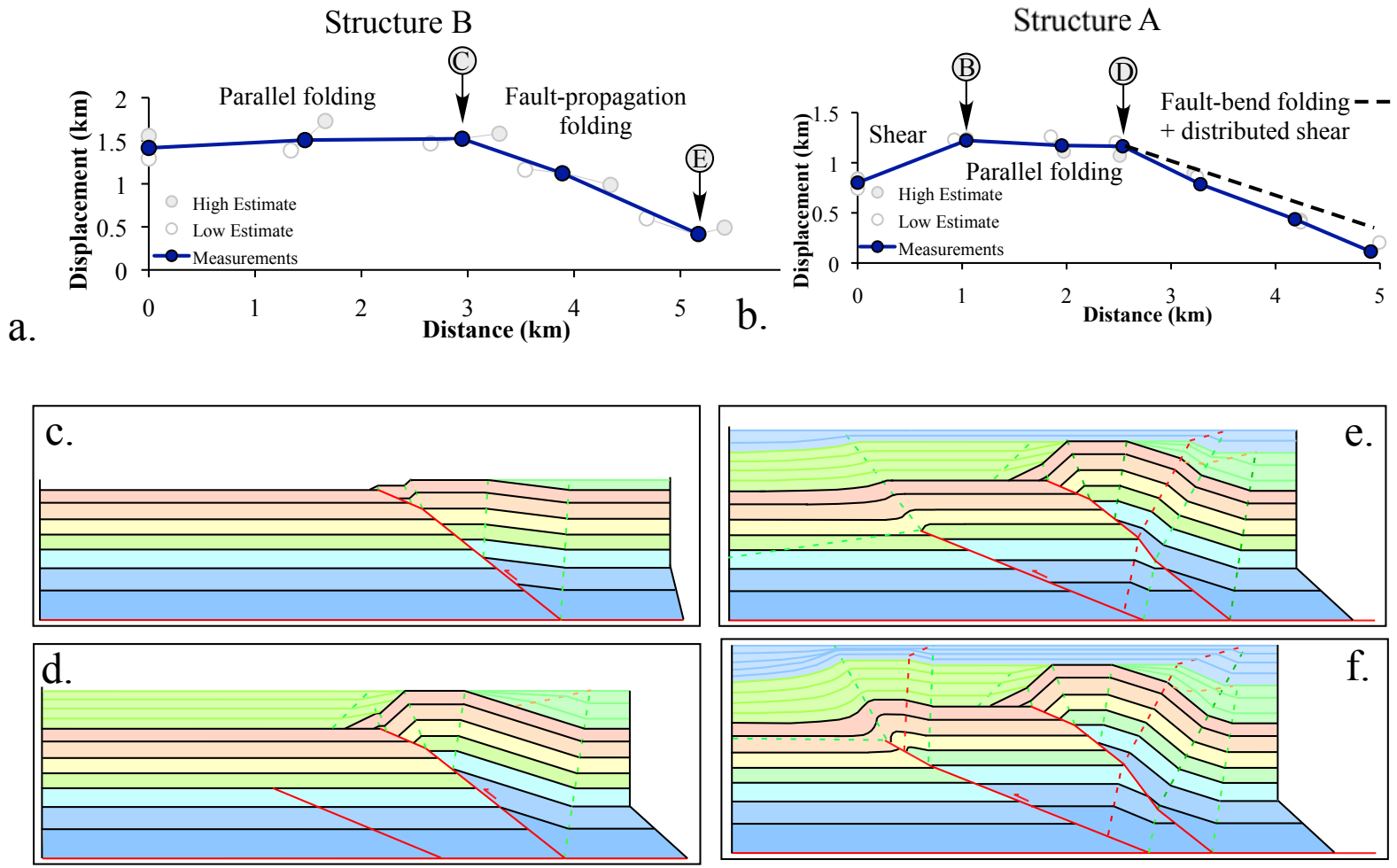


Figure 2.15: *(a)-(b)* Displacement-distance plots for the structures analyzed in figure 13. *c-e* sequential kinematic model of the development of these structures, with structural styles determined from observations from the distance-displacement plots.

Based on the insights from the distance/displacement plots and growth strata, we generated a balanced kinematic model of both structures (Figure 2.15C-F). Based on the detailed observations from structure A, it was modeled as a shear fault-bend fold, with the shear interval and fault geometry defined by observations from the seismic reflection data and distance/displacement plot (Figure 2.15B). After displacement was completely accumulated on the structure A, displacement was modeled on the foreland structure as a fault-bend-fold back-limb with a fault-propagation-fold front-limb, based on the observations made from the distance/displacement plot (Figure 2.15A). Many of the parameters necessary to model the front-limb of structure B as a trishear fault-propagation fold may be constrained from the distance/displacement plot. The base of the propagating section is inferred to be the location of the transition between constant displacement and decreasing displacement. The location of the fault tip is also evident, as it is the location where displacement reaches zero. The distance between those two points represents the distance that the fault propagated during this phase of its history. Additionally, the amount of displacement at the base of this segment can be easily measured. These two observations combine to give the propagation-to-slip ratio ($P/S$) of 3.96 for structure B; knowledge of this value provides an important input constraint for modeling this structure as a trishear fault-propagation fold. Based on these observations and the observed dip of the fault, a trishear fault-propagation fold front-limb model was generated to model this structures geometry, concurrent with fault-bend-folding in the back-limb (Figure 2.15E-F). This model invokes the following series of events for this structure:

1. The fault propagated as a fracture from the lower detachment to the base of the fault-propagation interval,

2. As displacement on the fault commenced, the back-limb deformed as a fault-bend-fold while with tip of the fault propagated upwards through the stratigraphic

section, and,

3. The fault tip propagated to its currently observed location when the lower portion of the fault had accumulated the observed, maximum amount of displacement.

As the only observations that went into the construction of the kinematic models were displacement/distance relationships, fault geometries, and stratigraphic thicknesses, comparison of the resulting fold geometries with the fold shapes observable in the seismic reflection data provides an objective test of the utility of this approach. The pre-growth back-limb fold geometry of structure A is remarkably consistent with the fold observed in the seismic reflection data, as the limb dips and widths of the original fold and imbricated panels are both well represented in the model. The geometry of the growth strata over this back-limb is also consistent with the observed growth geometries of layers H and J. The modeled front-limb of structure A is also consistent with the location, size, and dip direction of the forelimb in the natural example.

However, the front-limb of the natural structure is also geometrically dissimilar in some ways from the model; this is likely because these sediments were not deeply buried, and therefore preferentially deformed with more distributed shearing rather than flexural slip. Additionally, the thickness of the drape sedimentary package (I) is thinner in the natural example; this is due to a combination factors, including the lower structural relief observed than modeled for Structure A, and an oversimplification of the depositional environment (it has been commonly observed in offshore settings that sediments tend to pond behind bathymetric highs (such as structure A), resulting in sediment-starved basinward regions [e.g., Shaw et al., 2004]), and that some of the deformation on structures A and B may have been concurrent. For structure B, the deep fold panel (4) and front-limb trishear geometries are well represented in the model geometry. Additionally, the modeled growth strata deposited over this fold thickens over the back-limb and front-limb are consistent with the strati-

graphic thickening and fold geometries observed in the seismic reflection data. The modeled folding due to the minor synclinal bend in fault B (5) is not observed in the data, which is perhaps due to the presence of a minor backthrust (8), which allowed the uplift and folding to be accommodated over a broader region. In summary, we suggest that the modeled structural geometries based on parameters defined by the displacement profiles are generally consistent with the patterns of folding and faulting expressed in this natural example. Specifically, the observed displacement profiles help characterize these structures as complex fault-related folds involving components of fault-bend, shear fault-bend, and fault-propagation folding. Moreover, in cases where the modeled geometries are locally inconsistent with the natural folds, this helps identify regions of the natural structures where deformation may be accommodated by alternative deformation mechanisms (e.g., non-parallel folding) or secondary structures that are not represented by the models.

## 2.5 CONCLUSIONS

We present a quantitative method for relating the displacement measured along a contractional fault to the style of folding deformation present in a given structure. We include results from various styles of fault-related folds by comparing the expected displacement-distance relationships to observations from seismic reflection datasets in a variety of tectonic settings. We then apply this method to a complex structure, illustrating that this approach can be successfully used to gain insight into the mixed structural styles that may be present. By this approach, we are able to identify shearing intervals, parallel folding intervals, and fault-propagation folding intervals, and to observe the effect of fault bends in displacement distributions. Additionally, by generating a balanced structural model based on our interpretation, we are able to

compare the fold and growth geometry of the model with observations in the seismic reflection data, confirming the validity of our interpretation. We suggest that this approach has value for the structural interpretation of seismic reflection data, as it can help to elucidate the styles of fault-related folding deformation present in a given contractional structure. The method can also serve as a somewhat independent way of interpreting structural style, which, when combined with geometric observations, will lead to the development of detailed and accurate structural models of contractional fault-related folds.

## 2.6 ACKNOWLEDGEMENTS

We thank CGGVeritas for their provision of this data and support of the project, which was instrumental. We also wish to offer special thanks to ExxonMobil and Chevron, which supported this research. We are also indebted to Landmark Graphics Corporation, which provided software that was critical to this research through their Strategic University Alliance Grant Program (Agreement 2007-CONT-005191).Generic Mapping Tools (Wessel and Smith, 1991) was used to generate Figure 4. This research was also funded by the Petroleum Research Fund (ACS PRF 48385-AC8) and National Science Foundation (NSF-EAR 0711220).

# Chapter 3

# Factors that control the development of fault-bend versus fault-propagation folds: Insights from mechanical models based on the discrete element method (DEM)

## 3.1 Abstract

We investigate the role and relative importance of a range of geometric and mechanical factors in the development of contractional fault-related folds, with an emphasis on defining the factors that promote the development of fault-bend and fault-propagation folds. We construct a series of discrete-element mechanical models in order to test the effects of fault dip, bulk material strength, mechanical layer anisotropy and layer spacing, sedimentation rate, and boundary conditions on the style of fault-related fold that develops. We find that fault-bend folding is most prevalent at low fault ramp dips and with thinly-spaced mechanical layers and strong layer strength contrasts. In contrast, increased friction on the upper detachment and a stationary foreland wall, which resists displacement on an upper detachment, favor the development of fault-propagation folds. Additionally, higher fault dips, more widely-spaced mechanical

layers, and decreased relative layer strength favor changes in which shear is localized during the growth of structures. This leads to structures that deform by a mixture of the fault-bend and fault-propagation folding styles. Observations of the distortional strain that develop in the model provide insight into the relationship between the different deformation mechanisms, such as flexural slip and localized shear, that accommodate structural growth and ultimately determine fault-related folding style. Thus, these models provide a context for understanding how rock and fault properties influence the whether structures evolve as fault-bend or fault-propagation folds, or as combinations of these end members. We apply these insights to interpret two natural examples from the offshore Niger Delta outer fold-and-thrust belt that exhibit changes in structural style through time as a result of changes in fault properties and syntectonic sedimentation.

## 3.2 INTRODUCTION

Fold and thrust belts have long been recognized to exhibit a variety of fault-related folding styles [Rodgers, 1990, 1991; Poblet and Lisle, 2011], yet the mechanical conditions that contribute to these differences are not well understood. While some fold-and-thrust belts are characterized by a predominant structural style, in most cases the two most common classes of fault-related folds - fault-bend and fault-propagation folds - are often found in close spatial association with each other (Figure 3.1). Given this proximity, it is evident that both types of structures developed under very similar lithologic and regional stress conditions. This suggests that the mechanical and geometric properties that favor the development of one of these structural styles over another are subtle and warrant more detailed investigation. To that end, we have undertaken a study to investigate the role of mechanical and geometric conditions in

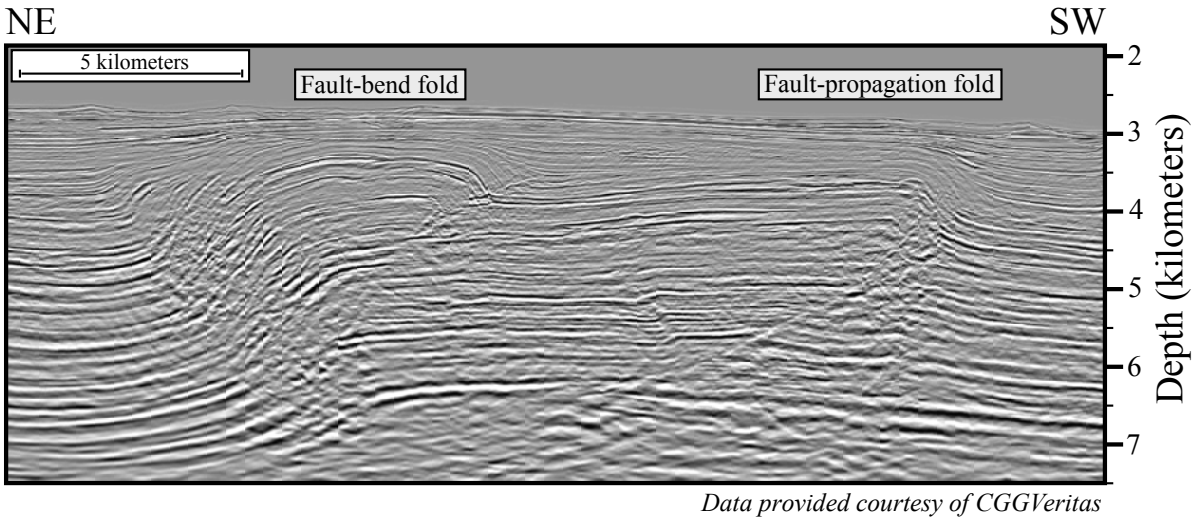


Figure 3.1: Seismic reflection profile from the offshore Niger Delta, showing structures that are classified as fault-bend and fault-propagation folds. Data is owned and provided courtesy of CGGVeritas, Crawley, UK.

the development of both fault-bend and fault-propagation folds.

We model fold development with the discrete element method (DEM) to identify the conditions under which slip on an upper detachment produces a fault-bend fold. Moreover, we explore cases in which slip on the upper detachment is inhibited, resulting in shortening being accommodated by internal deformation mechanisms, including fault-propagation folding. We investigate the sensitivity of this transition to a range of material strengths, mechanical layer thickness and relative mechanical layer strengths, syntectonic sedimentation rates, fault friction values, and boundary conditions. Finally, we analyze natural examples from the offshore Niger Delta in the context of our model results.

Understanding the characteristics that lead to the development of one of these structural styles over another is valuable to many applications, including geologic mapping and regional tectonic studies, seismic hazard assessment, and petroleum geology. Fault-bend and fault-propagation fold structures have distinct patterns of

fault displacement and fold shapes, which influence the amounts of crustal shortening and uplift that they accommodate. Proper identification of these structures is thus important to properly characterize upper crustal shortening in fold-and-thrust belts, a process often involves the application of a specific fault-related folding theory to quantitatively assess these structures. This is of particular importance in the interpretation of seismically active blind thrust faults, where fault slip rates are generally inferred from patterns of uplift above fault-related folds [Shaw and Suppe, 1994; Allmendinger and Shaw, 2000; Pratt et al., 2002; Shaw et al., 2002; Dolan et al., 2003; Yue et al., 2005; Gold et al., 2006; Hubert-Ferrari et al., 2007]. Relating uplift to fault slip requires proper identification of fault-related folding styles, as fault-bend and fault-propagation folds exhibit markedly different relations between these properties. Finally, proper identification of fault-related folds is useful to petroleum geology applications because these distinct classes of structure often have different trap geometries and reservoir characteristics. In exploration settings, data are often sparse or incomplete, so the style of fault-related folding is difficult to assess. This leads to significant uncertainties in subsurface trap geometries and can yield an incomplete or inaccurate history of the structural growth. These factors can lead to large inaccuracies in the assessment of reservoir volumes or hydrocarbon charge pathways.

Our research seeks to address these concerns by studying the particular mechanical and geometric conditions that favor the development of fault-bend versus fault-propagation folding. Insights from our mechanical models enable the use of stratigraphy, rock properties, fault geometries, and sedimentation rates to inform the classification and interpretation of natural structures. In practice, this generally involves the assessment of structures that are poorly imaged, and helps reduce uncertainties in deciding which kinematic model is more appropriate to apply in the interpretation of the structure. These choices, in turn, help to refine assessments of crustal

shortening, active fault slip rates, and petroleum trap and reservoir characteristics that are of academic and practical concern. Finally, since the mechanical conditions tested in this study give rise not only to structures that can be classified by the end-member kinematic fault-bend and fault-propagation folding styles, but also a range of intermediate structural styles, they provide a framework for interpreting natural structures that have a geometry that are intermediate or transitional between these end-member styles, and thus not well characterized by existing kinematic models.

### 3.2.1 Fault-related Folding Kinematics

It has long been recognized that the development of folds is often related to the displacement of rocks over underlying faults [Rich, 1934; Rodgers, 1950, and others]. Different relationships between the geometry of underlying faults, the deformational history of the structure, and the geometry of the subsequent fold that develops have been described. This study is focused on two of the most common types of fault-related folds, specifically fault-bend folds and fault-propagation folds.

The first studies to relate folding to the displacement of rocks over non-planar faults were conducted in detailed analyses of foreland fold and thrust belt structures in the Appalachians [Rich, 1934; Rodgers, 1950]. Based on constraints of constant cross-sectional area and layer thickness throughout the folding process, the quantitative relationship between fault shape and fold shape was derived by Suppe [1983], and has subsequently been successfully applied in the interpretation of fold and thrust fault geometry in a variety of fold and thrust belts [e.g., Shaw et al., 2005, and many others] that have relevance to petroleum applications [Rowan and Linares, 2009; Corredor et al., 2005a] and the interpretation of active structures [Shaw and Suppe, 1994; Pratt et al., 2002; Shaw et al., 2002; Dolan et al., 2003; Yue et al., 2005; Hubert-Ferrari et al., 2007].

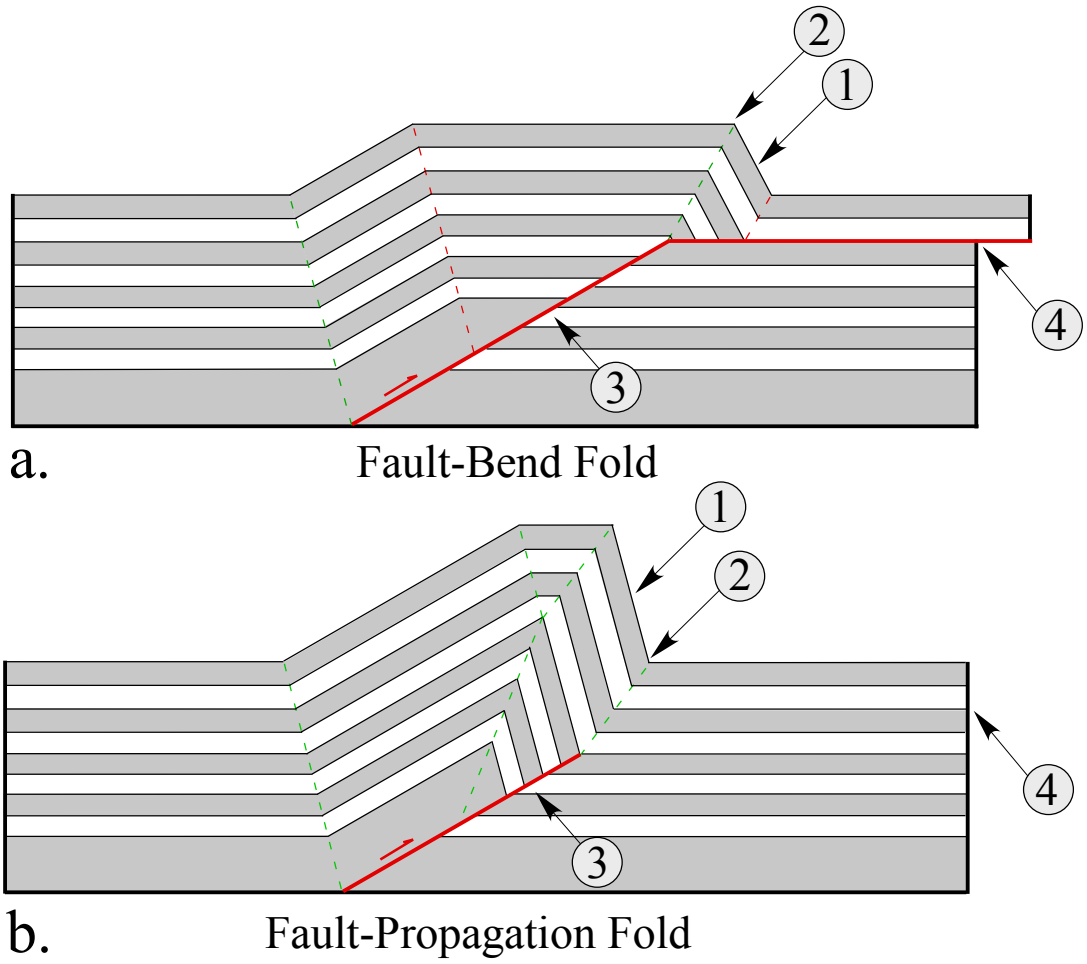


Figure 3.2: (*a*) Kinematic model of a fault bend fold (Suppe, 1983), characterized by relative symmetry between front and backlimb dips and widths (1), an active anticlinal axial surface tied to the top of the ramp (2), constant displacement along the fault ramp (3), and a finite displacement of material translated into the foreland along an upper detachment (4). (*b*) Kinematic model of a constant thickness fault propagation fold (Suppe and Medwedeff, 1990), which is distinguished from the fault bend fold by having a steep, narrow forerontlimb relative to the backlimb (1), an active synclinal axial surface tied to the top of the fault ramp (2), a decrease in displacement toward the fault tip (3), and the displacement is consumed within the structure (4).

While fault-bend folding has been widely and successfully applied to a range of structures, geologists have also recognized that some folds have different geometric relationships with underlying thrust faults. One of the most widely documented of these alternative fault-related-folding styles is fault-propagation folding, in which folding occurs in advance of a propagating fault dip. These folds accommodate differential displacement along the fault, as slip decreases to zero at the tip of the propagating fault, which is pinned to a synclinal fold. Structures fitting these criteria exhibit a range of geometries and, as a result, a number of models have been developed to describe their kinematics and geometric relationships. The most commonly applied of these kinematic theories are constant-thickness and fixed-axis fault-propagation folding [Suppe and Medwedeff, 1990] and trishear fault-propagation folding [Erslev, 1991; Allmendinger, 1998]. Other kinematic models have been developed to describe particular sub-classes of fault-propagation folds or to explain particular observations [Chester and Chester, 1990; Kattenhorn, 1994; Narr and Suppe, 1994; McConnell, 1994; Erslev and Mayborn, 1997; Spang and McConnell, 1997; Tavani et al., 2006]. Collectively, these kinematic models have been successfully applied to the interpretation of a variety of regional structural studies [Zapata and Allmendinger, 1996; Cardozo et al., 2005] active structures [Allmendinger and Shaw, 2000; Gold et al., 2006] and structures relevant to petroleum exploration [Corredor et al., 2005a; Bilotti et al., 2005].

There are several characteristics that distinguish fault-bend from fault-propagation folds (Figure 3.2) that can help to guide the classification of natural structures. Fault-bend folds tend to have forelimbs and backlimbs that are relatively symmetric in limb width and dip, while fault propagation folds are characterized by long, gently-dipping backlimbs and narrow, steeply-dipping forelimbs (Figure 3.2, 1). There are also important differences in where the folding is localized between these two classes

of structures. At the top of the ramp in an anticlinal fault-bend fold, an anticlinal axial surface remains fixed to the fault bend and marks the location where material is folded and incorporated into the front limb. In contrast, the upwards projection of the fault ramp in a fault-propagation fold is tied to a synclinal axial surface that forms as slip at the tip of the fault decreases to zero (2). These two structural styles are also distinguished by differences in displacement along the fault, as fault-bend folds display constant slip along fault segments and changes in slip at fault bends, where as fault-propagation folds are defined by a decrease in displacement that reaches zero at the fault tip (3) [Hedlund, 1997; Hughes and Shaw, 2012]. Finally, fault displacement continues out along an upper detachment in fault-bend folds, while fault-propagation folds accommodate all of the shortening by internal deformation, without slip along an upper detachment (4).

In addition to classical fault-propagation folding, there are other mechanisms for accommodating shortening through internal deformation above a thrust ramp. Most notably, these include forelimb shear and layer thickness changes [Suppe et al., 2004], and fault-arrest folding [Julian and Wiltschko, 1983; Fischer et al., 1992; Armstrong and Bartley, 1993; Hedlund et al., 1994; Thorbjornsen and Dunne, 1997] and fault-displacement-gradient folding [Wickham, 1995], where the fault tip location is stationary and folding occurs due to variations along the ramp in displacement. Many of the mechanical models that develop will involve aspects of these different deformation styles, which will be noted.

### 3.2.2 Mechanical influences on fault-related folding

Existing kinematic models are based on physical assumptions such as conservation of bed length or cross-sectional area, and their kinematics imply strain distributions and deformation mechanisms. These models, however, do not explicitly contain mechan-

ical considerations. Recent studies examining the strain distributions in kinematic models [Salvini and Storti, 2001] and comparing these predictions with field observations of strain [Hedlund et al., 1994; Tavani et al., 2005; Masini et al., 2010] have started to explore the mechanical implications of the kinematic models. Additionally, previous mechanical modeling studies have investigated the role of various mechanical properties on the development of fault-bend folds in analog models [Chester et al., 1991; Bonini et al., 2000] and in numerical mechanical models, using the finite-difference [Erickson et al., 2001], finite element method [Smart et al., 1999], discrete element method [Benesh et al., 2007; Benesh, 2010] and analytical models [Wiltschko, 1979a; Berger and Johnson, 1980; Goff et al., 1996]. Fault-propagation folds have also been modeled using the finite element method [Cardozo et al., 2003] and discrete element method [Cardozo et al., 2005; Hardy and Finch, 2006, 2007]. While the role of mechanical strength differences in stratigraphy, frictional considerations, fault dip, and sedimentation rate have been invoked as explanatory in contributing to the changes in between styles in natural structures, and some of these influences have been tested individually previous studies, the relative importance of each in the transition between fault-bend and fault-propagation folding has not been fully investigated, and as such, is the objective of the current study.

## 3.3 Modeling Approach

### 3.3.1 The Discrete Element Modeling (DEM) method

The mechanical modeling method we employ in this study is the two-dimensional discrete element modeling, or DEM, approach. We use the Particle Flow Code in 2 Dimensions (PFC2D) software package, distributed by the Itasca Consulting Group, which is based on the soft-sphere discrete element modeling method described by

Cundall and Strack [1979]. The material is modeled as a series of elastic disk-shaped particles that interact with each other and prescribed model boundaries. Particle interactions are governed by elasticity (defined by a Young's modulus) in compression that resists particle overlap due to a restoring force that is linearly proportional to the overlap distance, and a frictional strength (defined by a coefficient of sliding friction) that resists shear motion (Figure 3.3A). Additionally, contact bonds are applied to provide cohesive strength in tension and shear, and the particles are subject to a gravitational body force. Elastic, user-defined walls confine the particles and serve as the mechanism that drives deformation of the particle assembly in the model.

Many field observations of fault-related folds have documented the prevalence of small-scale folds, fractures, and flexural slip surfaces. This highlights the appropriateness of a Coulomb frictional constitutive modeling approach, such as that employed by DEM, for investigating the deformation of upper crustal rock materials. Moreover, bonds between adjacent particles in the models may break and reform as deformation progresses. Thus, this approach is particularly well-suited to modeling large strain values and localized, emergent deformation, without having to deal with the challenges of mesh design and reconfiguration inherent to some other continuum modeling approaches. As we seek to observe the development of incipient faults and emergent deformation within the front-limb of deforming structures, this capability is essential for our study.

The discrete element modeling method has been applied to a wide range of problems in physics, granular mechanics, material science, and engineering. Within the geosciences, DEM been applied to a broad range of topics in granular mechanics such as the evolution of fault gouge development in sheared fault zones [e.g., Mora and Place, 1993; Antonellini and Pollard, 1995; Mora and Place, 1998; Morgan and Boettcher, 1999; Morgan, 1999; Guo and Morgan, 2004, and others]. Since the num-

ber of particles that may be simulated is limited by computation time, simulations of geologic processes at larger scales cannot be implemented with realistic particle sizes. However, bulk material may be represented by a particle assembly in which the individual particles are not representative of a physical discrete entity; in this case, the frictional, contact bonding, and elastic interactions between individual particles must be calibrated to represent the bulk material properties at larger spatial scales. The inter-particle strength properties may be scaled to bulk material properties by conducting biaxial failure tests on the samples to find their material strengths. Through this calibration approach, the mechanics and kinematics of larger-scale geologic deformation processes have been successfully modeled, including thin-skinned thrust fault evolution [Burbridge and Braun, 2002; Strayer et al., 2004; Hardy et al., 2009], extensional faulting and folding [Seyferth and Henk, 2006; Finch et al., 2004], basement-involved thrust fault-propagation folding [Finch et al., 2003; Hardy and Finch, 2006, 2007], detachment folding [Hardy and Finch, 2005], and the gravitational collapse of volcanic edifices [Morgan and McGovern, 2005b,a].

### 3.3.2 Material strength calibration

In order to realistically simulate the material strength of sedimentary rock sequences, we conduct a series of biaxial stress tests on numerical samples in order to calibrate the single-particle interaction values for particle stiffness, contact bond strengths, and sliding friction to ensure that they scale to the desired bulk material properties (Figure 3.3b). Particle sizes were chosen from a uniform distribution from 25-33 meters. All particles were assigned an average rock density ($\rho$) of 2600 km/m$^3$. Particle stiffness values of 7 x $10^9$ N/m were assigned for shear ($k_s$) and normal ($k_n$) stiffness, and the coefficient of sliding friction between particles ($\mu$) was assigned as 0.3. For the

standard material used in this study, contact bond values of 10 and 600 megapascals (MPa) for normal ($\sigma_n$) and shear ($\sigma_s$) contact bonds were applied using a Gaussian distribution with a standard deviation of 25% of the mean bond strength. Through these simulations, we deform the numerical samples by applying a prescribed confining stress, then increasing the applied stress by displacing the top platen downward until the sample reaches peak strength and fails (Figure 3.3c). The platen is displaced at a rate sufficiently slow that a quasistatic solution is attained. We then record the applied stress at which the numerical sample reaches peak strength and fails at a range of confining pressures from 0 to 150 MPa. We conducted three trials at each confining stress with different randomly distributed particle assemblages, and averaged the results. Plotting the peak stresses recorded for each of these confining stresses defines the shape of the Mohr-Coulomb failure envelope, Young's Modulus ($E$), and coefficient of internal friction ($\mu$) for this material (Figure 3.3d).

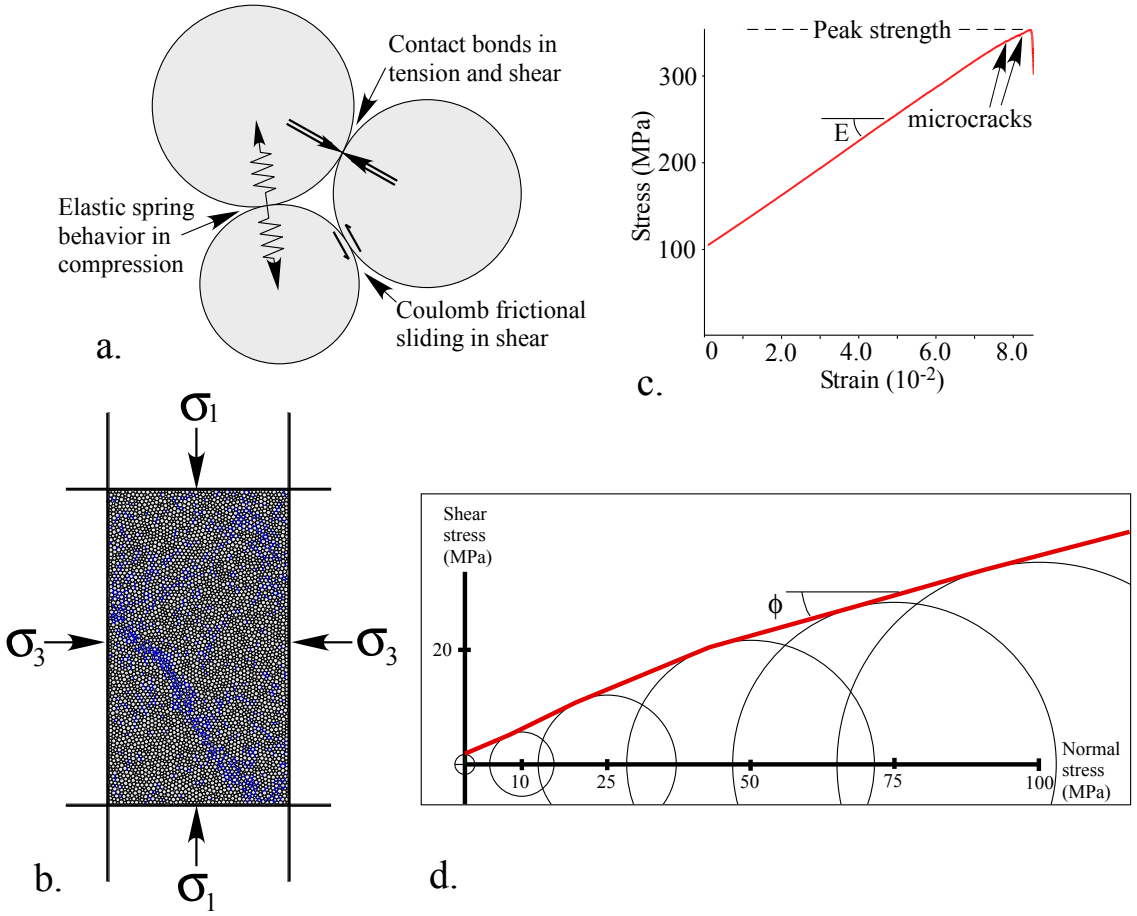


Figure 3.3: (*a*) Illustration of the interparticle interactions in the discrete element method. (*b*) Example of a numerical sample after a completed biaxial stress test at 100 MPa confining pressure, with microcracks (broken contact bonds) highlighted (blue). (*c*) The relationship between stress and strain for the biaxial test shown in (*b*), illustrating how the Young's Modulus (E) and peak strength are measured. (*d*) Compilation of averaged peak strength measurements at different confining stresses, defining the Mohr-Coulomb failure envelope for this material.

A calibration of these particle-scale parameters yielded a bulk aggregate material with average coefficient of internal friction ($\mu$) of 0.64 ($\phi = 32.6$), cohesion ($C$) of 8.3 MPa and Young's modulus ($E$) of 2.7 GPa. For the weaker material, all assigned properties were the same, except that contact bonds strengths were reduced by an order of magnitude, resulting in bulk material with a coefficient of friction ($\mu$) of 0.48 ($\phi = 25.4$), cohesion ($C$) of 4.3 MPa and Young's modulus ($E$) of 2.6 GPa. These values are within the range of natural laboratory measurements of rock strength [Byerlee, 1978], and are broadly consistent with the material strengths used in other discrete element modeling studies. The use of these material strength values results in the development of realistic structures at the basin scale. There are not significant surficial slumps that would indicate a material that was too weak, nor are there unrealistic gaps and crevices that would indicate that the material was too strong. The stronger set of material properties was emphasized for this study, as it was observed that these strengths are required for fault localization to occur in larger, fold-and-thrust-belt scaled models [Chapter 4], rather than the more distributed shear deformation that occurs with weaker material strengths; however, it will be demonstrated that the results of this study are fairly insensitive to absolute material strength within this range. Calibrated values of Young's modulus are at least an order of magnitude lower than laboratory experiments [Jaeger and Cook, 1976, p. 146], as has been employed in other discrete-element modeling studies [Saltzer and Pollard, 1992; Strayer et al., 2004; Hardy and Finch, 2006; Benesh et al., 2007; Hardy and Finch, 2007; Hardy et al., 2009; Benesh, 2010]; this is consistent with the finding that Young's modulus decreases for increasing sample scale [Bieniawski, 1984], suggesting that such values are appropriate for modeling large-scale tectonic deformation [Serafim and Pereira, 1983]. For a more complete description of the material strength calibration test, see Itasca [1999]; Strayer and Suppe [2002]; Hardy and Finch [2007].

In order to model heterogeneously layered and anisotropic stratigraphy, thin layers with much weaker material properties are embedded within the models in order to represent flexural slip surfaces. The particles in these layers have a uniform size distribution of +/- 25% of a mean size of 22 meters, and are assigned the same particle stiffness values as the material tested above, except that they have no resistance to sliding friction or contact bonds, in order to most accurately approximate the presence of flexural slip surfaces. In the case where the effect of stronger weak layers is investigated, weak contact bonds are established in this layer. The assigned interparticle bond strengths are 3 orders of magnitude lower than in the surrounding, stronger material.

### 3.3.3 Experimental setup for standard conditions

Our experimental setup consists of model boundaries that include a dipping fault ramp, horizontal surface that can serve as an upper detachment, and two vertical model boundaries. All of these surfaces are defined in the model by rigid, frictional boundary walls [Itasca, 1999; Benesh et al., 2007; Benesh, 2010]. Within these boundaries, we generate a mechanically-layered rock mass, and then drive deformation of the assemblage through displacement of the left-most, or hinterland, wall. We first describe the setup and parameters for standard experimental conditions, and then outline the variations from these conditions that we tested in subsequent experiments.

### 3.3.4 Boundary Conditions

We assign a wall/particle coefficient of sliding friction of 0.3 on the fault ramp and flat walls, and 0.57 on the vertical walls (the higher value is employed in order to

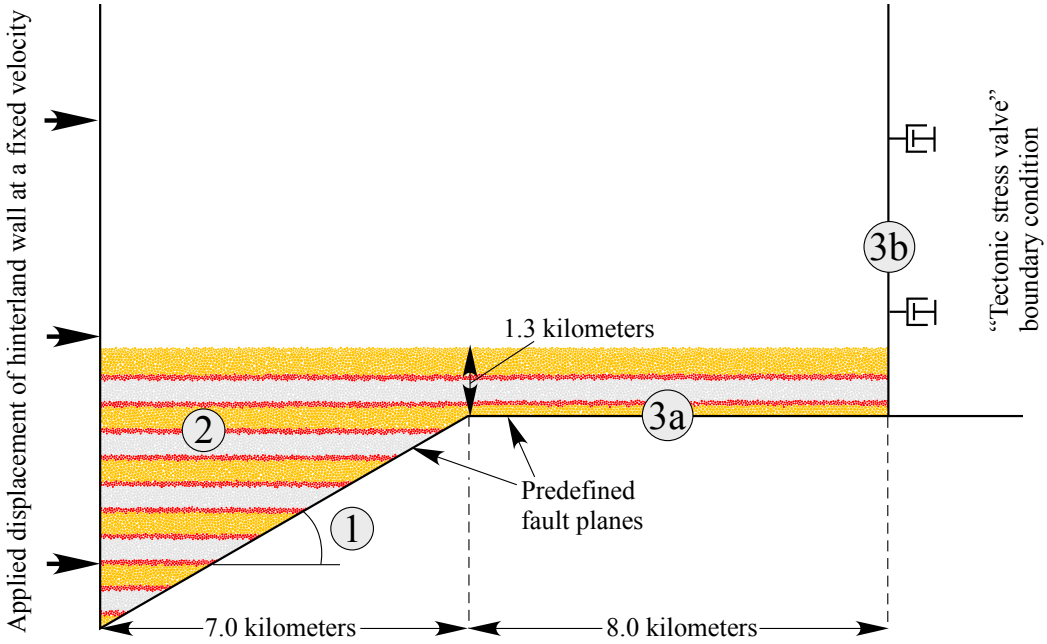


Figure 3.4: Initial model setup. Model parameters that are varied in this study include fault dip (1), properties of the rock layers, such as layer spacing, bulk material strength, and strength contrast between weak layers (red) and strong layers (orange and grey) (2), effective friction on the upper detachment (3a), restricted motion of the foreland wall (3b), and syn-tectonic sedimentation rate (not shown).

discourage vertical sliding of particles along these boundaries). During a given model run, the fault ramp and flat boundaries remain stationary, while deformation is driven by displacement of the hinterland wall of 1.5 kilometers at a rate of 3 m/s, which has been determined by previous work [Itasca, 1999; Benesh, 2010] as sufficiently slow that the resulting deformation is quasistatic. The foreland boundary is prescribed as a "tectonic stress valve;" its displacement is calculated such that deformation associated with the boundary is minimized. As the hinterland wall is displaced and deformation progresses, the foreland wall is displaced such that any tectonic stress is dissipated, but the horizontal stress associated with the adjacent rock material is maintained [Benesh, 2010].

### 3.3.5 Generation of pre-growth layers

Within these prescribed model boundaries, we generate a particle assemblage to simulate a sedimentary rock sequence (Figure 3.4). To generate a single rock layer, we create particles with the densities, frictional values, and size distributions described in section 2.2 in the space within the model boundaries, above any preexisting rock layers. These particles are then allowed to gravitationally settle to the bottom of the model. At each timestep, the force on each particle is calculated as the sum of the forces from all surrounding particles; an unbalanced force on the particle results in a net force that translates to a displacement of that particle. At the next time step, after all particles are displaced, the contact relationships with adjacent particles are updated, and the force balance process is iterated. This cycle is continued until the mean unbalanced force is a negligible fraction of the mean contact force, at which point the assemblage is considered to be "settled." Once the particles are settled, we remove all of the particles above a given datum; as this load is removed, the underlying particles rebound upward, so this process is repeated two more times to allow

for the layer to have a flat top surface. Each subsequent rock layer is generated by this process until the assemblage reaches 1.3 kilometers in height above the upper fault detachment. Strong layers, shown in orange and gray in the models, are 400 meters thick, and weak layers, shown in red, are 100 meters thick. After the material is assembled, the particles are assigned inter-particle shear and normal contact bonds as described in section 3.3.2.

### 3.3.6 Deformation procedure

Deformation of the particle assembly is implemented in PFC2D through an iterative time-stepping procedure. At a particular time step, all of the contacts on a single particle are summed to a net force on the particle, which is integrated to produce a finite displacement for the particle. This is done for all particles, and the new particle positions are used to calculate particle forces and contacts for the next time step (for a more detailed description of the numerical method, see Itasca [1999]). For quasistatic applications such as this one, this process iterates until the mean unbalanced force is a small fraction of the mean force for the particles. Additionally, a viscous damping term of 0.7 is applied to reduce the magnitude of the particle displacements in order to dissipate the energy in the system; it has been shown that the addition of such an artificial viscosity does not fundamentally alter the mechanics [Mora and Place, 1994].

### 3.3.7 Syntectonic sedimentation

After every 300 meters of shortening, the displacement of the hinterland wall is paused in order to allow for sedimentation of growth layers and the re-establishment of contact bonds in the assemblage. This is done in order to simulate the process of the re-development of cohesive strength through cementation, as this is an important process

in natural systems. Growth layers are composed of particles chosen from a uniform distribution of sizes from 18.5-24.75 meters, and are assigned the same frictional and contact bond properties of the standard material. The growth layers are deposited by the same method described for the pre-growth layers, in section 3.3.5. In order to minimize the effect of surface processes that may modify deformation patterns, we deposit sediment until the uplifted region adjacent to the hinterland wall is buried by 100 meters of sedimentation. Given that uplift rates vary across the structure, the ratio between the sedimentation rate on the uplifted area above the ramp and the foreland region above the upper detachment varies from 0.48 for a fault dip of 20° to 0.16 for a fault dip of 60°.

### 3.3.8 Model variations

In different experimental runs, we vary a number of geometric and mechanical parameters to investigate the relative contributions of these factors in determining folding style. These variants from the standard model parameters described in the previous section include:

1. the dip of the thrust fault ramp, from 20-60° at 5° intervals,
2. mechanical properties of the rock assemblage, including:
    a. the influence of a weaker bulk material strength,
    b. the absence of particle rebonding,
    c. 200 and 400 meter thick mechanical layer spacing,
    d. the magnitude of the relative strength between weak and strong rock layers
3. factors that affect the favorability of displacement along the upper detachment, including:

    a. effective friction on the detachment surface, which was accomplished by fixing the particles adjacent to the upper detachment to the boundary surface,

b. restricting movement of the foreland wall, and,

4. the rate of syn-deformational sedimentation, increased from 100 to 300 meters burial per 300 meters of shortening.

We run a model with standard conditions for each fault dip, resulting in 9 standard models with standard layer spacing, and 9 standard models with thin layer spacing. Then, for each of these 18 standard cases, we test the effect of weaker bulk material strength, no particle rebonding, increased strength of the weaker layers, increased sedimentation rate, increased effective friction on the upper detachment, and a stationary foreland wall, resulting in a total of 126 experimental runs.

## 3.4 RESULTS

For each of the model runs, we record the location of the particles every 100 meters of shortening. For the final deformation state, we analyze the deformational style of the resulting fault-related folding. Since one of the primary differences between fault-bend and fault-propagation folding is the presence or absence of translation of material along the upper detachment, we measure the displacement difference between the driving hinterland wall and the foreland wall. We report this value as the percentage of the tectonic shortening accommodated by internal deformation of the model (the remainder of the shortening is accommodated by displacement sent out the upper detachment). Additionally, we classify the resulting structures by the aspects of the fold limb and growth strata geometries that are characteristic of each of the deformational styles, which are color-coded throughout the reported results, as indicated below. The features of each of the fault-related folding classifications are subsequently described, and typical examples of each are shown in Figure 3.4.

**Fault-bend fold**–A structure is characterized as a fault-bend fold if it has an ac-

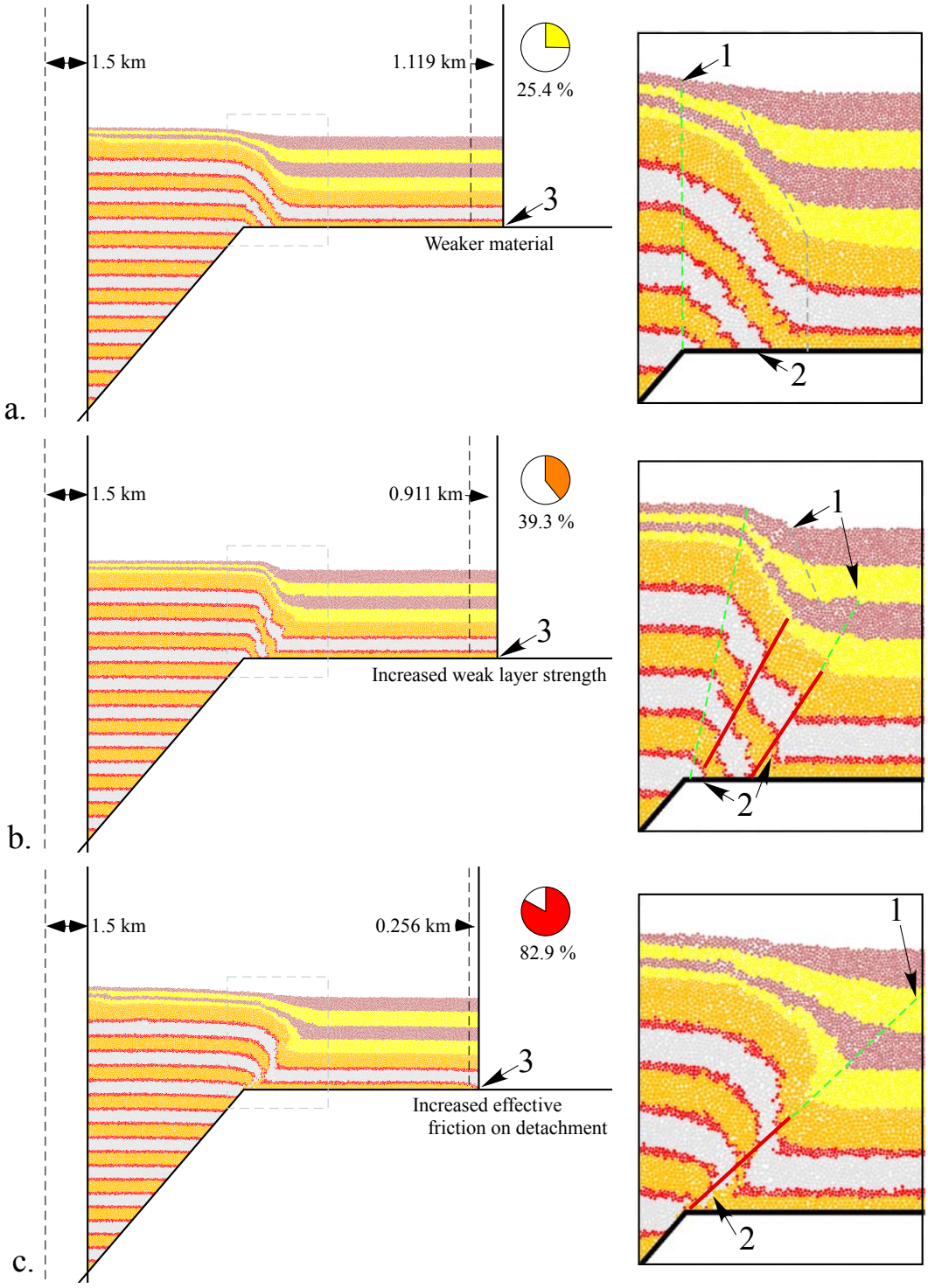


*(Continued on next page)*

Figure 3.5: (*Continued from previous page)*
Examples of different experimental results at 50° fault dip after 1.5 kilometers of shortening with thick layer spacing. Initial boundary wall locations are black dashed lines, final wall locations are black solid lines, and displacement on upper detachment is reported. Percentage of the shortening accommodated by internal deformation is reported in upper right, with pie chart colored to indicate deformational style, as described in section 3.4. (*a*) In the case of weak bulk material, fault-bend folding is observed (yellow), as discrete faulting and significant variations in layer thickness are not observed in the forelimb (1), an active anticlinal axial surface is observed (2, green dashed; inactive synclinal axial surface shown, gray dashed), and significant displacement along upper detachment is observed (3). (*b*) When the strength contrast between the strong and weak layers is decreased, transitional fault-related folding behavior is observed (orange), as discrete faults are observed in the forelimb (1, red dashed), active anticlinal and synclinal axial surfaces (green dashed) developed at different times in the growth of the structure, as indicated by the growth geometry (2), and an intermediate amount of displacement is translated along the upper detachment. (*c*) Increased effective friction along the upper detachment results in the development of a fault-propagation fold (red), in which a fault propagates upward from the defined fault ramp (red dashed, 1), an active synclinal axial surface develops (2), and most of the displacement is accommodated by internal deformation, with little displacement being translated along the upper detachment (3).

tive anticlinal axial surface, no abrupt changes in layer thickness in the forelimb, no localized faulting in forelimb, and significant displacement on the upper detachment. While kinematic models that preserve layer thickness do not exist for anticlinal fault-related folds with ramp dips higher than 30° that flatten to an upper detachment, we recognize that structures that fit the general criteria for a fault-bend fold may occur at these higher fault dips [Benesh, 2010].

**Fault-propagation fold**–these structures are characterized by an active synclinal axial surface, a discrete fault propagating upward from the defined fault ramp through the forelimb, and little displacement on the upper detachment. While these structures may be more specifically classified as consistent with one of the existing kinematic models for fault-propagation folding, we have limited our classification to the generalizations that are consistent among all models for fault-propagation folds.

**Transitional structure**–structures are characterized as transitional if they possess some, but not all, of the characteristics that are diagnostic of either a fault-bend or a fault-propagation fold. These structures may have minor, localized folding or faulting in forelimb, variable layer thinning and thickening, active synclinal and/or anticlinal axial surfaces, and some displacement on upper detachment. This includes structures in which a fault propagates through the forelimb, but is then abandoned and translated along the upper detachment, as well as structures that have an active synclinal axial surface, but no evidence for a fault propagating upwards over time from the predefined ramp; such a structure is characteristic of a fault-arrest fold.

**Other**–a very small number of the structures that develop in the experiments exhibit significant deformation outside of front-limb area associated with slip on weak layers toward the hinterland, resulting in distributed uplift and deformation.

Example model outcomes in which the deformation is characteristic of fault-bend-folding, transitional fault-related folding, and fault-propagation folding are shown in

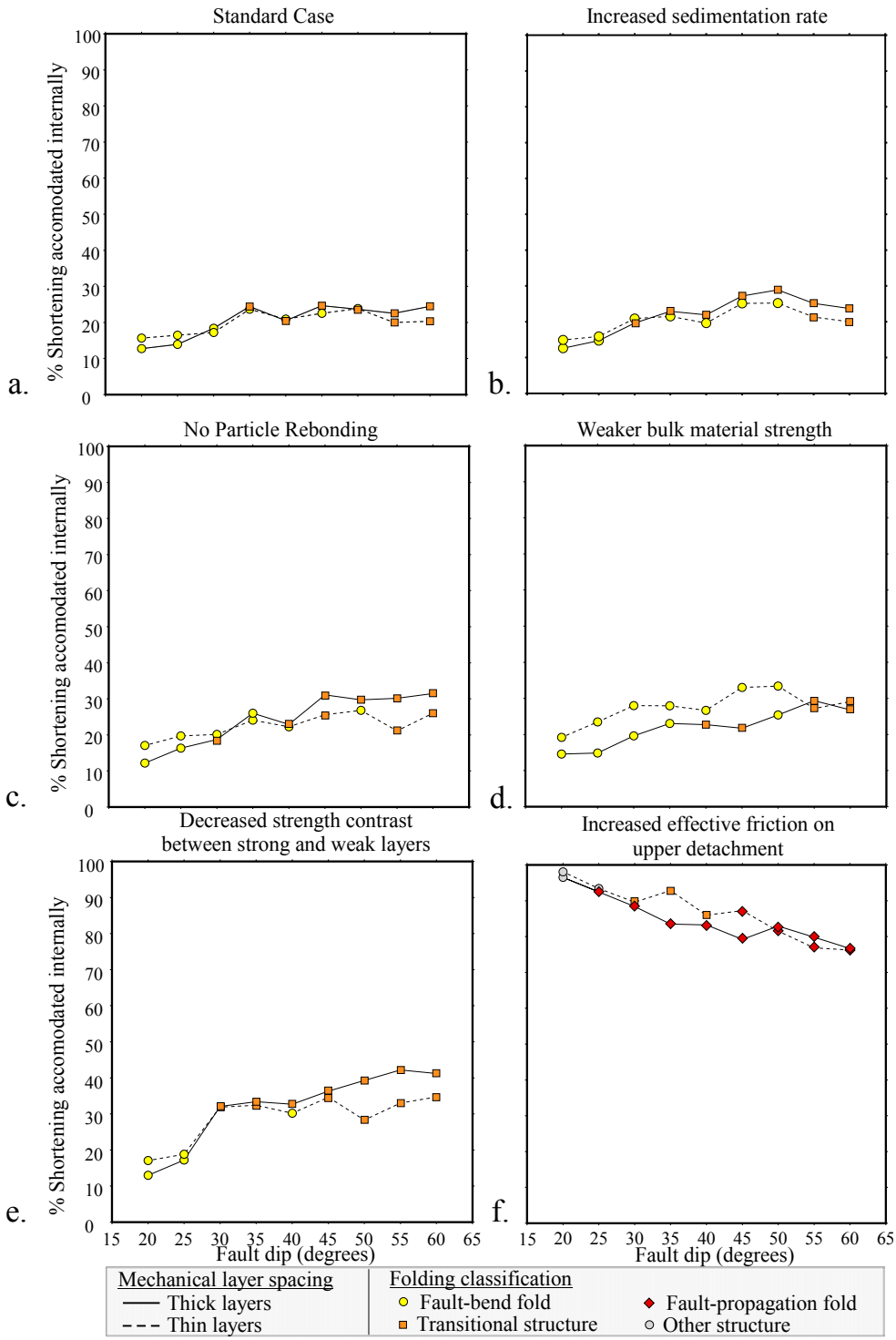


Figure 3.6: Percentage of displacement accommodated by internal deformation as a function of fault dip for the different experimental variants, color coded by observed fault-related folding style. Results for thick mechanical layer spacing (solid line) and thin layer spacing (dashed line) are plotted separately.

Figure 3.4. In each of these models, the fault dip, layer spacing, and sedimentation rate are constant, but other parameters are changed, which has led to the observable differences in deformation patterns. In the first case (a), the bulk material is weaker than the standard model, resulting in deformation that is characteristic of fault-bend folding. The resulting fold is characterized by relatively constant layer dip and thickness in the forelimb, and an anticlinal axial surface tied to the top of the ramp that remains active throughout the growth of the structure, as indicated by the geometry of the syntectonic strata. In the second case (b), the strength of the slipping layers is stronger than in the standard model, and the resulting deformation is transitional between fault-bend and fault-propagation folding. Discrete faults in the forelimb are observed, and the geometry of the syntectonic growth indicates that these faults are active for short periods of time, characteristic of fault-propagation folding. However, these structures are displaced away from the fault bend due to translation along the upper detachment, characteristic of fault-bend folding, and become inactive over time. In the final case (c), increased effective friction on the upper detachment has led to the development of a fault-propagation fold. A discrete fault can be observed emanating from the fault bend into the syncline of the structure, and a near-vertical, thinned forelimb is observed. Additionally, the geometry of the syntectonic strata indicates that the syncline is the locus of deformation for the duration of the structural growth. A fanning of dips in the growth strata also indicates a progressive rotation of the front limb over the duration of the fold growth, all of which are consistent with fault-propagation folding. The full suite of model outcomes, measurements, and classification information are available in the supplementary material, which can be found in Appendix A. The results for all model variations are summarized in Figure 3.6, where the percentage of the displacement accommodated by internal deformation of the model (rather than translation of material along the

upper detachment) is reported as a function of fault dip for thick (solid lines) and thin (dashed lines) mechanical layer spacing as a function of fault dip. The points are coded according to the fault-related folding style observed in the model, where yellow corresponds to fault-bend folds, orange to transitional structures, red to fault-propagation folds, and grey to other structures. These results may be summarized by the following general observations:

1. In the standard case, fault-bend folds form for all but the highest fault dips; very little difference is observed between thin and thick mechanical layer spacing, except that fault-bend folding is more readily accommodated at intermediate fault dips in the thinly-layered models;

2. In the case of no particle rebonding, slightly more of the deformation is accommodated by internal deformation at high fault dips, and this is correlated with the development of more transitional structures;

3. Weaker bulk material strength had little effect on the thick-layered model; in the case of thinly-layered weak material, more of the deformation is accommodated internally and fault-bend-folding behavior persists to higher fault dips than in the case of stronger material;

4. Increased sedimentation rate over the range that we have considered has a negligible effect on fault-related folding style and shortening, relative to the standard case;

5. A decreased strength contrast between the strong and weak layers results in more of the shortening being accommodated by internal deformation and the development of more transitional structures;

6. Increased effective friction on the upper detachment resulted in nearly all of the displacement being accommodated by internal deformation of the material, and the associated development of fault-propagation folds in all but the lowest fault dips for

thick-layered experiments, while for thinly-layered models, some transitional behavior was observed at low to intermediate fault dips, and fault-propagation folds developed at high fault dips.

The model results can be categorized into factors that have a significant impact on structural style, and factors that have a minor effect. We find that the frictional properties of the upper detachment and the mobility of the foreland wall exert the strongest influence on structural style. Fault dip, mechanical layer spacing, and relative mechanical layer strength all have an important, but secondary, influence. Finally, overall material strength, the presence or absence of particle rebonding, and sedimentation rate have negligible effects on structural style. These observations are elaborated on and explained through further analysis in the subsequent discussion.

## 3.5 Discussion

Whether a fault-bend or fault-propagation fold forms associated with a thrust ramp is dependent on a range of mechanical and geometric factors. As the displacement of material along an upper detachment is one of the most diagnostic differences between the two styles, the ultimate style of structure that develops given a set of model parameters may be thought of as the relative balance between the forces opposing translation along the detachment and the forces promoting translation along the detachment. Particular mechanical and geometric conditions lead to specific patterns of stress and strain in the model that make translation along the detachment more or less favorable. Thus, an analysis of how the distribution of strain changes throughout deformation for each of the model variants described in the previous section helps us to identify where significant strain accumulates in the model, and how this may impact the ability of the layers to transmit stresses and displacement into the foreland, thus

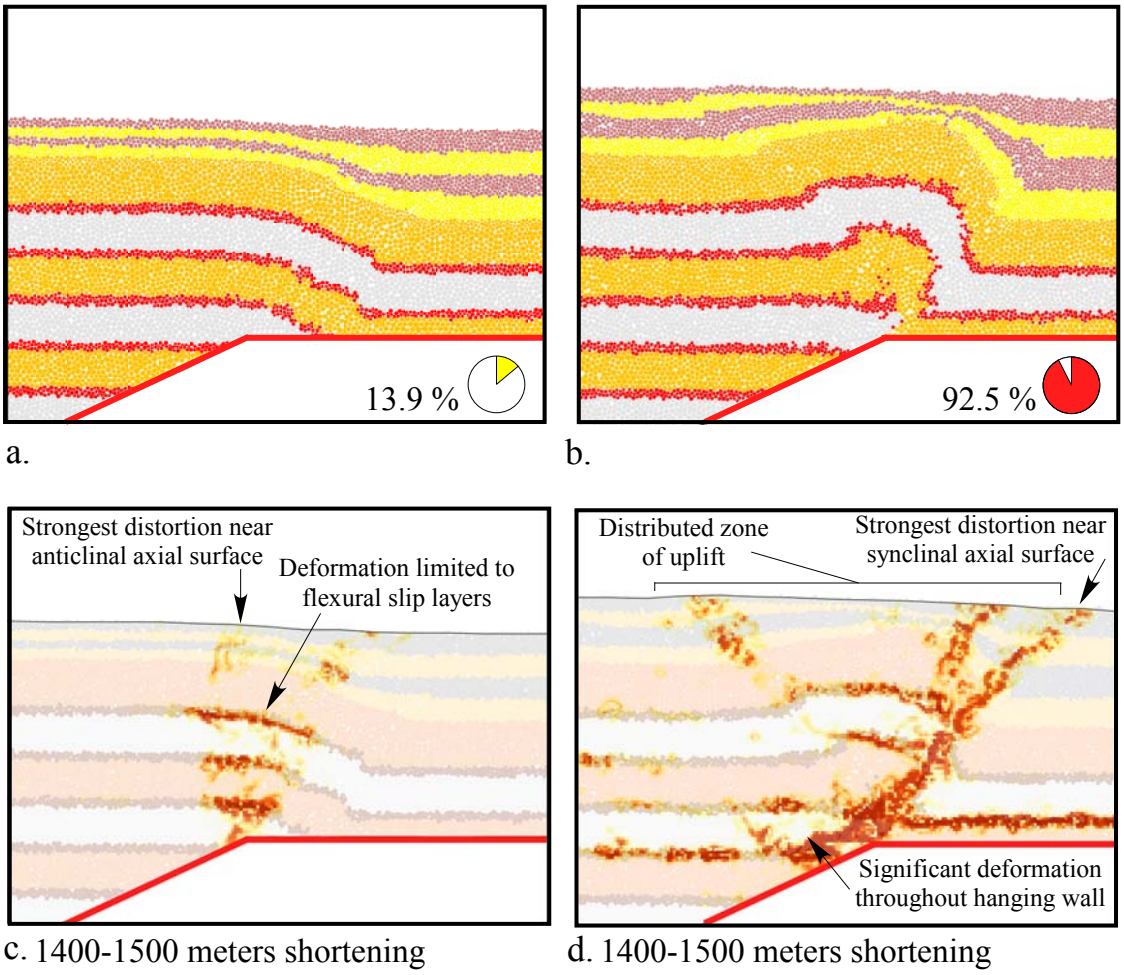


Figure 3.7: Final model geometry for a fault dip of 30°, (*a*) standard case, and (*b*) increased effective friction on detachment, with percentage of shortening accommodated internally inset, bottom right. (*c*) Overlay of J2 distortion for the final 100 meters of shortening for model (*a*), showing that the folding is mostly accommodated by a zone near the anticlinal axial surface of flexural slip on the weak layers, resulting in the development of a fault-bend fold. Red indicates high values of distortion. (*d*) Overlay of J2 distortion for the final 100 meters of shortening for model (*b*), showing higher overall distortion, strong distortion along the structure's synclinal axial surface, and distributed uplift accommodated by diffuse deformation throughout weak layers in the crest of the structure. Deformation on the first weak layer along the upper detachment serves as a detachment that accommodates a modest amount of slip (7.5% for the entire model run).

controlling structural style. In order to visualize the incremental strain and localized deformation mechanisms active throughout the development of a given structure, we focus on the spatial variations of distortional strain [Morgan and Boettcher, 1999; Morgan, 1999]. Displacement vectors are calculated from the particle locations that were recorded every 100 meters of shortening, and from this, the displacement gradient tensor is determined using a gridding approach. Finally, the second invariant of the deviatoric strain tensor (J2), also referred to as the "equivalent strain," is calculated, which is an effective means of visualizing the distortion occurring in localized regions of the model [Hill, 1967, p. 14-21]. By identifying the spatial and temporal distribution of strain during model deformation, we can evaluate the role of different deformation mechanisms, such as flexural slip and localized shear, in contributing to the observed structural geometries.

### 3.5.1 Influence of fault friction

We first examine the deformation mechanisms observed at low fault dips between the standard model conditions (Figures 3.7a, c). In this case, the geometry of the model is consistent with fault-bend folding, and very little of the shortening is consumed by internal deformation of the model (13.9 %). The distribution of distortional strain illustrates that the vast majority of the deformation is confined to the weak layers in the region of the anticlinal axial surface, as was shown by Benesh [2010]. This is consistent with the assumption of the kinematic fault-bend folding model, in which layer-parallel shear accommodates folding through the flexural slip process [Suppe, 1983]. We may infer from this strain pattern that the thin layers accommodate the majority of the strain, leaving the thicker, more competent layers modestly deformed. As a result, these layers retain a significant portion of their strength, and thus are able to transmit stresses and deformation out into the foreland, which facilitates slip on

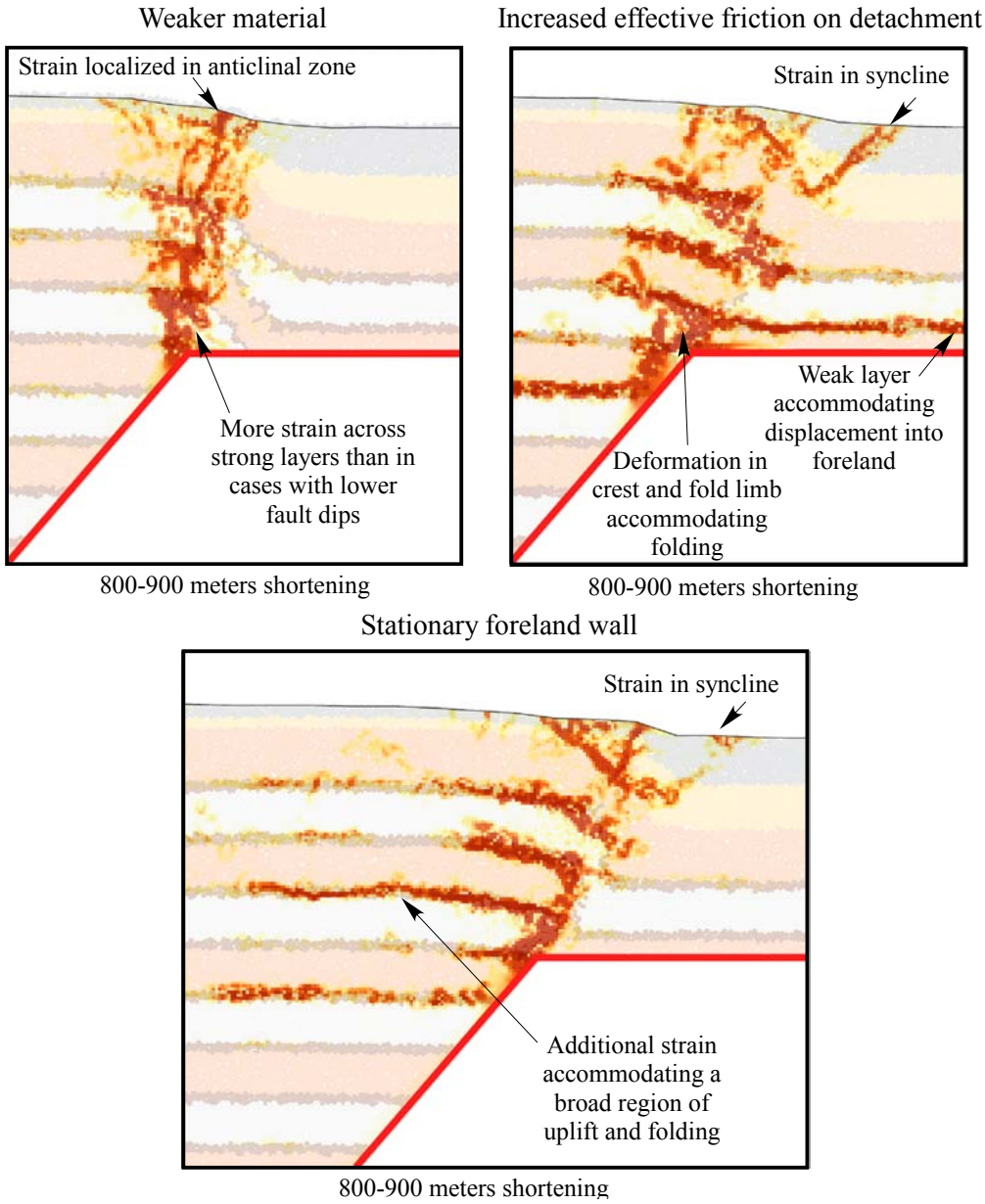


Figure 3.8: Model geometries overlain by plots of J2 distortion for 50° fault dip models, for the model in figure 3.4*a* (a), 3.4*c* (*b*), and a stationary foreland wall (*c*). (*a*) For weak bulk material strength, while a fault-bend fold still develops, the folding is accommodated by much stronger axial-surface-parallel shear in the anticlinal axial zone than at lower fault dips. (*b*) Increased effective friction on the detachment results in shear in the structural syncline and distributed deformation along weak layers in the crest, accommodating folding and uplift in the development of a fault-propagation fold. (*c*) A similar structure develops when the foreland boundary is held stationary, but the additional shortening is accommodated by distributed shear in weak layers in the structural crest, resulting in the development of more uplift and folding.

the detachment and the fault-bend folding process. This may be readily contrasted with the deformation observed in the case of increased friction on the upper detachment (with all other model conditions the same as in the previous case). The model geometry shows the development of a highly asymmetric fold, with a broad, gently dipping backlimb, and a steep, thinned forelimb that is cut by a small fault emanating from the thrust ramp through the structural syncline. Analysis of the growth geometry indicates that the syncline was active over the duration of structural growth. Additionally, nearly all (92.5%) of the shortening in this model was accommodated by internal deformation. This is supported by the observation that overall distortion values are much higher in this model. Additionally, the J2 distortion highlights a zone of strong shear in the structural syncline, and distributed shear over a wide region, accommodating folding and uplift. These observations of an active syncline pinned to the fault tip and an additional component of folding and uplift in the structural crest are characteristic of fault-propagation folding [Hardy and Poblet, 2005]. These findings are consistent with previous analytical mechanical models in which ramp-to-flat fault geometries with very low friction produce symmetric fault-bend folds, while increasing fault friction resulted in the accommodation of higher amounts of shortening by internal model strain and the development of asymmetric structures [Wiltschko, 1979a,b; Berger and Johnson, 1980]. Variable mesoscale deformation above an upper detachment has been observed in the hanging wall of the Lewis Thrust, and based on analytic elastic modeling, was determined to have been related to the spatial variation in mean stress along the detachment due to variable shear strength and displacement along the detachment [Erickson and Wiltschko, 1991], also highlighting the role of detachment strength in overall structural style.

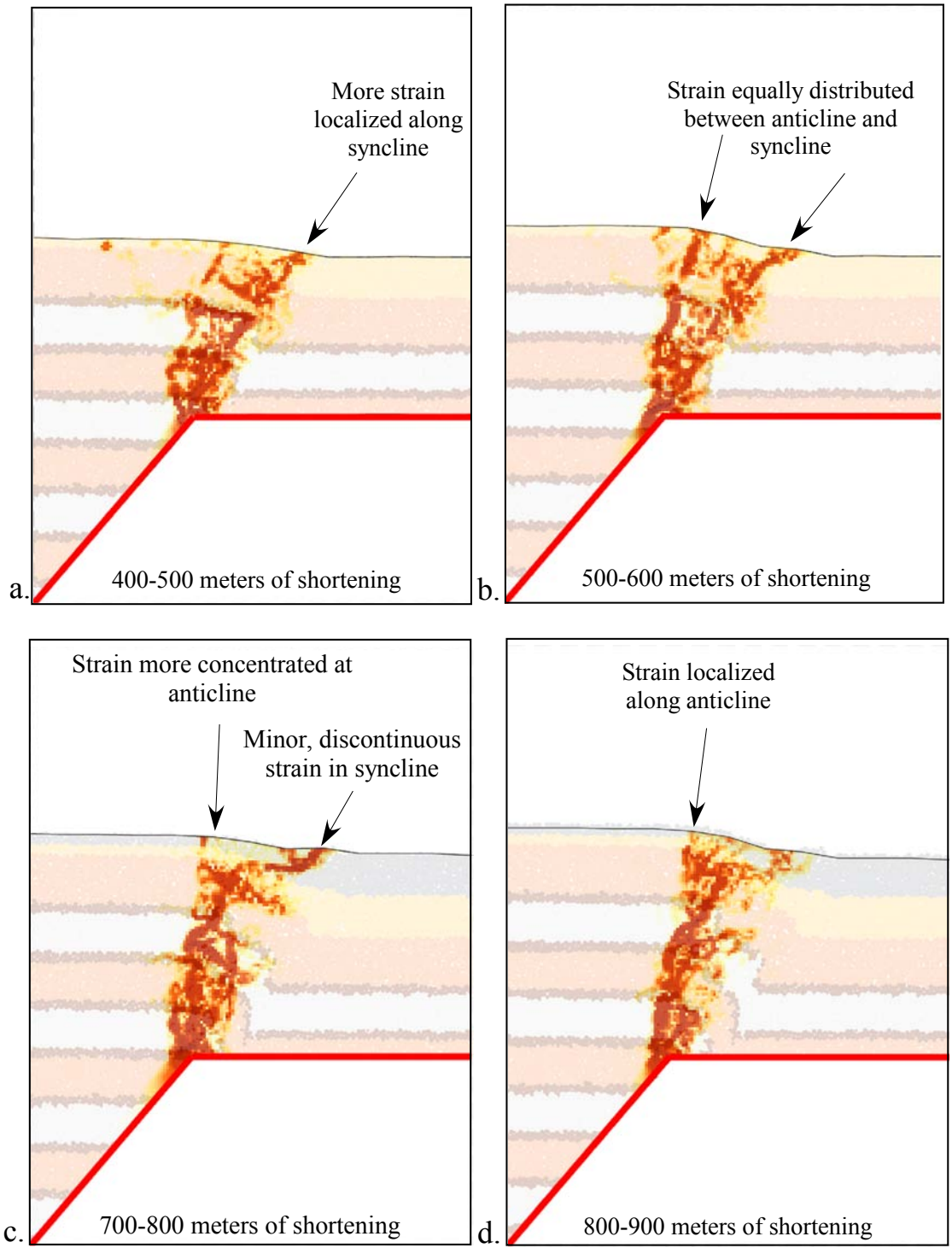


Figure 3.9: J2 distortional plot for the structure shown in Figure 3.4b, which displays mixed signatures of fault-bend and fault-propagation folding, at 400-500 meters shortening ($a$), 500-600 meters ($b$), 700-800 ($c$), and 800-900 ($d$), showing that the location of maximum distortion switches locations from the structural syncline to the anticline over time.

### 3.5.2 Influence of fault dip

For nearly all model variants, the amount of shortening accommodated by internal deformation is lower at low fault dips, and higher at high fault dips; this is accompanied by a transition from predominantly fault-bend folding to more transitional behavior. Plots of distortion for the models in Figures 3.4a and c are shown in Figures 3.8 a and b; these are otherwise the same as the models discussed in section 3.5.1(only fault dip is varied). For the case of weaker material strength, a structure characterized as a fault-bend fold develops. Distortion is concentrated in the anticlinal axial zone, but rather than localized to flexural slip surfaces, the folding is accommodated by shear across layers; the location of this shear remains fixed to the anticline over time, yielding a forelimb that has been penetratively sheared and weakened as it is displaced past the axial zone. As a result, the progressive weakening of the forelimb as deformation progresses makes it less capable of transmitting stress and displacement into the foreland along the detachment, and a greater proportion (25.4%) of the shortening is accommodated by internal deformation. This effect is modestly augmented when particles are not periodically rebonded (29.7% of the deformation accommodated internally), as this promotes more persistent strain localization. Therefore, higher fault dips limit the capacity for flexural slip to accommodate folding, leading to the development of more localized shear, which subsequently results in forelimb weakening, more deformation accommodated internally, and the development of more transitional structural styles. The relative importance of these two deformation mechanisms in accommodating fault-bend folding has been the focus of previous mechanical modeling work by Erickson et al. [2001] and Benesh [2010]. These studies found that while factors such as sedimentation rate, angularity of fault bends, and relative mechanical layer strength drove the dominance of layer-parallel or layer-perpendicular shear,

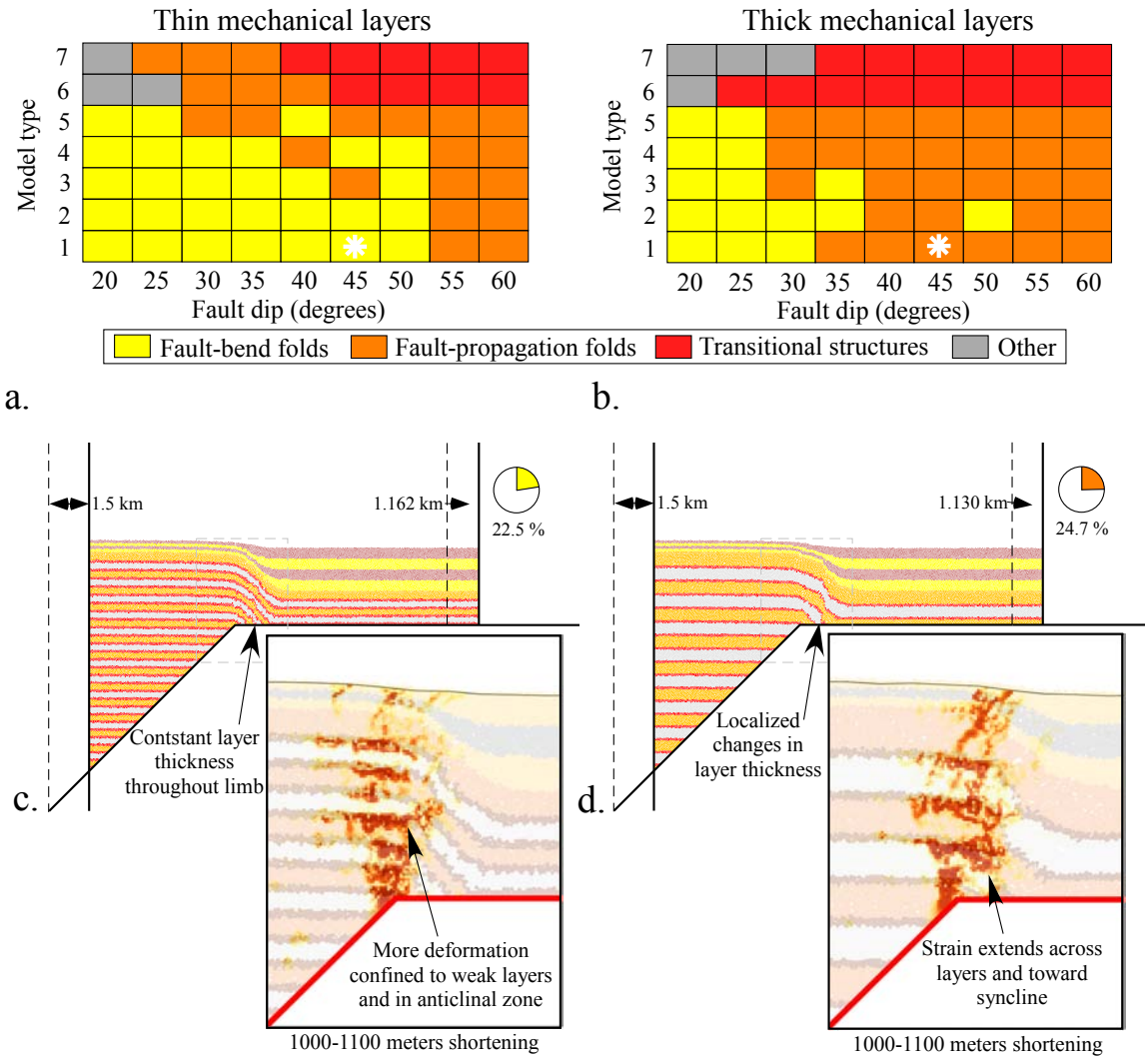


Figure 3.10: (*a* and *b*) Classification of resultant structural styles as a function of fault dip and model type for thin and thick mechanical layer spacing, respectively, where model types are as follows: 1–standard case; 2–weaker bulk material strength; 3–no rebonding; 4–increased sedimentation rate; 5–decreased layer strength contrast; 6–increased effective friction on detachment; 7–stationary foreland wall. (*c*) 50° fault dip model, standard case, thin layer spacing, with overlay of J2 distortion highlighting strain in weak layers (inset), (*d*) 50° fault dip model, standard case, thick layer spacing, with J2 distortion highlighting strain in weak layers and an additional component of strain breaking across strong layers, and more strain toward the syncline of the structure. The locations of the models in *c* and *d* are indicated by a white asterisk in *a* and *b*.

both cases resulted in the formation of fault-bend folds.

### 3.5.3 Influence of boundary conditions

To further explore how the availability of an upper detachment influences folding style, we examined a set of models with a fixed foreland wall. This situation is considered representative of natural cases in which a detachment layer may be folded or faulted by a second, foreland structure and can no longer accommodate slip due to geometric limitations. Alternatively, this may represent cases where a detachment is localized in a weak stratigraphic unit (e.g., salt) that pinches out in the foreland. As suggested in analog modeling studies [Chester et al., 1991], boundary conditions play an important role in the determination of structural style. The influence of a stationary foreland wall was tested (with otherwise standard model parameters). For the same fault dip as the models in section 3.5.2, the resulting fold geometry and distortion are shown in Figure 3.8c. The resulting fold geometry is very similar to the structure that resulted from increased effective friction on the upper detachment. The models share evidence for an active synclinal axial surface and distributed folding and uplift in the crest of the fold, characteristic of fault-propagation folding. This suggests that both increased fault friction and foreland boundary conditions are viable mechanisms for promoting the development of fault-propagation folds. The distribution of distortion shows that the additional internal deformation that occurs within the stationary wall model was accommodated by flexural slip and thickening of weak layers in the development of folding and uplift of the crest of the structure over a broader region. The models exhibit a range of fault-propagation folding geometries: the flexural slip and additional component of uplift observed in some of the mechanical models are more consistent with the implied deformation mechanisms of the fixed-axis and constant-thickness fault-propagation folding styles [Suppe and Medwedeff, 1990], while the distributed shear throughout the frontlimb region and limited additional uplift ob-

served in others is more consistent with the trishear kinematic model [Erslev, 1991; Allmendinger, 1998], and others exhibit a combination of both deformation mechanisms that would be consistent with a hybrid fault-propagation folding style between these end-members.

### 3.5.4 Influence of relative mechanical layer strength

The influence of the relative layer strength between weak and strong layers may be observed by contrasting the standard model, which has a high degree of strength anisotropy, with a model where the ratio of layer strengths is decreased (Figure 3.4b), but which shares all other model properties. Plots of distortion show that flexural slip is significantly inhibited, and that the folding is primarily accommodated by localized shear. This suite of models accommodates significantly more shortening by internal deformation, and exhibits a significantly more transitional structural style than standard models (Figure 3.6e), which is consistent with progressive strain weakening of the forelimb over time as a result of this deformation mechanism. A close examination of the distribution of distortion in a representative model throughout its history (Figure 3.9a-d) shows that at different time periods, strain is primarily localized in the structural syncline (characteristic of fault-propagation folding), in the structural anticline (characteristic of fault-bend folding), in both, or distributed throughout the limb. This suggests that the structural style of transitional structures changes throughout model deformation. Thus, rather than being a distinct folding mechanism, these transitional structures result from an integration of fault-bend and fault-propagation folding mechanisms. The importance of mechanical anisotropy is consistent with previous mechanical modeling studies that found that models with high layer strength contrasts favor the development of folding, while isotropic or weakly layered models showed a preference for faulting [Erickson, 1996; Goff et al.,

1996; Benesh, 2010]. The observation that relative mechanical layer strength is important in determining structural style, and that a structure may exhibit mixed structural style or may change structural style over time is also consistent with previous field studies. Field-based studies of foreland fold-and-thrust belts have recognized a spatial correlation of along-strike facies changes with variations in structural style in the Appalachians [Julian and Wiltschko, 1983; Woodward et al., 1988], Canadian Rockies [Spratt et al., 2004], Caledonides [Morley, 1986], and Sierra Madre Oriental [Fischer and Jackson, 1999], which suggests that the mechanical properties of stratigraphic layering extert a significant influence on structural style. Woodward and Rutherford Jr [1989] observed that changes in structural style along strike in a variety of fold-and-thrust belts are strongly correlated with composition and stacking sequence of sedimentary layers, suggesting that layer anisotropy and strength is the greatest determinant in folding geometries. They also speculate that, as these properties vary continuously, a continuum of fault and fold angularity and fault-related folding style results. Furthermore, through detailed analysis of mesoscale structural deformation mechanisms in different stratigraphic layers in a detachment fold in the Sierra Madre Oriental, Fischer and Jackson [1999] were able to infer that flexural slip and flexural flow, or shear parallel to bedding planes and axial surfaces, respectively, were active sequentially and coevally during the development of map-scale fault-related folds. These variations were closely tied to stratigraphy. These inferences, based on field-based observations, are borne out by our mechanical modeling results.

### 3.5.5 Influence of mechanical layer spacing

A plot of the structural style that results in all model variants as a function of fault dip shows that fault-bend folding persists to higher fault dips in models with more closely-spaced mechanical layers (Figure 3.10a), while the same conditions in models

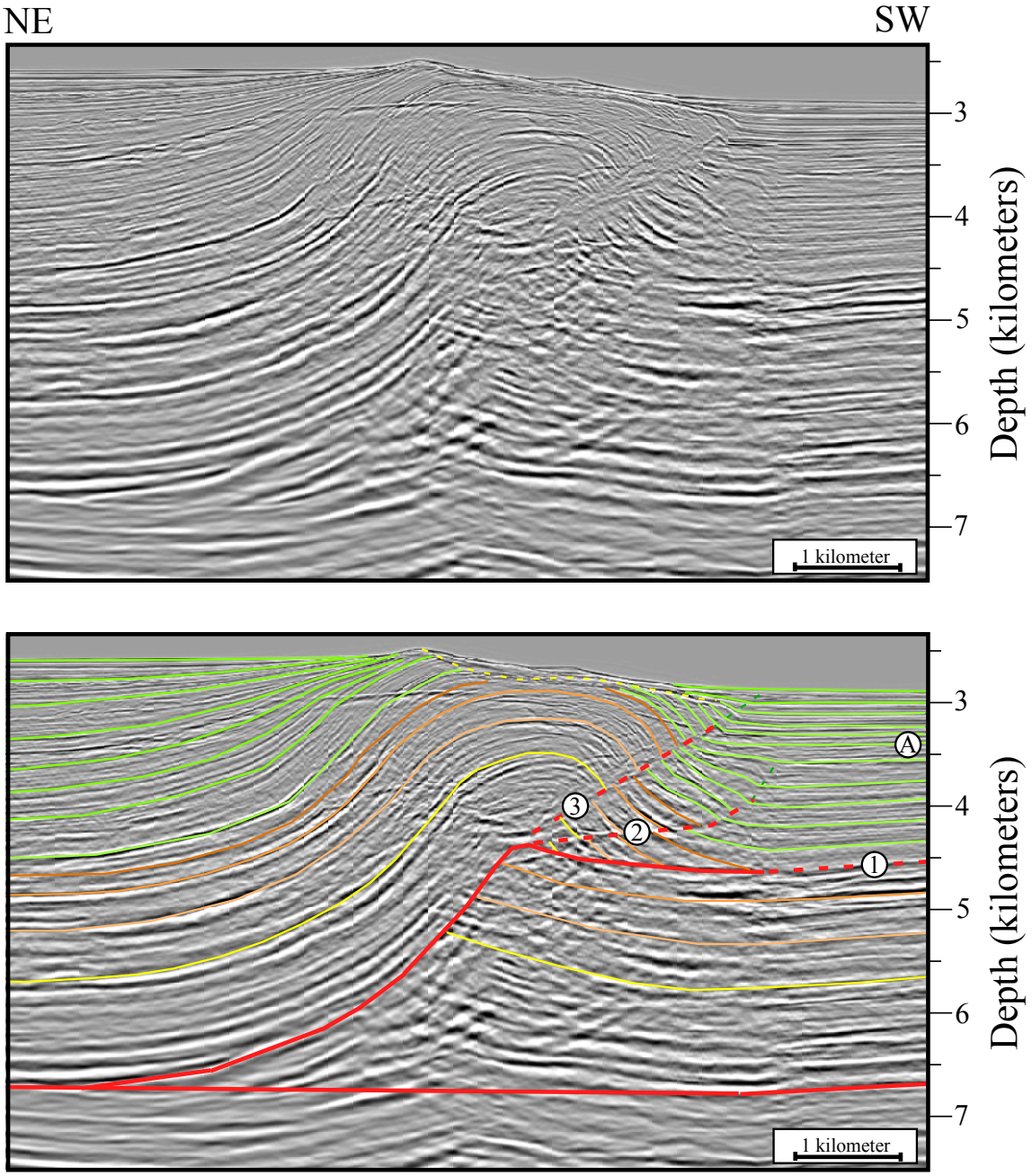


Figure 3.11: (*a*) Seismic reflection profile of a fault-related fold in the northwestern Niger Delta that displays evidence of fault-bend and fault-propagation folding. (*b*) Enlargement of the forelimb region of the structure (grey box in (*a*), with interpretation. Note pregrowth stratigraphic layers (orange and yellow), growth layers (green), faults (red), original detachment (1), first fault break-through (2), highest growth layer deformed by fault 2 (A), and most recent fault break-through (3). Data is owned and provided courtesy of CGGVeritas, Crawley, UK.

with more widely-spaced mechanical layers tend to develop transitional structures (Figure 3.10b). The impact of this difference is highlighted by the standard model conditions at a fault dip of 45 °, in which a fault bend fold develops in the thinly-layered case, but transitional fault-related folding behavior is observed in the thickly layered case. Relatively constant forelimb dip and layer thickness is observed in the fault-bend fold, associated with strain localization in the weak layers along the anticlinal axial surface. In the latter case, significant deviations in layer thickness occur in the middle of the forelimb, which is associated with distortion both within weak layers and across-layer shear, and more deformation toward the middle of the limb. The persistence of fault-bend folding to higher fault dips in thinly-layered models indicates that the presence of these weak layers allows for more of the deformation to be accommodated by folding through flexural slip.

### 3.5.6 Model variants that have little influence on fault-related folding style

We find that fault-related folding style is relatively insensitive to overall bulk material strength; this is supported by the observation that fault-related folding models are successfully applied to regions with highly variable overall material strength, such as subaerial fold and thrust belts faulting strong, well-lithified rock, and weaker materials found in accretionary prisms and passive margins. Additionally, while it might be surmised that the absence of rebonding (a simulation of the process of reestablishing material strength through cementation of faulted material over time) could serve to have a strong strain weakening effect and serve to localize deformation over time, the observed overall effect on the resulting structural style was modest. Finally, we tested the influence of sedimentation rate, as some previous analog and mechanical modeling studies have suggested that it may play in important role in structural style

[Barrier et al., 2002; Strayer et al., 2004]. However, we find in the range of model parameters we have chosen for our study, sedimentation rate has a negligible effect on the structural style that develops. This likely occurs because our models have significant layer strength anisotropy and sufficiently high sedimentation rates that the impact of surficial modification on structural geometry is minimized. Natural cases in which sedimentation rates are lower would be expected to exhibit variations in deformational patterns associated with surficial processes and the strong differential sedimentation between the structural crest and trough.

## 3.6 Comparison with natural structures

### 3.6.1 Regional geologic setting of the Niger Delta

The structures analyzed in this study are imaged in an extensive industry two-dimensional seismic-reflection dataset from the deepwater offshore Niger Delta. This region is ideal for comparison with our model results because, unlike most subaerial fold-and-thrust belts, many structures in the deep water Niger Delta have significant syntectonic sediment deposition. These sediments preserve a record of how these structures deformed over time [Suppe et al., 1992; Storti and Poblet, 1997]. Additionally, the data quality is exceptional, allowing for the detailed study of structural geometry. Situated offshore of Nigeria in the Gulf of Guinea, the Niger Delta is a gravity-driven linked extensional/contractional passive margin system that overlies the attenuated transition between African continental crust and Early Cretaceous-aged oceanic crust. Delta formation began as sediments from the Niger River accumulated in the Benue Trough during the opening of the Atlantic Ocean, with delta progradation beyond the continental shelf occurring by the Late-Eocene [Damuth, 1994; Doust and Omatsola, 1990]. Gravity-driven collapse of the sediments deposited

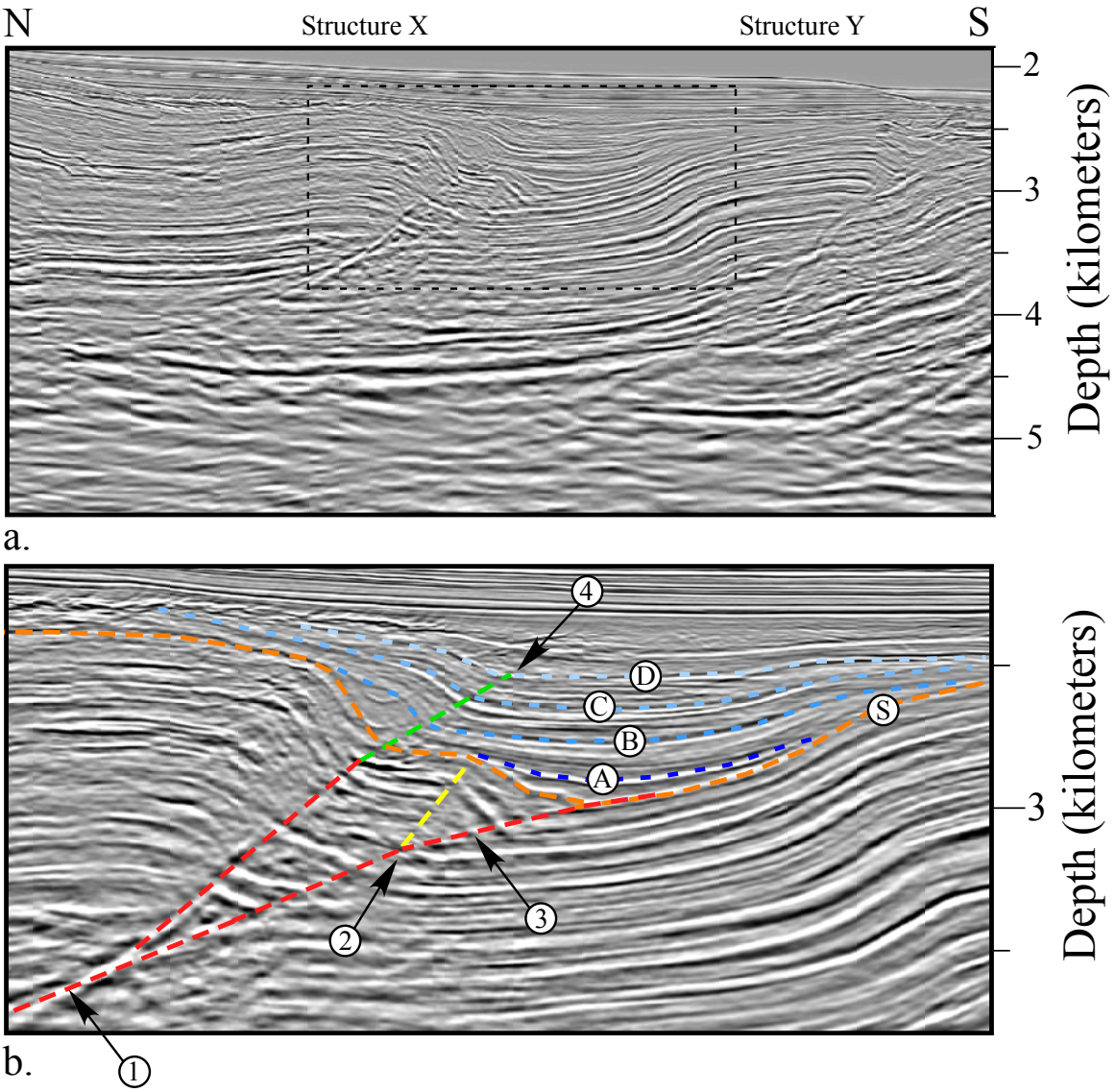


Figure 3.12: (*a*) Seismic reflection profile of a series of thrust faults in the northwestern Niger Delta. (*b*) Enlargement of the forelimb structure in (*a*), with interpretations (dashed lines) and the following features noted: thrust ramp indicated by fault plane reflector (1), angular cutoffs indicating fault location (2), anticlinal axial surface tied to minor fault bend (3), synclinal axial surface (4), top of pre-growth layers (S), growth layers (A-D). Data is owned and provided courtesy of CGGVeritas, Crawley, UK.

in the Niger River delta results in active extension, accommodated by normal faulting, in the onshore parts of the delta [Wu and Bally, 2000]. This extensional displacement is linked through a detachment system in a weak, overpressured shale unit to contractional fold-and-thrust belt deformation in deep water, which began by the Late Miocene to Early Pliocene. This deformation consists of a highly imbricated inner fold and thrust belt, a detachment-folding belt, and an outer fold-and-thrust belt [Connors et al., 1998; Corredor et al., 2005a; Bilotti and Shaw, 2005]. Regionally, the detachment occurs in the Akata formation, an early to mid- Tertiary-age time-transgressive thick marine shale [Avbovbo, 1978]. This formation is characterized low seismic velocities, reflective of fluid overpressures [Bilotti and Shaw, 2005] that developed due to rapid burial and hydrocarbon maturation. This unit is overlain by the Agbada formation, an Eocene to recent section of mixed pelagic-sourced shales and turbidic sequences of stacked channel complexes and basin floor fans [Briggs et al., 2006].

### 3.6.2 Transitional fault-related folds

A large number of studies have focused on documenting the kinematics of natural examples of end-member fault-bend [e.g., Suppe, 1983; Rowan and Linares, 2009; Shaw et al., 2005; Yue et al., 2005; Hubert-Ferrari et al., 2007] and fault-propagation folds [e.g., Erslev, 1991; Zapata and Allmendinger, 1996; Erslev and Mayborn, 1997; Cardozo et al., 2005; Shaw et al., 2005; Masini et al., 2010], yet characterization of structures that are transitional between the two styles is limited. As such, we have chosen to focus on two structures for which a transition between structural styles may be clearly inferred from the structural and growth geometries; we then relate the transitional nature of these structures to mechanical and geometric factors that likely contributed, based on our model results.

The forelimbs of many structures in the Niger Delta are suggestive of transitional fault-related folding, and often, reactivation of an existing thrust after some period of sediment deposition. The multistage deformational history of these structures suggests periodic reactivation of structures that is indicative of sustained internal deformation of the fold-and-thrust belt (as opposed to a simple break-forward sequence). This sustained activity may be associated with maintaining critical taper [Bilotti and Shaw, 2005]. In the analytical critical taper model, a wedge must deform internally to maintain taper as it propagates forward and incorporates more material into the wedge, or to respond to erosion or a strengthening of the basal detachment [Davis et al., 1983; Dahlen et al., 1984, and others]. Such coeval fault activity on thrusts in a wedge has been observed in analog models [Wu and McClay, 2011] and fold-and-thrust belts [Shaw et al., 1999; Corredor et al., 2005a].

In the first example, we examine a fault-related fold from the western portion of the outer fold-and-thrust belt. The structure has at least 2.5 kilometers of slip, with a front-limb that shows evidence of distinct periods of fault-bend and fault-propagation folding during its history (Figure 3.11). The thrust ramp steps up from a detachment at 6.5-7.0 kilometers depth. Angular cutoffs of seismic reflectors in the hangingwall and foot wall define a steepening upward fault ramp to 4.5 kilometers. At this depth, the fault flattens to an upper detachment (1) at the top of the pre-growth layers, which was the sea floor at the time of deformation. The location of this detachment is constrained as the point at which deeper seismic reflectors are flat, while overlying (hanging-wall) reflectors are inclined and terminate abruptly into the surface. These observations indicate that the structure initiated as a fault-bend fold. A fault is observed breaking through the front limb at point (2). This fault is associated with folded growth layers in advance of the fault tip in the structural syncline, which is characteristic of fault-propagation folding. However, this structure has been

translated away from the fault bend, presumably the result of displacement along the detachment, characteristic of fault-bend folding. Layer A is not folded above fault bend at location (2), and thus, this fault was inactive since the deposition of that layer. Finally, another fault propagated through the forelimb (3), which folds Unit A and other shallow growth layers in the structural syncline, consistent with fault-propagation folding. Through these observations, we would classify this structure as transitional.

Two aspects of our mechanical modeling results suggest reasons that this structure experienced transitional fault-related folding styles. First, the stratigraphy of the Niger Delta is relatively homogeneous, so strong mechanical layer heterogeneity is not likely present. Additionally, the thrust ramp dip (approaching 50° at the top of the ramp) is high. As transitional structures were observed most commonly at high thrust ramp dips and in models with low mechanical layer strength contrast (compare with the model results from Figures 3.4b and 3.9), these factors likely contribute to the observed transitional nature of this structure. Additionally, as the sea floor acted as an upper detachment, the subsequent deposition of sediment on that surface also served to increase the effective friction on that interface.

A second structure from the southern portion of the outer fold-and-thrust belt exhibits a similar transition in structural style. However, observations from the seismic reflection data suggest that while the structures both deform relatively isotropic material, which favors transitional behavior, an additional factor contributes to the change in folding style that occurred over time in this structure (Figure 3.12). A fault ramp, highlighted by a prominent reflector (1), can be observed extending upward at an angle of 22° beneath structure X. The fault, as defined by an angular cutoff between dipping layers above and flat layers below, shallows across a bend of 7° (2). An anticlinal fold is observed above this bend (3). The anticlinal fold associated with

the fault bend is consistent with this structure having initiated as a fault-bend fold that detached on the paleo-seafloor, where layer S is the highest pre-growth stratigraphic layer. That stratigraphic layer A truncates onto this forelimb of structure X indicates that it was deposited during or after this fold developed. This layer also truncates onto the backlimb of the foreland structure (Y). The anticlinal axial surface associated with this fault-bend fold does not extend upward into overlying layers B and C, indicating that these units were deposited after folding ceased. However, these layers are truncated and folded by the deformation associated with structure Y in the foreland, indicating that this structure remained active after fault-bend folding (and hence slip on the upper detachment) ceased. Finally, another fault is observed breaking upwards from the fault ramp in structure X at a dip of 40°. This fault splay is associated with a steep forelimb and an active synclinal axial surface pinned to the tip of the fault (4) that folds layers B,C, and D.

Based on these observations, we interpret the following order of events. Fault-bend folding occurred with an upper detachment on the paleo-seafloor in structure X. As sediments filled the accommodation space to the foreland of the forelimb and structure Y began to develop in front of this structure, the detachment became covered with sediment and folded. Finally, a fault broke upwards from the hinterland ramp and formed a fault-propagation fold. This fault-propagation fold was active contemporaneously with the structure to the foreland. This sequence of events suggests that the deposition of sediment and folding of the detachment by the foreland structure served to make displacement along the detachment no longer favorable.. Thus, structure X transitioned from a fault-bend to a fault-propagation fold.

This transition in folding behavior implies that slip on the upper detachment became less favorable. This is despite the fact that the rotation of the detachment by the foreland structure Y places it in a more favorable orientation for slip based on

Mohr-Coulomb considerations. This indicates that factors other than simple Mohr-Coulomb criteria played a role in making this detachment less favorable for slip. We suggest that the folded geometry of the detachment would require the overlying sediments to be folded for displacement along the detachment to continue. Evidently, the energy needed to fold the overlying sediments had a stronger effect than the more favorable fault orientation, leading to the abandonment of the upper detachment surface. In lieu of sending slip out along this detachment as shortening progresses, a new fault propagated through the forelimb (analogous to the models of a stationary foreland wall from the previous section). This caused the transition from fault-bend to fault-propagation folding behavior, which was similar to the change in structural styles observed in our models when the foreland wall was held fixed or the upper detachment was strengthened.

## 3.7 CONCLUSIONS

We find that investigating a wide range of geometric and mechanical properties of fault-related folds with the discrete element mechanical modeling method has helped to identify the factors that are most favorable for the development of fault-bend, transitional, and fault-propagation folds. Observations of the resulting structural geometries and distribution of distortion over time provide insight into the timing, location, and style of deformation that is responsible for these observed changes. We find that increased effective friction along the upper detachment and the restriction of motion of the foreland wall have the strongest influence in driving the development of fault-propagation folds. Fault dip, relative mechanical layer strength, and mechanical layer thickness also play an important role in driving the transition between

fault-bend and fault-propagation folding behavior, while some properties, including bulk material strength, rebonding, and sedimentation rate, have negligible effects. These factors primarily exert their influence on structural style development by influencing the dominant deformation mechanisms; low fault dips, high layer strength anisotropy, and thinly spaced layers lead to more deformation by the flexural slip process, allowing the intervening layers to maintain more of their original strength and to transmit stress and deformation into the foreland. This promotes the development of fault-bend folds. In contrast, high fault dips, decreased layer strength contrast, and widely-spaced mechanical layers inhibit the flexural slip process, forcing deformation to be accommodated by more penetrative shear that acts as a mechanism for strain weakening in the forelimb and results in the development of more transitional and fault-propagation structures that accommodate a larger percentage of the deformation through internal model strain. We show through our natural examples that transitional structures exhibit these changes in fault-related folding style over time, and that these observations can be related to variations in geometric or mechanical properties.

## 3.8 Acknowledgements

We thank CGGVeritas for their provision of this data and support of the project, which was instrumental. We acknowledge support from the Petroleum Research Fund (ACS-PRF 48385-AC8) and the National Science Foundation (NSF-EAR 0711220). We also wish to offer special thanks to ExxonMobil and Chevron, which supported this research. Special thanks to Julia Morgan for helpful discussions and providing us with J2 visualization tools.

# Chapter 4

# Insights into the mechanics of fault-propagation folding styles

## 4.1 Abstract

Motivated by the wide range of geometries observed for fault-propagation folds, we investigate the role that mechanics plays in the variations observed for this structural class. Detailed structural measurements of a series of 15 fault-propagation folds from the Niger Delta, Argentina, and southeastern Asia reveal several relationships between aspects of the structural geometries. We find that the decrease in displacement up dip along the fault is well approximated by a linear trend that has a relatively consistent slope, and that this gradient remains constant for increasing total displacement. This suggests that the structures grow self-similarly, consistent with a range of kinematic models that have been used to describe them. Additionally, we observe that uplift has contributions both from rigid translation along a dipping fault and folding, and that the observed values lie between those predicted by the trishear and kink-style models, such as fixed-axis and constant-thickness fault-propagation folding. Finally, we find that fault-propagation folds have a bimodal fault dip distribution, with one group coincident with fault dips for fault-bend folds, and another, steeper

group that consists of steepening-upwards faults. By developing a series of discrete-element mechanical models, we find that mechanical layering plays a first-order role in the development of different styles of fault-propagation folding. Homogeneous materials produce trishear-like fault-propagation folds, while strongly layered materials produce structures more similar to the kink-style kinematic models. Comparison with the observations from natural structures indicates that these models reproduce the observed trends, and that most natural structures fall between these two models. This suggests that trishear and the kink-style (fixed-axis and constant-thickness) fault-propagation folding models may be thought of as end-members on a continuum of possible fault-propagation folding geometries that are largely dictated by the degree of mechanical layer anisotropy in the stratigraphy. Finally, we suggest that fault-steepening in highly anisotropic models may develop due to strain weakening of tightly-folded structural forelimbs.

## 4.2 INTRODUCTION

Fault-propagation folds are a common and important class of fault-related folds that form as faults propagate upward through sedimentary layers. Folding is localized at the tips of these faults, generally resulting in steep or overturned forelimbs that are considered characteristic of this structural style. Fault-propagation folds are one of the most common types of structure in contractional tectonic settings, including fold-and-thrust belts, accretionary prisms, and the compressive portions of passive margins. They are characterized by a general asymmetry, with long, gently dipping back-limbs and narrow, steeply-dipping fore-limbs, an active synclinal axial surface pinned to the fault tip, and a decrease in displacement along the fault as shortening is consumed in the folding process (Figure 4.1). While most fault-propagation folds

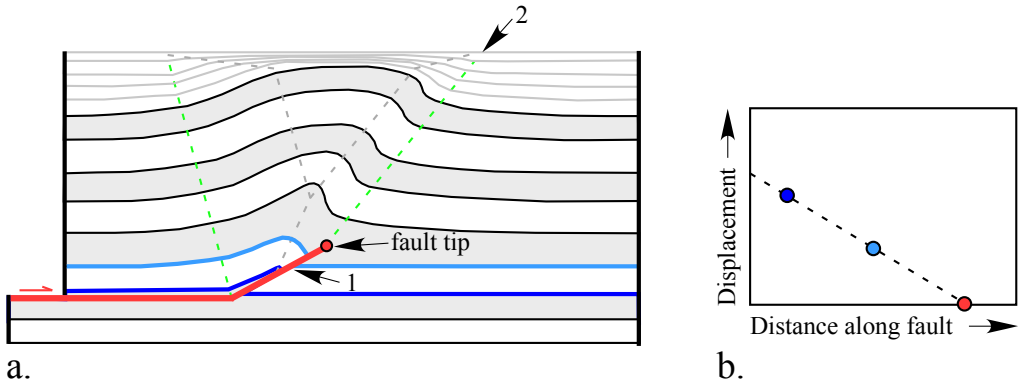


Figure 4.1: (*a*) Schematic of a typical fault-propagation fold (adapted from Shaw et al, 2005), characterized by asymmetric limb widths and dips, a decrease in displacement along the thrust fault toward the fault tip (1) and an active synclinal axial surface pinned to the fault tip (2). (*b*) Decrease in displacement as a function of distance along the fault toward the fault tip.

share these characteristics, natural examples exhibit a wide range of structural geometries (e.g., limb dips and widths), as illustrated in examples at a range of scales and locations shown in Figure 4.2. This diversity has motivated the development of a great number of quantitative kinematic models to describe the deformation of these structures over time. Many of these models are capable of describing a subset of these structures, but no single model has proven able to adequately capture the natural variability of these structures that has been observed in seismic reflection and field-based studies. This wide range of structural geometries presents a significant challenge in selecting the most appropriate models to interpret them, and poses many unanswered questions about the factors that control the development of these structures in different geologic settings.

An understanding of the geometry and kinematics of fault-propagation folds is essential to many applications in earth science. As this class of structures is ubiquitous in fold and thrust belts throughout the world, proper identification and characterization of fault-propagation folds is essential to studies that seek to define the magnitudes

of upper crustal shortening. An understanding of fault-propagation folds is also particularly important to the assessment of seismic hazards. Many active blind thrust faults are best characterized as fault-propagation folds [e.g., Allmendinger and Shaw, 2000; Carena and Suppe, 2002, and others]. In these cases, the faults do not reach the Earth's surface, and thus pose a particular challenge to researchers seeking to define fault slip rates, the ages of past earthquakes, and other factors that determine the seismic hazard. For this class of structure, only folds and uplifted features (e.g., terraces) above the fault are observable at the surface. Thus, a kinematic model must be used to relate these surface features to fault properties at depth. The ability to estimate the depth of the tip of the fault and the fault dip are essential, as these determine the area of the fault that lies within the seismogenic zone, and therefore the magnitude of earthquake that the fault is capable of generating [Kanamori, 1977; Wells and Coppersmith, 1994]. Moreover, inferred slip rates are used to determine earthquake recurrence intervals. The accuracy of these forecasts are largely dependent on the applicability and effectiveness of the fault-propagation fold model that is used to interpret the structure.

Fault-propagation folds also provide structural traps for many of the largest petroleum fields in the world. As the forelimbs of these structures are often steeply dipping, seismic reflection imaging in that part of the structure is often limited. The location of the fault and fault tip may have a significant impact on the estimation of reservoir volume, thus the ability to predict the precise geometry of the structure in the poorly imaged forelimb zone is often critically important. These predictions are generally made through a kinematic fault-propagation fold model, and can have a significant impact on accuracy of reservoir volume calculations. Additionally, a kinematic understanding of how the structure grew over time also helps to define the timing of structural growth relative to hydrocarbon source maturation and migration. Finally,

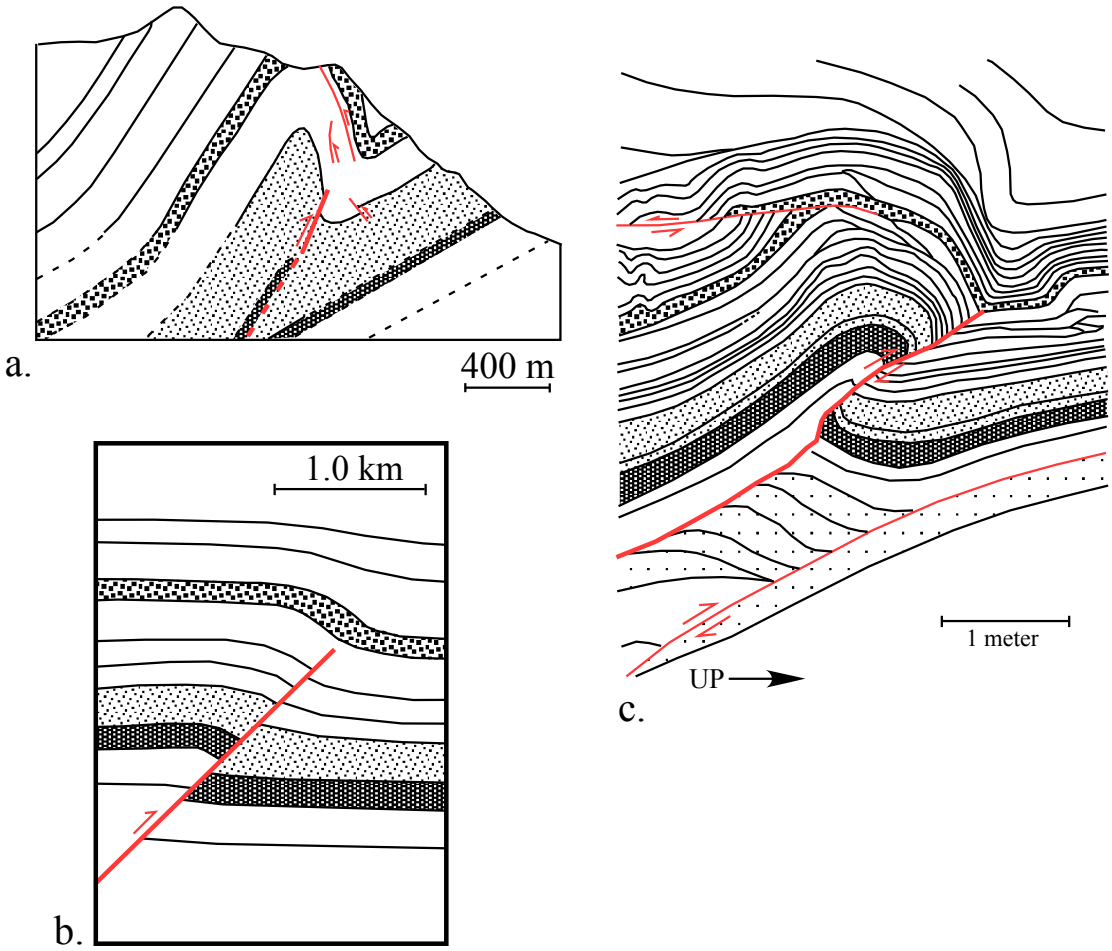


Figure 4.2: Three examples illustrating the range of geometries observed for fault-propagation folds. (*a*) Elliot mountain, in the hanging wall of Sulfur Mountain thrust, Canadian Rockies, adapted from Erslev and Mayborn [1997]; (*b*) Line tracing of seismic reflection data, adapted from Hughes and Shaw [2012], Niger Delta; (*c*) Eagle Rock, Virginia, Valley and Ridge province of Appalachians, adapted from McConnell et al. [1997].

strain distribution in the reservoir, which may control fracture permeability, is often dependent on the deformation history of the structure. This study is motivated by these applications, as well as the availability of high-quality seismic reflection data and numerical modeling tools that can be used to further constrain the geometries, kinematics, and mechanics of fault-propagation folds. Specifically, we seek to quantify geometric aspects of natural structures in order to assess if some aspects of the structures are common to all fault propagation folds while others can be used to distinguish different classes of these structures that are implied by existing models. We find that gradients in displacement toward the fault tip, and the relationship between maximum displacement and structural relief are consistent across the 15 structures that we studied. Additionally, we find a bimodal fault dip distribution for fault propagation folds, with the steeper faults displaying characteristic steepening-upward geometries. We then generate a range of mechanical models that satisfy these observations while also helping to identify the factors that lead to the wide range in fold shapes that has been previously observed in this structural class. We find that variation in mechanical layer anisotropy is the most important factor that determines the folding style and most appropriate fault-propagation folding model to describe it.

### 4.2.1 Kinematic models of fault-propagation folding

Folds with steep forelimbs that are associated with faults have been recognized in the field for over a century [e.g., Heim, 1919]. Interpretations of these structures fell into three main categories: folding was subsequently cut by a fault (i.e. break-thrust model in Willis and Willis [1934]), faulting was followed by drag folding [e.g., Fox, 1959], and contemporaneous folding and faulting [e.g., Dahlstrom, 1970; Suppe and Medwedeff, 1990]. In the first case, folds developed and were subsequently cut by a thrust fault as in the break-thrust [Willis and Willis, 1934] and stretch thrust [Heim,

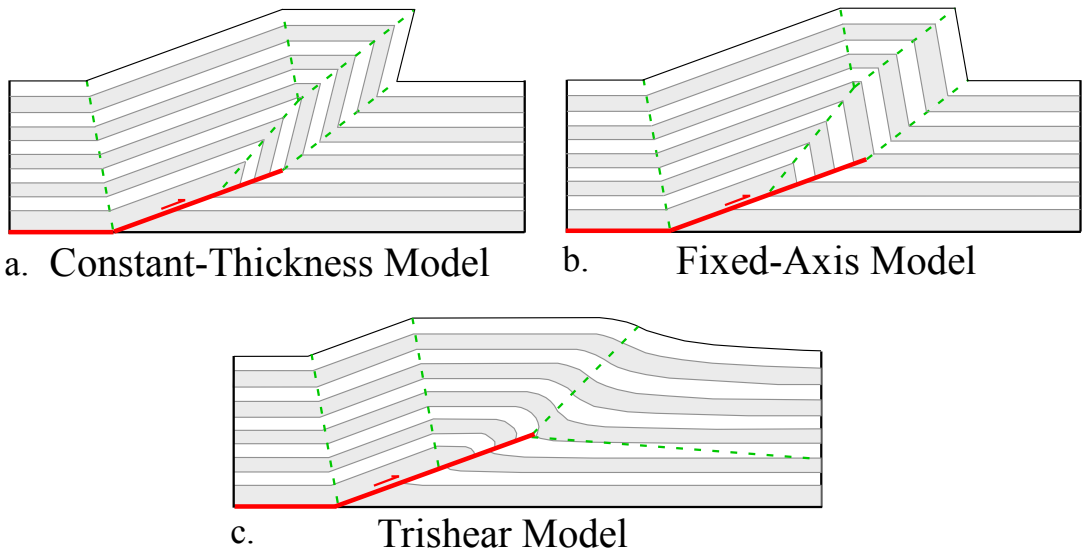


Figure 4.3: Commonly-applied kinematic fault propagation folding models: (*a*) Constant thickness, (*b*) Fixed axis, [from Suppe and Medwedeff, 1990] and (*c*) Trishear [from Erslev, 1991; Allmendinger, 1998, and others].

1919] concepts. In these cases, the fault geometry did not dictate the fold geometry. In the second case, the fault formed first, and friction along the fault interface caused "drag folding" to occur. In the final case, the folding and faulting were contemporaneous and genetically related such that the fault shape and fold shape are directly related. While all of these classes of structures are now thought to occur at different scales in nature, the last category—fault-propagation folds—are considered to be the most common mesoscale structures in fold-and-thrust belts and accretionary prisms [for example, Suppe and Medwedeff, 1990; Shaw et al., 2005, and many others].

Motivated by the wide range of observed structural geometries for fault-propagation folds, many different kinematic models have been developed. The most commonly applied kinematic models fall into two end-member classes: kink-style models, such as fixed-axis and constant-thickness fault-propagation folding [Suppe and Medwedeff,

1990], and models that are characterized by distributed, non-localized strain, such as trishear fault-propagation folding [Erslev, 1991; Allmendinger, 1998]. These "kink-style" models are characterized by planar fold limbs separated by angular axial surface or hinge zones, and deformation is accommodated largely by shear parallel to bedding orientation. This folding mechanism is consistent with field observations of flexural slip in many natural structures. One of the first attempts to model contemporaneous folding and faulting in fault-propagation folds was a kink-style geometric model that preserves line length and cross-sectional area [Figure 4.3a; Suppe and Medwedeff, 1984, 1990, constant thickness variant]. Motivated by a variety of field observations, further variants on the kink-style model relaxed the layer thickness constraint, allowing for variable thickness of the fold forelimb [Figure 4.3b; e.g. Jamison, 1987; Suppe and Medwedeff, 1990, fixed-axis variant], externally-applied shear [Mitra, 1990; Mosar and Suppe, 1992], and constant fault dip [Chester and Chester, 1990]. In each of these models, the full geometry of the fold is prescribed for a given fault dip and amount of slip.

The alternative approach to modeling fault-propagation folds is through a penetrative shear oblique to bedding orientations. First proposed by Erslev [1991], trishear fault-propagation folding has been the most widely analyzed [e.g., Allmendinger, 1998; Cardozo et al., 2003] and applied [e.g., Allmendinger and Shaw, 2000; Carena and Suppe, 2002; Cardozo et al., 2005; Gold et al., 2006] of these models (Figure 4.3c). In this model, the hanging wall moves at a prescribed velocity relative to footwall, and a triangular zone in front of fault tip deforms through penetrative shear that is oblique to bedding plane orientations. As such, the limb gradually acquires its dip as the fault propagates upward, resulting in a fold that is characterized generally by spatially variable limb dips and layer thicknesses throughout the forelimb and rounded axial zones. These fold characteristics are supported by observations in some natural

structures of upward shallowing limb dips in syntectonic (growth) strata and intense deformation and bedding thickness changes in forelimbs. Additionally, a variety of other models have been developed to address a specific subset of the natural structures or to explain specific characteristics of these folds, including basement-involved models [Narr and Suppe, 1994; Spang and McConnell, 1997], forelimb dip steepening with increasing slip [McConnell, 1994], mixed-mode structures [Erslev and Mayborn, 1997], and double-tipped fault propagation [Kattenhorn, 1994; Johnson and Johnson, 2002; Tavani et al., 2006].

## 4.3 Empirical observations

For our study, we analyzed fault-propagation folds in a variety of tectonic settings: the Niger Delta passive margin fold-and-thrust system, offshore Nigeria; the Sierras Pampeanas, Argentina, a thick-skinned contractional continental setting; and, the offshore contractional regions of Southeast Asia. These structures were chosen in order to explore the range of tectonic settings in which these structures occur. They were classified as fault-propagation folds based on their consistency with the general features of this structural class, including folding above a thrust unassociated with a fault bend (Figure 4.4b,1), and an active synclinal axial surface (Figure 4.4b,2). Additionally, these structures were chosen for the exceptional quality of the seismic reflection data available, as this allowed for the accurate measurement of full fault and fold geometries and displacements.

We find that many aspects of the structural geometry, such as limb widths and dips, were highly variable and were not well correlated with other observations; this is consistent with observations from previous studies (McConnell [1994] and Figure 4.2). However, relationships between some aspects of the structural geometry are consistent

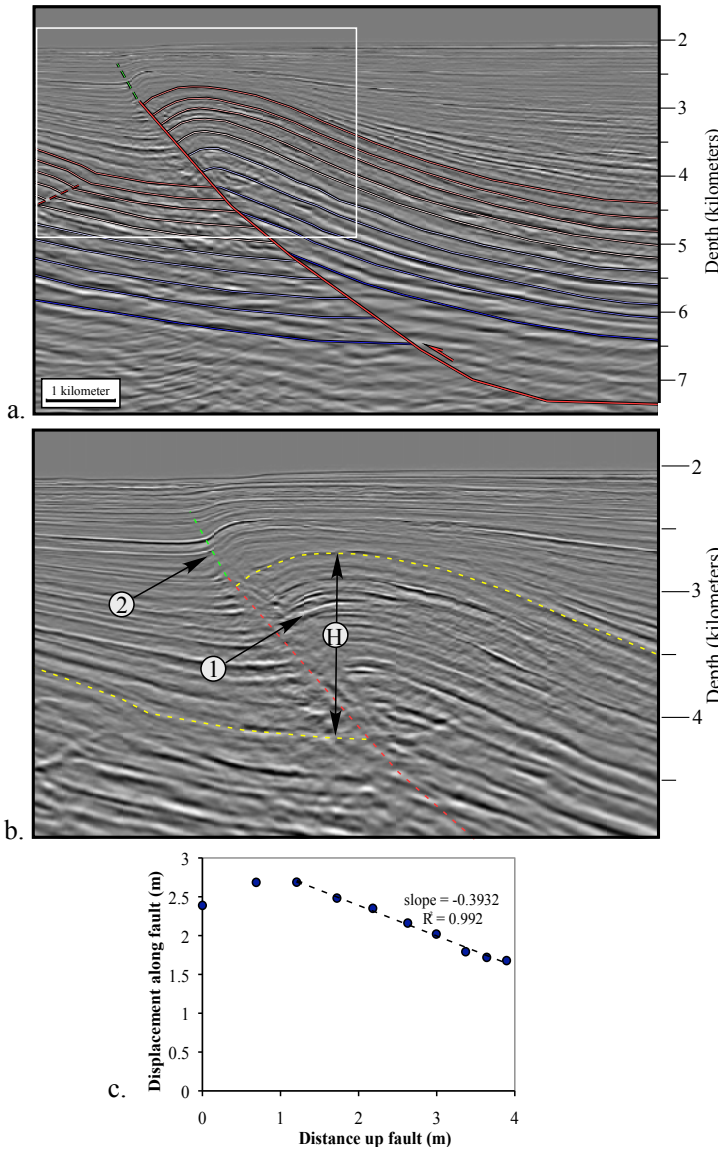


Figure 4.4: (*a*) Interpreted seismic reflection profile of a representative fault-propagation fold included in this study, from the southern outer fold-and-thrust belt, offshore Niger Delta. (*b*)Enlargement of region in white box, showing folding unassociated with an underlying anticlinal fault bend (1) and an active syncline pinned to the fault tip (2) serve to identify this structure as a fault-propagation fold. Structural relief measurement is shown (H). (*c*) Displacement-distance relationship, showing the decrease in displacement characteristic of fault-propagation folding for the upper portion of this structure. Data is owned and provided courtesy of CGGVeritas, Crawley, UK.

for all structures included in this study. As these observations appear to be robust for a wide range of natural fault-propagation folds, they represent a useful metric for classifying these structures in comparison with existing kinematic models and mechanical models.

### 4.3.1 Displacement-distance relationships

The decrease in displacement toward the fault tip is a diagnostic characteristic of fault-propagation folds. This decrease may be quantified by measuring the offset of different stratigraphic layers across the fault, and plotting that as a function of distance up-dip along the fault, termed the distance-displacement plot [Figure 4.1b; Williams and Chapman, 1983, and others]. Previous studies [Hedlund, 1997; Hughes and Shaw, 2012] have established that displacement decreases linearly toward the fault tip for the fixed-axis and constant-thickness kinematic fault-propagation fold models for a given fault geometry, and are linear for a constant fault dip and propagation-to-slip ratio for the trishear model as well.

An example of one of the structures analyzed in this study is shown in Figure 4.4. Stratigraphic layers were correlated in a grid of 2D seismic reflection data to ensure proper correlation across the fault (Figure 4.4a). General observations of an anticlinal fold unassociated with a fault bend, and evidence for an active synclinal fold in the syntectonic strata pinned to the fault tip serve to classify this structure as a fault propagation fold (Figure 4.4b). A measure of the displacement with distance along the fault indicates that, for the region of the structure that experienced a fault-propagation fold growth history, the slip gradient is well approximated by a linear trend ($R^2 = 0.992$) (Figure 4.4c).

A compilation of all of the displacement-distance relationships for the structures analyzed in this study reveals that gradients in displacement for many natural fault-

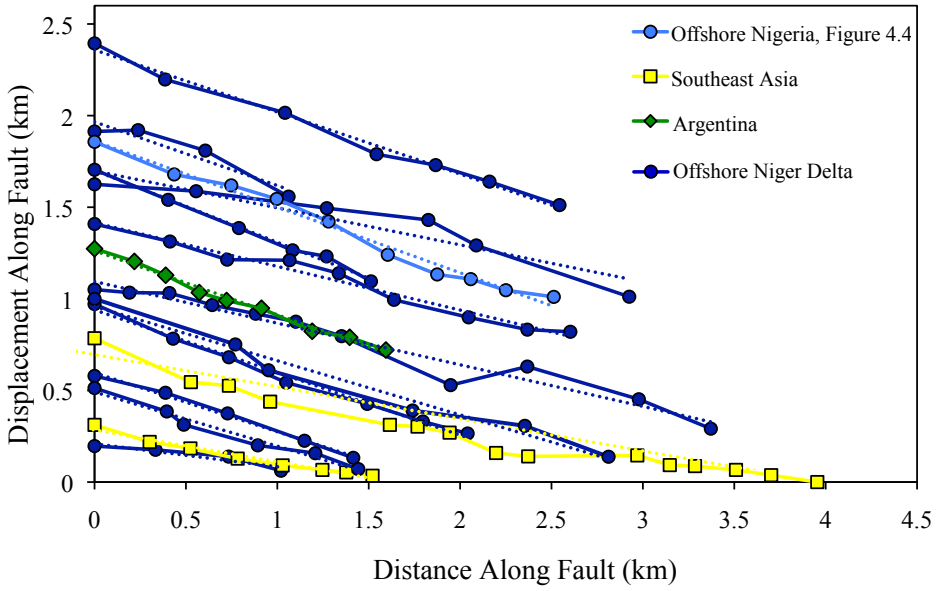


Figure 4.5: Compilation of distance-displacement measurements for all structures in this study.

propagation folds may be well approximated by a linear trend, and that the slope of this trend is relatively constant (Figure 4.5). The average slope of the decrease in displacement is -0.290 (St.Dev. = 0.081). There is not a systematic trend in displacement gradient as a function of increasing total displacement, suggesting that the structures grow self-similarly. This is further supported by observations of individual structures along strike (Figure 4.6). For the same structure at two positions along strike where the total displacement is different, we observe a common displacement gradient. In addition to supporting the idea that these structures grow self-similarly, this also lends credibility to the commonly-held view that observation of a structure along strike may be taken as a proxy for time-transgression.

We also find that there is not a strong correlation between displacement gradient and fault dip in the natural structures that we examined (Figure 4.7). Moreover, we find that the observed displacement gradients are generally lower than those predicted

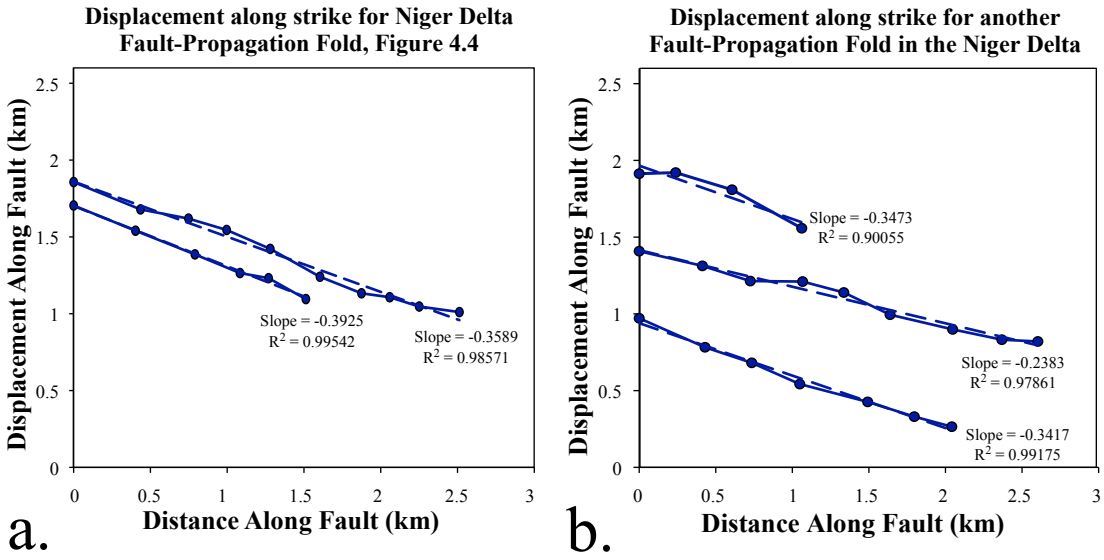


Figure 4.6: Displacement-distance relationships for two fault-propagation folds in the Niger Delta along strike, showing that with increasing displacement for a given structure, displacement-distance relationships are relatively constant.

by fixed axis and constant thickness fault-propagation fold models. As the gradient in displacement is largely a function of fault dip and forelimb dip and width, this reflects the fact that many of the natural structures are more open folds, with less steeply-dipping forelimbs, than are described by these kinematic models. Displacement gradient is a function of propagation-to-slip ratio, which may be freely varied in the trishear model. Thus, trishear models can reproduce our observed displacement gradients but make no prediction for the relationship between displacement gradient and fault dip.

### 4.3.2 Displacement/Structural Relief Relationships

Another trend that is apparent from analysis of the data is that there is a linear correlation ($R^2 = 0.82$) between the maximum amount of displacement observed along the fault and the maximum amount of structural relief, or uplift, that is measured

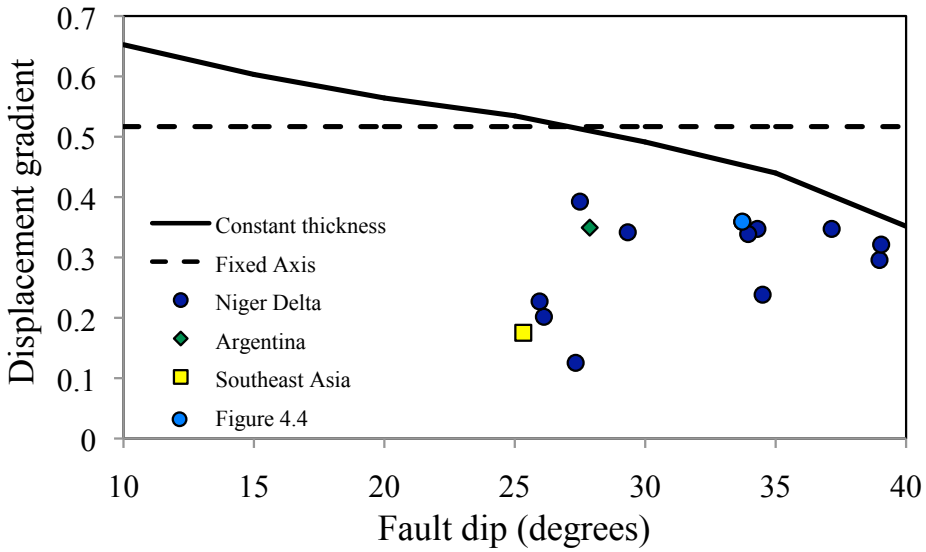


Figure 4.7: Displacement gradient as a function of fault dip, compared with kinematic model predictions.

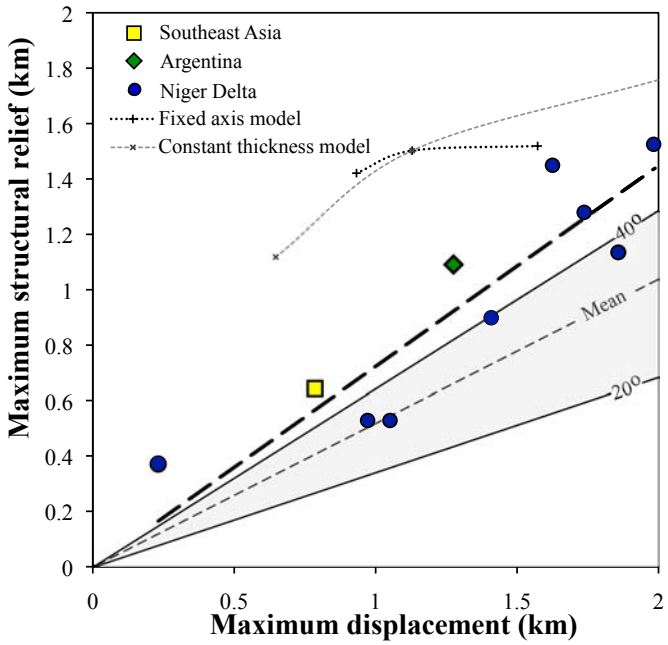


Figure 4.8: Relationship between structural relief and maximum displacement for natural structures (points). Heavy dashed line is the best fit to the observations. Fine dashed lines are the predicted relationship for the fixed axis and constant thickness models for fault dips of 20-40°, shaded area corresponds to the predicted relationship for the trishear model for fault dips of 20-40°.

(Figure 4.8). Such a general correlation is to be expected. However, the specific correlation value is significantly different than that predicted by most existing models. A component of uplift in these folds is produced purely as a function of the translation of material along a dipping fault. This "throw" is simply the vertical component of the displacement vector, and as such, varies as a function of fault dip, where shallowly dipping faults produce a modest amount of uplift per unit displacement on the fault, while steeply dipping faults produce a significant amount of throw-related uplift. This is the only mechanism of uplift described by trishear fault-propagation folding. In contrast, the fixed-axis and constant-thickness fault-propagation folding models predict a significant, additional component of uplift that develops due to the folding process. The weighted-average fault dips for our structures range from 23.6-39.0°. However, if the uplift observed for these structures was solely produced by fault throw, it would be consistent with an average fault dip of 46°, suggesting that throw alone is insufficient to explain the observed uplift. However, our observed relationship between uplift and fault slip is consistently lower than that predicted by these constant thickness and fixed axis fault-propagation fold models. This observation indicates that folding, in addition to faulting, is accountable for some fraction of the structural relief in natural structures. This "folding" component to uplift is not reproduced explicitly in trishear models but is not as large as would be predicted by both constant-thickness and fixed axis fault-propagation fold models.

### 4.3.3 FAULT DIPS

For each of these structures, we measured the dip of the faults. As the faults are generally non-planar, we report two different measures of fault dip–an average dip that is weighted by the length of each segment, and the maximum fault dip of any segment. We compare the maximum fault dip for the fault propagation folds in this

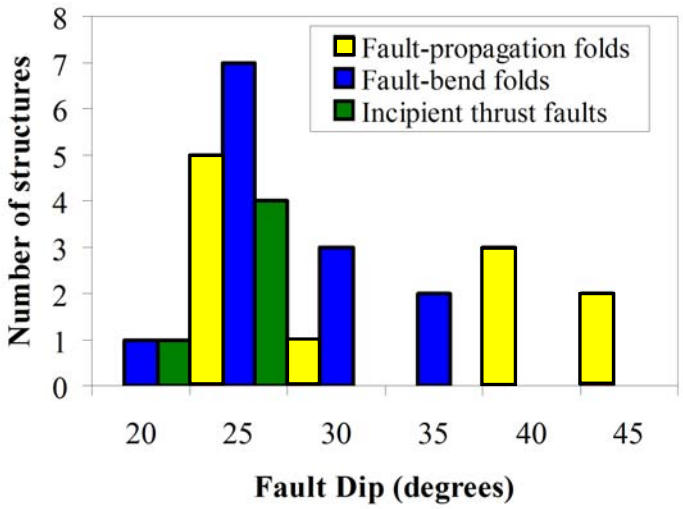


Figure 4.9: Distribution of average weighted fault dips for different structure styles, showing that at dips of 20-30°, all structural styles may develop, but above a threshold dip, only fault-propagation folds are observed.

study with fault dips for fault bend folds (including shear fault bend folds), and incipient faults (structures in which a fault plane reflector was imaged but virtually no slip was observable) in the Niger Delta. These structures were selected from a series of five regional seismic reflection profiles that were distributed throughout the southern outer fold-and-thrust belt of the Niger Delta, in order to ensure that the coverage was representative of the region. A plot of frequency of any given maximum fault segment dip illustrates that, while incipient faults and fault-bend folds generally coincide with a peak at 25-30°, fault propagation folds have a bi-modal fault dip distribution (Figure 4.9). One peak for fault-propagation folds is coincident with the fault-bend fold dips at 25-30°, but another broad peak exists between 40° and 50°. This suggests that below some threshold fault dip, both fault-bend and fault-propagation folds develop. Above this threshold, however, only fault propagation folds form.

## 4.4 Comparison with mechanical models

Motivated by these observations, we developed a suite of mechanical models in order to investigate what factors controlled the various geometric aspects of the structures that we observed. Previous studies on the mechanics of fault-propagation folding have been limited by the challenge that such structures are inherently emergent. That is, both faults and folds must grow during the deformation. This is difficult to achieve in continuum methods without dynamic remeshing. Moreover, geologic factors such as variations in mechanical stratigraphy and growth sedimentation are important aspects of fault-propagation folding, and these conditions are difficult to reproduce in both continuum and boundary element methods. Thus, we use the discrete-element modeling (DEM) method, as it is particularly well-suited to modeling large strains and localized, emergent deformation in materials that are capable of effectively describing upper crustal rocks and sediments [Morgan, 1999; Morgan and Boettcher, 1999; Strayer and Suppe, 2002; Finch et al., 2003, 2004; Strayer et al., 2004; Cardozo et al., 2005; Benesh et al., 2007; Hardy and Finch, 2006, 2007; Benesh, 2010, and others]. DEM is particularly well suited for modeling this type of structure for a number of reasons. Unlike continuum methods, particle based methods permit a dynamic evolution of the system and emergent structures to form. Additionally, DEM allows for large relative motion of individual particles at moderate to high strains, which leads to the formation of localized discontinuities in the deforming medium (such as faults or fractures). Finally, mechanical stratigraphy in these models can be specified precisely, along the deposition of stratigraphic growth sequences through the deformation.

### 4.4.1 Previous DEM studies

DEM has been used to study mechanical processes in many fields, including the physics of granular materials, geotechnical and mechanical engineering, and material science. It was first applied to geosciences in modeling the evolution of fault gouge zones [Mora and Place, 1993, 1994; Antonellini and Pollard, 1995; Mora and Place, 1998; Morgan, 1999; Morgan and Boettcher, 1999, and others]. However, since bulk material may be approximated as an assembly of individual particles, mechanical modeling of larger scale processes has also become possible through a calibration of inter-particle mechanical strengths to bulk material strengths. This has allowed for the application of DEM to a wide range of aspects of crustal deformation, including extensional faulting and folding [Finch et al., 2004; Seyferth and Henk, 2006], thin-skinned contractional systems [Burbridge and Braun, 2002; Strayer et al., 2004; Hardy and Finch, 2005; Hardy et al., 2009, and others] and the gravitational collapse of volcanic edifices [Morgan and McGovern, 2005a,b].

Previous applications of discrete element modeling methods to fault propagation folding have focused on the development of basement-involved structures [Finch et al., 2003; Hardy and Finch, 2006, 2007]. These studies found that mechanical layer strength and layer strength contrasts play an important first-order control on the fault-propagation folding style that develops. However, these models have utilized a model setup in which a boundary wall is driven upward as a rigid indentor into the cover sequence. Thus, displacement along much of the fault is prescribed by offset of the model boundaries. While this approach may be viewed as analogous to basement-involved fault-propagation folding, it has limited applicability to other structures within this structural class where faults nucleate and grow with variable displacements along their extents. Fold uplift and structural relief in these models are

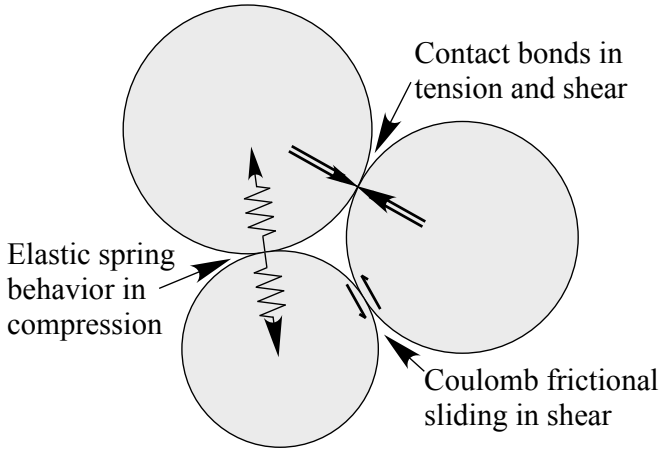


Figure 4.10: Basic particle interactions for the discrete element modeling (DEM) method.

also largely dictated by the boundary conditions, so they do not provide insight into these aspects of the fault-propagation folding process. As a result, we developed a new model setup that is better suited to investigating these aspects of structural growth, and may be considered more analogous to a thin-skinned contractional system.

### 4.4.2 The Discrete Element Modeling (DEM) Method

We used the discrete element modeling (DEM) method, as implemented in the Particle Flow Code in 2 dimensions (PFC2D) software package and based on the soft-sphere discrete element modeling method [Cundall and Strack, 1979; Itasca, 1999]. This approach models material as an aggregate of elastic disk-shaped particles that interact with each other and model boundaries (Figure 4.10). Particles interact through a resistance to particle overlap through a restoring force that is linearly proportional to overlap distance, and a frictional resistance to shear motion. Additionally, particles are bonded to provide strength in tension and shear, and are subject to a gravitational body force. Finally, elastic, user-defined walls serve as the driving mechanism and to contain the particle assemblage.

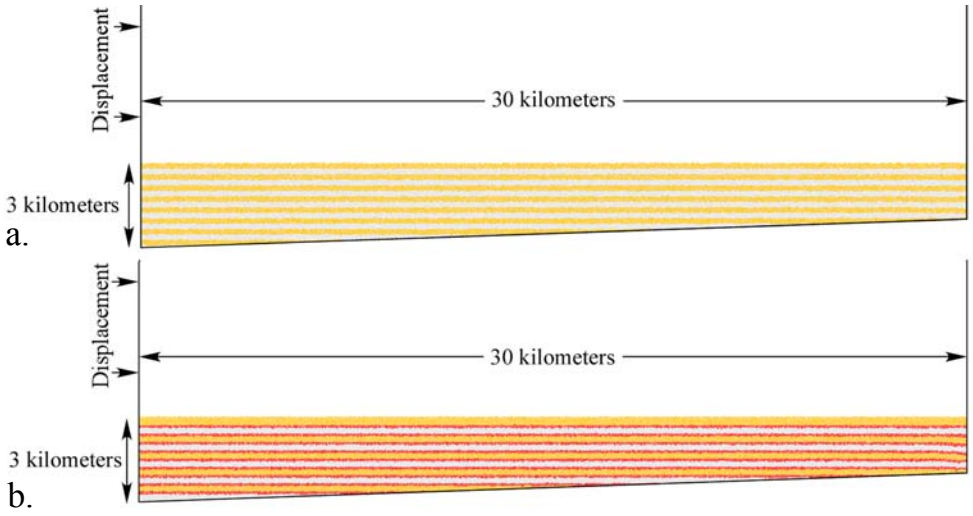


Figure 4.11: DEM model setup for ($a$) homogeneous and ($b$) layered models, where weak layers are shown in red. Models are rotated clockwise by 1° prior to deformation.

### 4.4.3 EXPERIMENTAL SETUP

In an effort to allow for the development of fully emergent contractional fault-related folds that are not localized by boundary conditions, we model contraction of a large wedge of material, defined by a base that is dipping 2 degrees and two vertical model boundaries (Figure 4.11). The boundaries are rigid, frictional boundary walls that are assigned a sliding friction of 0.57 for the side boundaries and 0.3 for the bottom boundary, which represents a basal detachment. Within these model boundaries, we generate either homogeneous or layered rock material by generating a series of particles from within a uniform size distribution of 24-33 meters (19-24 meters for the weaker layers), and assign them the density, elastic, and frictional properties listed in Table 4.1. These particles are then allowed to settle under their own weight, after which time, we remove particles above a given datum, allow for particle rebound, and repeat two additional times in order to create a flat surface to the layer. Layers are 200 meters thick (weak layers are 100 meters thick). This is repeated for all

| | | Standard Homogeneous | Standard Stratified | Weak Stratified |
|---|---|---|---|---|
| Particle-scale parameters | $\rho$ (kg/m$^3$) | 2600 | 2600 | 2600 |
| | $k_n$, $k_s$ (N/m) | $7x10^9$ | $7x10^9$ | $7x10^9$ |
| Regular layers | Particle radii (m) | 25-33 | 25-33 | 25-33 |
| | $\mu_c$ | 0.3 | 0.3 | 0.3 |
| | $\sigma_c$ (MPa) | 10 | 10 | 1 |
| | $\tau_c$ (MPa) | 600 | 600 | 60 |
| Slip layers | Particle radii | – | 19-25 | 19-25 |
| | $\mu_c$ | – | 0.0 | 0.0 |
| | $\sigma_c$ (MPa) | – | 0 | 0 |
| | $\tau_c$ (MPa) | – | 0 | 0 |
| Macro-scale parameters | Comp. layer thick. (m) | 200 | 200 | 200 |
| | Slip layer thick. (m) | 0 | 100 | 100 |
| | $\mu$ | 0.64 | 0.64 | 0.48 |
| | $Cohesion(C)$ (MPa) | 8.3 | 8.3 | 4.3 |
| | $Young's Modulus(E)$ (GPa) | 2.7 | 2.7 | 2.6 |

Table 4.1: Prescribed particle-scale mechanical properties and the resulting aggregate material properties, as determined by biaxial strength tests of numerical samples.

subsequent layers until a total thickness of 3 kilometers is attained. After the material is assembled, contact bonds are assigned to the particles. In the case of homogeneous models, all layers are assigned the same material properties, and different colors serve merely as passive markers in order to show strain patterns. In the layered models, weak layers are assigned an inter-particle friction of 0.0 and no contact bonds in order to simulate the presence of flexural slip surfaces.

We then rotate the entire model by 1°, creating a basal slope and surface slope that are each 1°. Deformation of the model is then implemented through horizontal displacement of the hinterland, or left, wall, while holding the opposite boundary stationary. We shorten the model by 3 kilometers, recording deformation after every 100 meters of shortening. As this predefined taper is below the critical taper of the material, this setup allows for individual structures to develop within the wedge as it is shortened and the model evolves toward its critical taper [Davis et al., 1983; Dahlen et al., 1984, and others]. Our focus is on the specific geometry of the structures that develop within the models. However, the model setup and resulting wedge mechanics behavior suggest that the stresses and displacements imposed by this type of loading are realistic and analogous to the environment in which natural fault-propagation folds form.

### 4.4.4 Material strength calibration

As described in Chapter 3, we conduct a series of biaxial strength tests to calibrate the inter-particle material properties specified in our models to bulk material strengths to ensure that they are representative of the values appropriate for rocks. The densities, interparticle friction and elastic strength, and contact bond values, and the correlative bulk material properties used for the models in this study are outlined in Table 4.1. We assign frictional strength and elastic moduli consistent with previous

studies [Benesh et al., 2007; Benesh, 2010, Chapter 3, and others]. Bulk material internal friction and cohesion values are within the range of rock laboratory measurements [Byerlee, 1978], and values for Young's Modulus are within the range deemed appropriate for basin scale applications [Serafim and Pereira, 1983; Bieniawski, 1984, and others]. Finally, we deem the use of these material strength values as appropriate as they result in realistic large-scale deformation pattern–signs that the material is either too weak (pervasive surficial slumping) or too strong (the development of unrealistic gaps or crevasses) are absent from our models. We investigate the role that variations in contact bond strength plays in the subsequent section.

### 4.4.5 General strength-dependent model results

We identify and record the location and geometry of faults in the model though observations of discrete changes in the particle displacement field. Distributed gradients in the displacement field are indicative of folding. Through these observations, we are able to characterize the development of fault and fold geometry in the model over time and compare these observations to the end-member kinematic models previously described. Additionally, through observation of distortional strain, or the second invariant of the strain tensor, we are able to monitor the location and intensity of strain throughout structural development.

In order to test the influence of mechanical strength on folding styles, we vary the contact bond strength by two orders of magnitude. Higher values of contact bond strength translate to higher peak strength, but more pronounced strain weakening. We find that for low contact bond strengths, the strength is easily exceeded and contacts are broken; however, since this material only experiences modest strain weakening, there is little preference to localize the deformation in a particular area over time, leading to shear that is distributed over wide areas, which favors folding

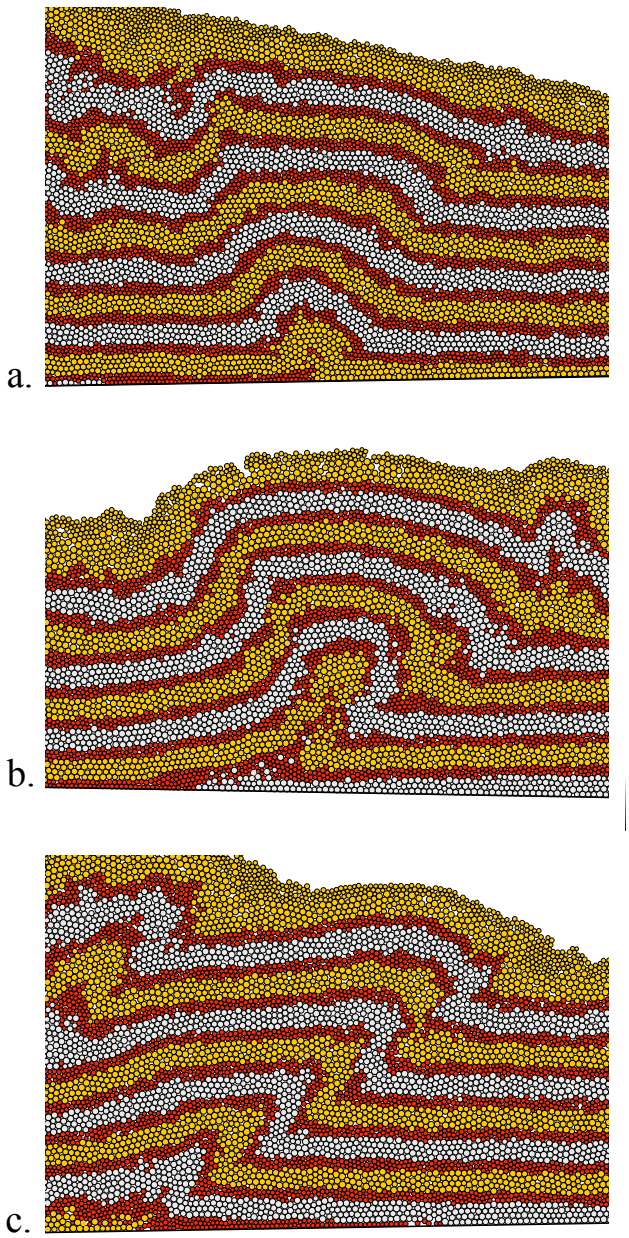


Figure 4.12: Characteristic deformation patterns for (*a*) low, (*b*) intermediate, and (*c*) high contact bond strengths, highlighting the role of peak strength and strain weakening in the relative importance of folding and faulting in the deformation process.

over faulting. Macroscopically, this leads to the development of large-scale folds that are best characterized as detachment folds [Figure 4.12a; Dahlstrom, 1990; Ephard and Groshong, 1995; Poblet et al., 1997; Hardy and Finch, 2005, and others]. At high contact bond strengths, once bond strength is exceeded in a particular location, this part of the model is substantially weaker than the surrounding material, leading to considerable strain weakening and favoring faulting over folding. At a macroscopic scale, this leads to the development of a highly localized shear zone, or fault that propagates very rapidly through the material and to the model surface, often leading to the development of a fault-bend fold [Figure 4.12c; Suppe, 1983]. In this case, the folding is simply responding to the displacement over bends in a defined and persistent fault surface. In contrast, at intermediate contact bond strengths, faults are localized but generally propagate more slowly. Folding localized above the fault tip accommodates a portion of the particle displacements in these cases (Figure 4.12b). Thus, we find that these conditions are most favorable for the development of fault-propagation folds. As a result, these are the contact strengths that are used for the models described in the remainder of this study.

### 4.4.6 Influence of mechanical layering on structural style

We find that the structures that develop in homogeneous models are most consistent with the trishear fault-propagation fold model. Observation of the model geometry over time shows a fault propagating upward from the detachment, at the tip of which is a triangular zone of distributed folding and layer thickening (Figure 4.13a). Observations of the distortional strain in these models highlight the localization of strain in the fault zone, with distributed deformation ahead of the fault tip that accommodates folding (Figure 4.13b). As the trishear kinematic model predicts distributed shear throughout the triangular region oblique to bedding orientation, the implication is

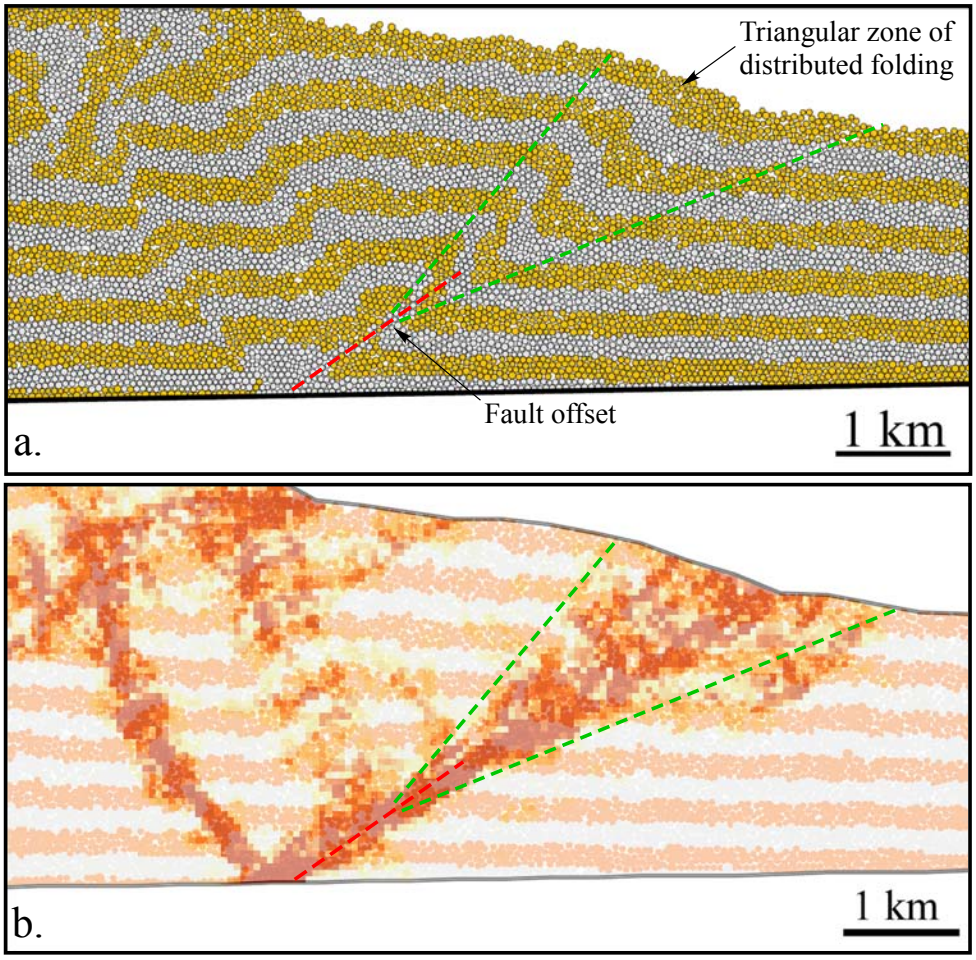


Figure 4.13: (*a*) Observed structural geometry for a homogeneous mechanical model. Fault and fold locations are inferred from analysis of the displacement field, and are broadly consistent with the trishear kinematic model. (*b*) Distortional strain is localized along the fault and anticlinal axial surface and distributed throughout a triangular zone ahead of the fault in the structural forelimb.

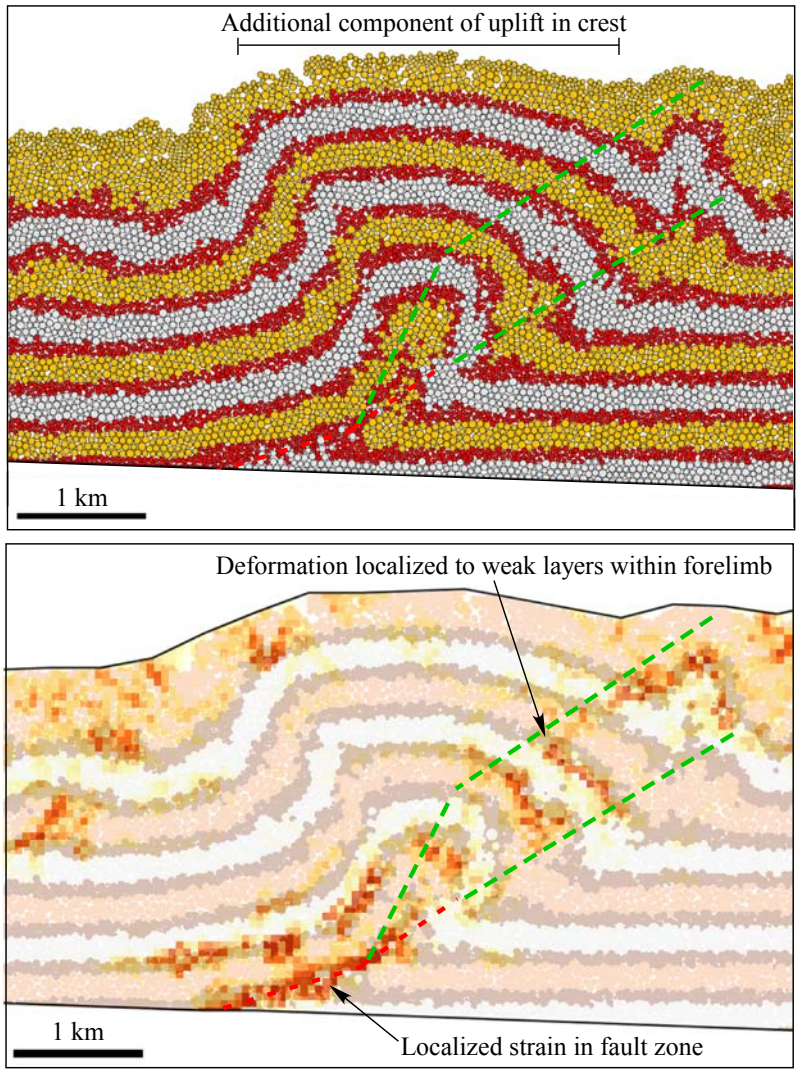


Figure 4.14: (*a*) Observed structural geometry for a layered mechanical model, broadly consistent with the kink-style fault-propagation folding kinematic models. (*b*) Distortional strain is localized along the fault and in weak layers.

that anisotropy of the material is not required in order for folding to occur by this mechanism. As such, our finding that homogeneous materials deform in this way is intuitively consistent with the implications of the kinematic model.

In contrast, strongly-layered materials display a very different style of folding (Figure 4.14a). In anisotropic models, we observe a fault propagating upward from the

basal detachment that steepens upward over time. We find that associated folding occurs in a zone above the fault tip that is bounded by two approximately parallel axial surfaces. Folds consist of fairly planar limbs, with limb dips that are relatively constant with depth. For a given amount of shortening, these structures also typically display more steeply dipping fold limbs than do the homogeneous models. These observations are all broadly consistent with the kink-style fault-propagation fold models. An analysis of distortional strain indicates that folding is accommodated by strain localized along weak layers in the forelimb, consistent with a flexural slip folding mechanism (Figure 4.14b). This style of folding in the mechanical models is in agreement with the kinematics implied by the kink-style fault-propagation models. These findings are consistent with recent finite element based mechanical models in which adaptive remeshing and an evolving strain-weakening constituitive model is employed [Albertz et al., 2011]. Additionally, they are consistent with the observation from a range of previous DEM models that mechanical layer strength contrasts have a first-order control on fault-related folding style for thick-skinned fault-propagation folds [Finch et al., 2003; Cardozo et al., 2005; Hardy and Finch, 2006, 2007].

## 4.5 Comparison of mechanical model results with empirical data

The mechanical models that we generated reproduce many qualitative aspects of fault propagation folds that are observed in nature and described by the kinematic models. To explore these relationships more fully, we now compare the displacement gradient and fault dip observations for the mechanical models, natural structures, and kinematic models (Figure 4.15). We find that the displacement gradients measured for the mechanical models are broadly consistent with those observed for natural structures in both their linearity and general slope. Moreover, displacement gradients

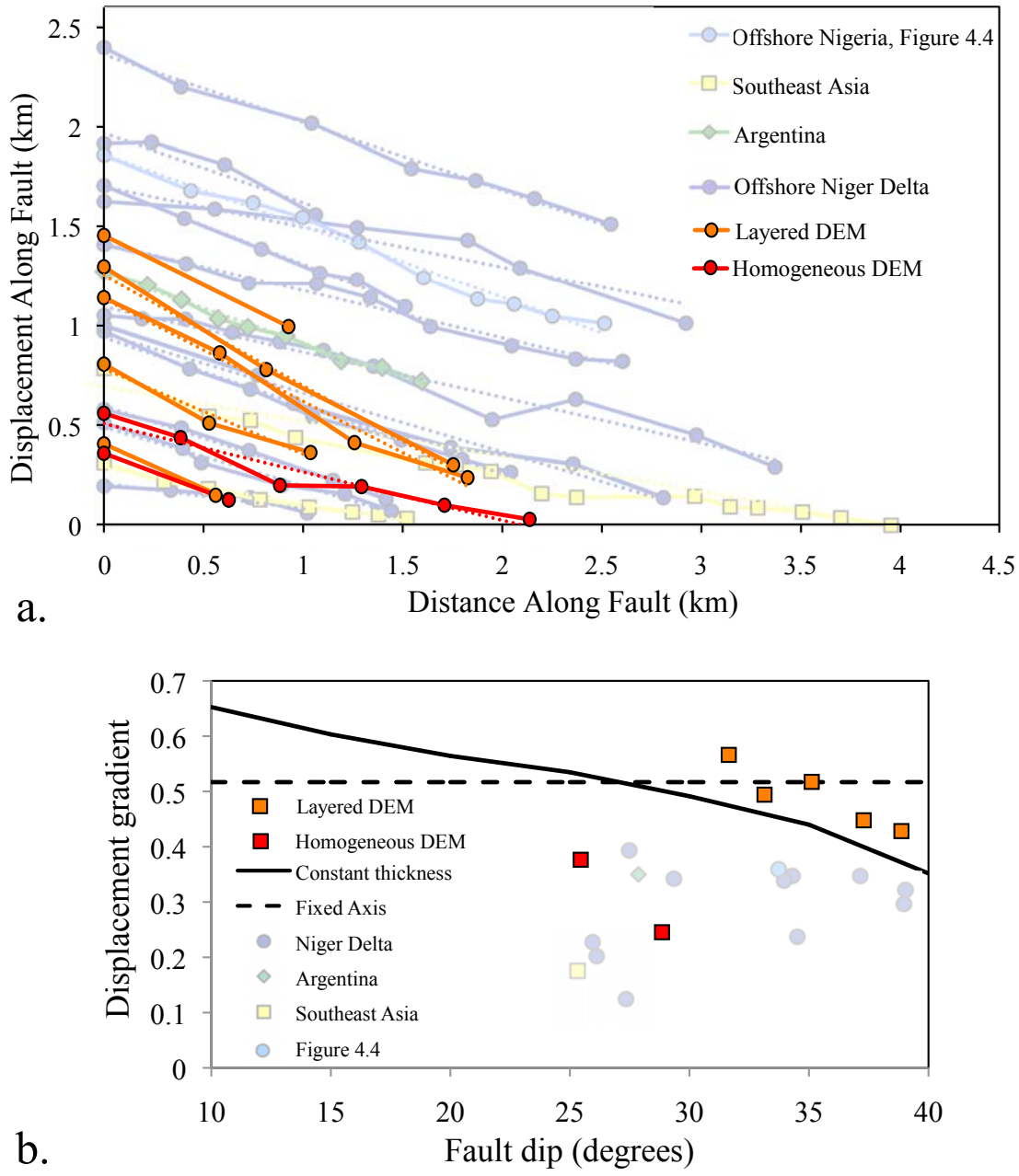


Figure 4.15: ($a$) A comparison of measurements of displacement gradients, ($b$) displacement gradients as a function of fault dip, and ($c$) structural relief as a function of maximum displacement for the mechanical models and the previously discussed kinematic models and empirical observations.

also remain constant with increasing total displacement (Figure 4.15a), consistent with the self-similar growth of the kinematic models and along strike variations in slip observed in our Niger Delta structures (Figure 4.6). Thus, linear displacement gradients, over a modest range of slopes, appear to be common characteristics to all fault-propagation folds models and structures that we have examined in our study. Undoubtedly, certain geologic conditions, such as polyphase growth, may lead to more complex displacement gradients. Nevertheless, our results suggest that linear displacement gradients may be characteristic of many fault propagation folds, which provides a basis to both identify these structures [Hughes and Shaw, 2012] and to infer fault displacements and fault tip locations in cases where structures are only partially constrained by geologic or geophysical data.

Our layered mechanical models also produce structures with higher fault dips and higher displacement gradients than structures produced in the homogeneous mechanical models. These layered models results are more consistent with the predictions from the fixed-axis and constant thickness models than with trishear models (Figure 4.15b). In contrast, homogeneous models produced fault-propagation folds that were geometrically more similar to the trishear model, and had lower fault dips and displacement gradients. Thus, we propose that mechanical layer anisotropy may be a primary control in the range of structural geometries observed for fault-propagation folds. Many of the observations from natural structures fall between the fault dip and displacement gradient values observed in our mechanical models. We interpret this relationship in the context of the role played by mechanical stratigraphy in defining fault-propagation fold style. Since layer strength contrasts in nature are highly variable and inherently gradational, it is likely that these natural structures exhibit behaviors that lie between our fully homogeneous and highly layered models. Given the similarities between these two sets of mechanical models and the kink-fold and

trishear kinematic models, the observations from natural structures imply that the kinematic models can be considered as end members. The degree of mechanical layering in natural structures—between homogeneous and fully layered—thus determines the degree to which they conform to the trishear and kink fold models, respectively.

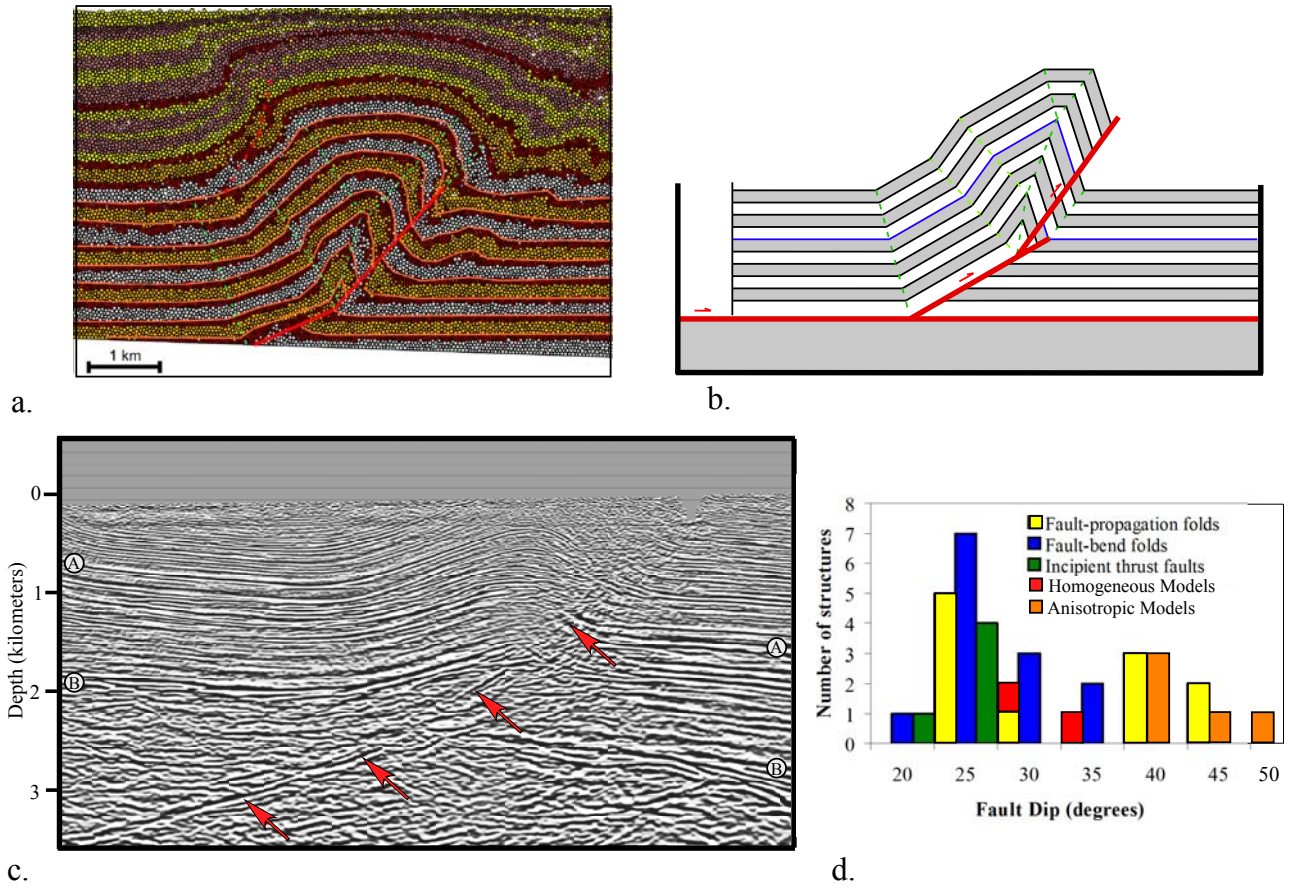


Figure 4.16: (*a*) A steepening upward fault-propagation fold in a mechanical model with growth stratigraphy. (*b*) Comparison with a kinematic model of a break-through kink-style fault-propagation fold illustrates the geometric similarities with the mechanical model. (*c*) An example of a steepening upward fault propagation fold from the Sierras Pampeanas, Argentina, from Hughes and Shaw [2012], with red arrows pointing to fault-plane reflectors and cutoffs. (*d*) A comparison of homogeneous and anisotropic model fault dips with empirical observations suggests that homogeneous models are consistent with the lower-dip peak, while anisotropic models are consistent with the higher peak for fault-propagation folds.

Finally, we compare the range of fault dips observed in the mechanical models with the observations from natural structures (Figure 16). We find that the trishear-style structures that developed in homogeneous models have fault dips of 20-30°. These values are consistent with the observed fault dips of thrust faults that display a range of structural styles, including fault-propagation folding. However, we find that in layered models, fault dips steepen upward (for example, Figure 4.16a), and the maximum fault dip of any segment for these structures is more consistent with the second peak that is associated with only fault-propagation folds. This suggests that the mechanical models are able to reproduce the range of fault dips observed in natural structures, and that fault dip may result from, or reflect, the style of fault-propagation folding (Figure 4.16). The lower range of fault dips associated with fault propagation folds are generally consistent with average thrust fault dips in many fold-and-thrust belts around the world. These dips are generally explained by Mohr-Coulomb failure criteria [Suppe, 1985, and other text books]. The steeper mode of fault dips associated with fault propagation folds, however, requires a different explanation. The development of steep thrust faults has been investigated by previous studies, and has been attributed to a variety of causes, including sedimentation rate [Barrier et al., 2002] and oblique slip [Harding, 1973, 1985, and others]. Additionally, a correlation between steep thrusts and fault-propagation folding is further supported by the general observation that when steeply-dipping normal faults are reactivated with a thrust sense of displacement ("inversion" structures), fault propagation folds are commonly formed [Harding, 1985; Gillcrist et al., 1987; McClay, 1989; Brun and Nalpas, 1996, and others].

Our mechanical models from this study suggest an alternative explanation that may account for the steepening upward of thrust faults and the associated development of fault-propagation folds. We propose that in layered models, flexural slip

allows for the development of tight folds with steep limbs. The folding associated with this process is asymmetrically distributed, as it is predominantly located in the hanging wall of the structure. As a result, the hanging wall directly above the fault tip experiences very high strains, and as a result, a high degree of weakening. Furthermore, as displacement occurs along a blind thrust fault, stress concentrations favor the subsequent activity of faults in orientations that would cause fault steepening [Kame et al., 2003], and thrust fault propagation may be encouraged by bedding-parallel slip in the region directly above the fault [Roering et al., 1997]. Thus, as the fault propagates further, it may be preferable for it to propagate through the forelimb above the fault tip due to preferable stress conditions and strain weakening, leading to an upward steepening of the fault.

## 4.6 CONCLUSIONS

We outline a series of observations from natural fault-propagation folds. We find that the decrease in displacement up dip along the fault is well approximated by a linear trend that has a relatively constant slope, and that this gradient generally remains constant for increasing total displacement. This suggests that the structures grow self-similarly, consistent with a range of kinematic models that have been used to describe them. Additionally, we find that these natural structures have uplift that has contributions from rigid translation along a dipping fault, and an additional component due to folding. This folding component of uplift is intermediate between that predicted by the kink-style and trishear fault-propagation fold models. Finally, our observations suggest that at low to intermediate thrust fault dips, all structural styles may develop, while above a threshold fault dip, fault-propagation folds tend to develop. These steeper faults tend to steepen upward toward the Earth's surface.

Furthermore, we find that mechanical layering plays a first-order role in the development of structural geometries; structures that are more consistent with kink-style models develop in models with strongly anisotropic rock properties, while structures more consistent with the trishear model develop in the mechanical models with homogeneous materials. Measured by displacement gradients and uplift patterns, natural structures appear to exhibit patterns that fall among and between the predictions of these kinematic theories. This implies that the degree of mechanical layering in natural structures may determine their fault-propagation folding style. Finally, we find that steepening upward thrust faults associated with fault-propagation folding develops in our mechanical models in which contrasting layer strengths are employed. We suggest that flexural slip allows for the development folding with steep limbs above the thrust fault, and that progressive weakening of the forelimb of the structure makes subsequent fault breakthrough in the forelimb preferable, leading to fault steepening.

## 4.7 Acknowledgements

We thank CGGVeritas for their provision of this data and support of the project, which was instrumental. We acknowledge support from the Petroleum Research Fund (ACS-PRF 48385-AC8) and the National Science Foundation (NSF-EAR 0711220). We also wish to offer special thanks to ExxonMobil and Chevron, which supported this research. Special thanks to Julia Morgan for helpful discussions and providing us with J2 visualization tools.

# Appendix A

## Complete mechanical modeling results

This appendix includes the complete suite of mechanical model results for Chapter 3. The first section includes the final model geometries. The second section is a table the measurements, observations, and interpretations that have been made for each model.

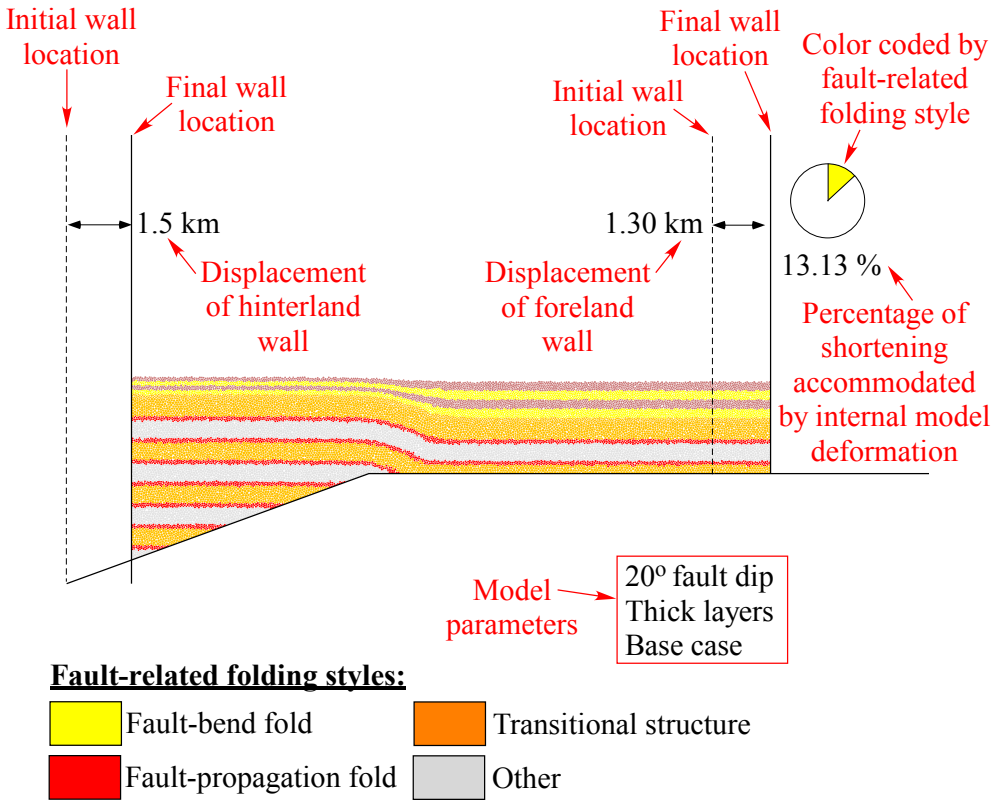


Figure A.1: Explanation (red text) of the features and annotation for each model result in the following figures.

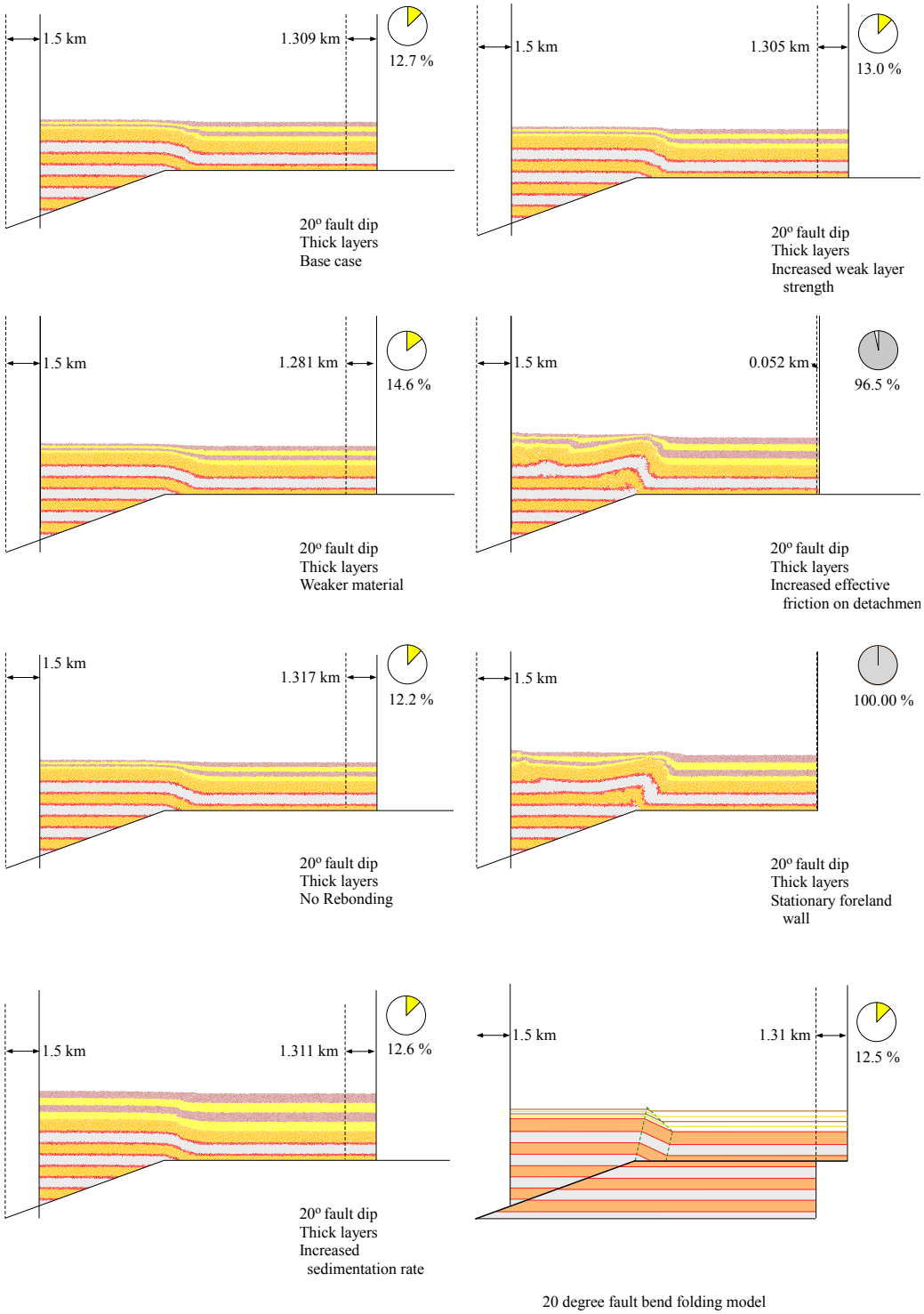


Figure A.2: Model results for 20° fault dip, thick mechanical layers. Annotation as described in Figure A.1.

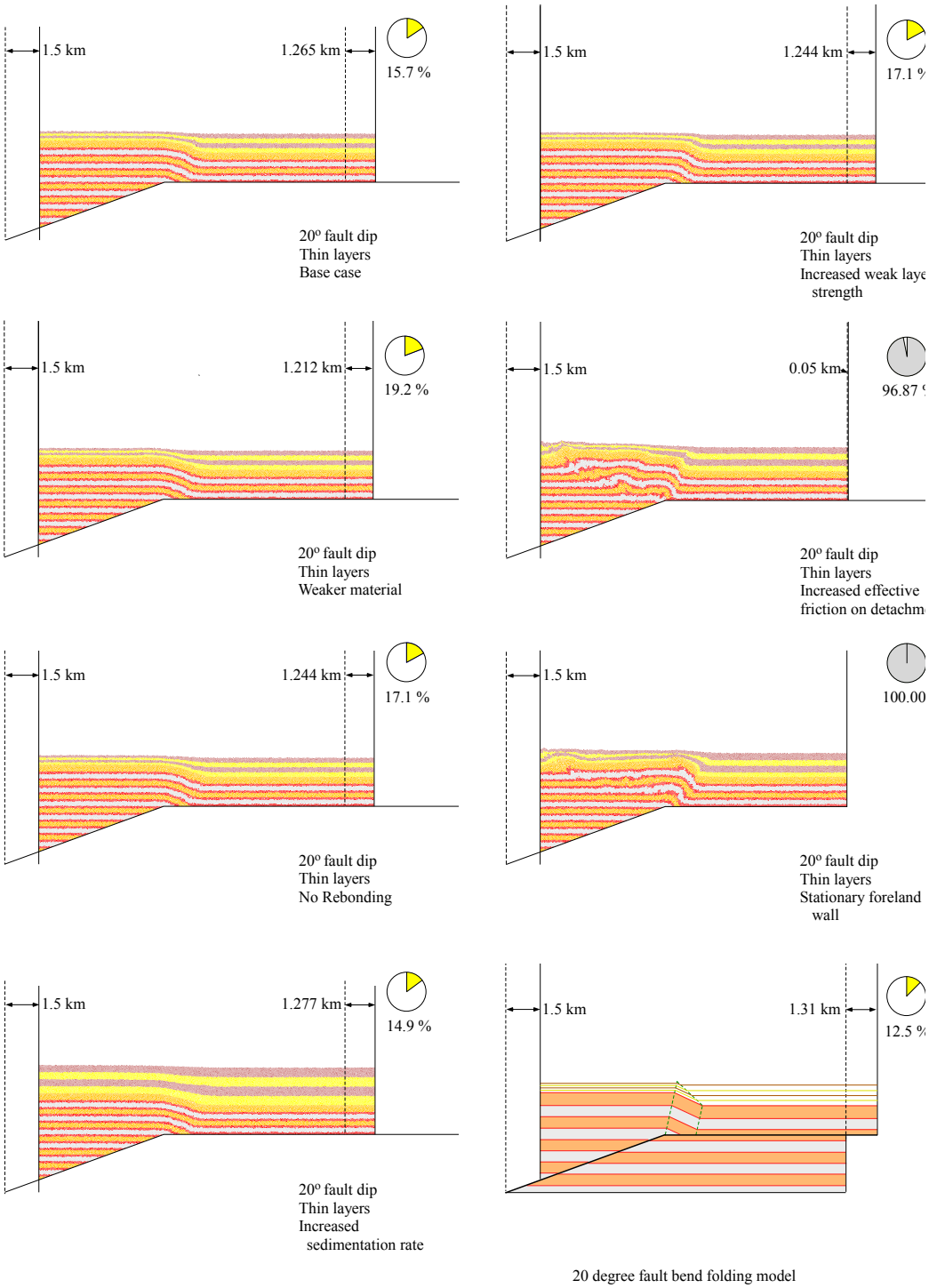


Figure A.3: Model results for 20° fault dip, thin mechanical layers. Annotation as described in Figure A.1.

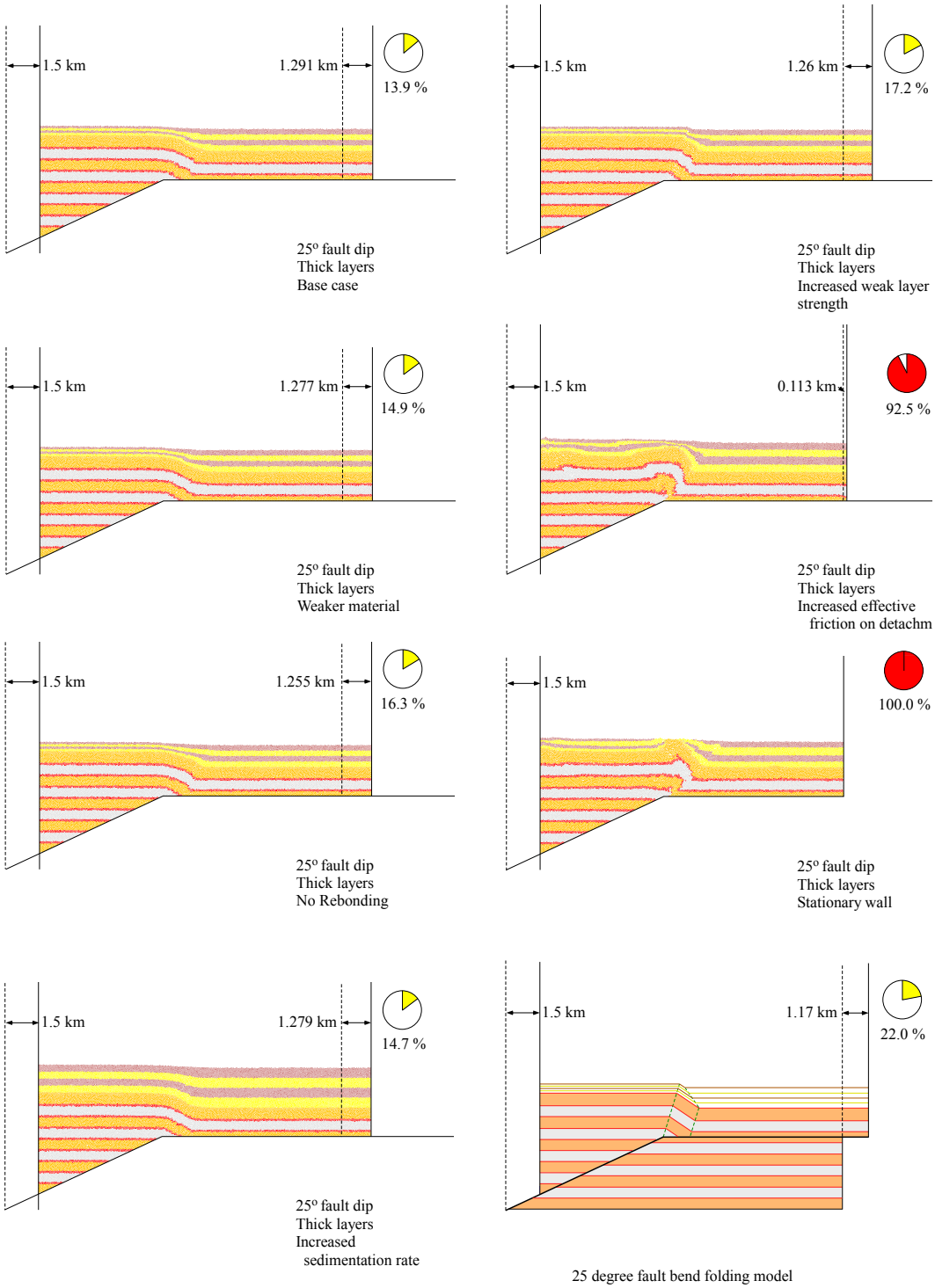


Figure A.4: Model results for 25° fault dip, thick mechanical layers. Annotation as described in Figure A.1.

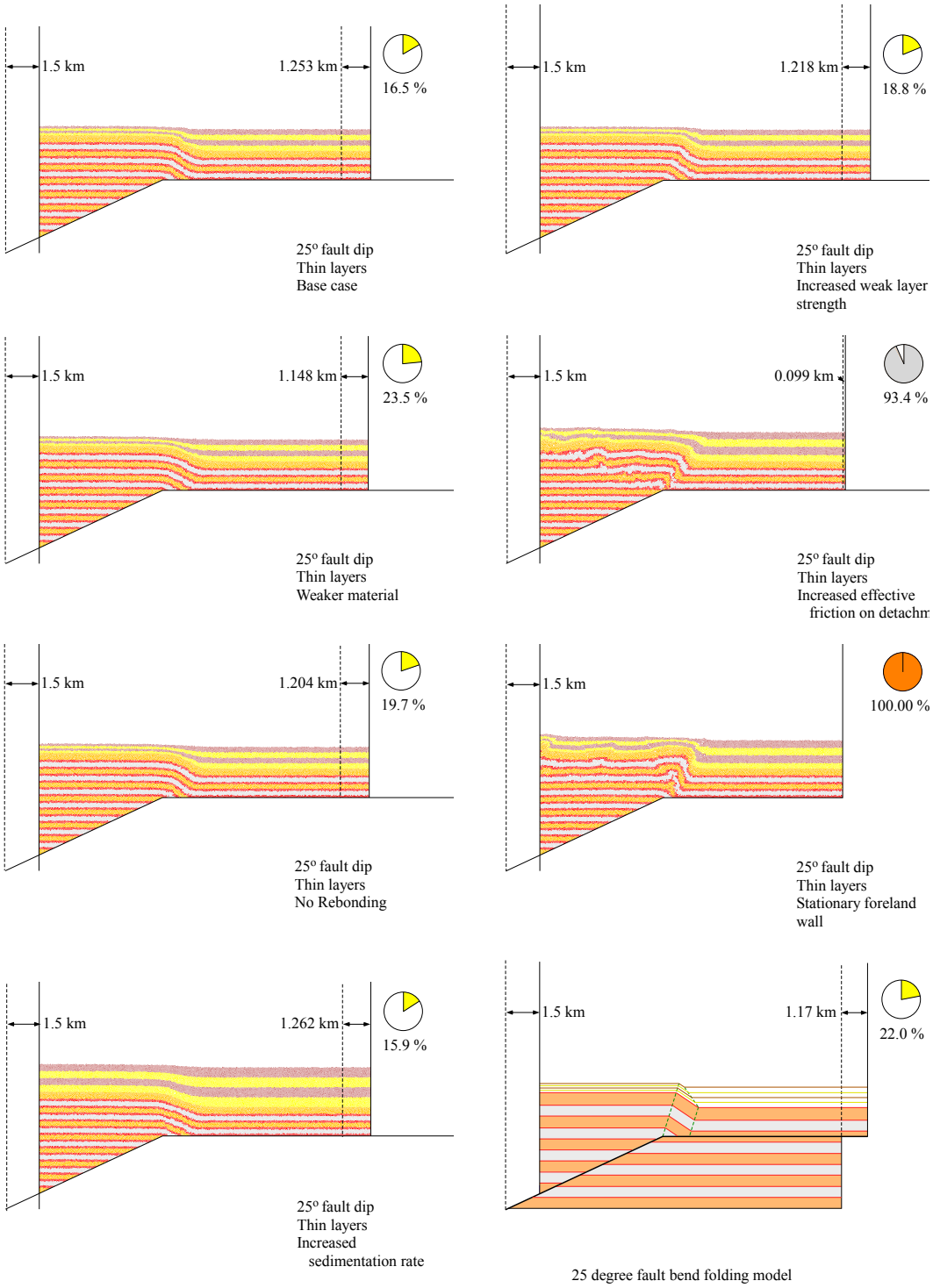


Figure A.5: Model results for 25° fault dip, thin mechanical layers. Annotation as described in Figure A.1.

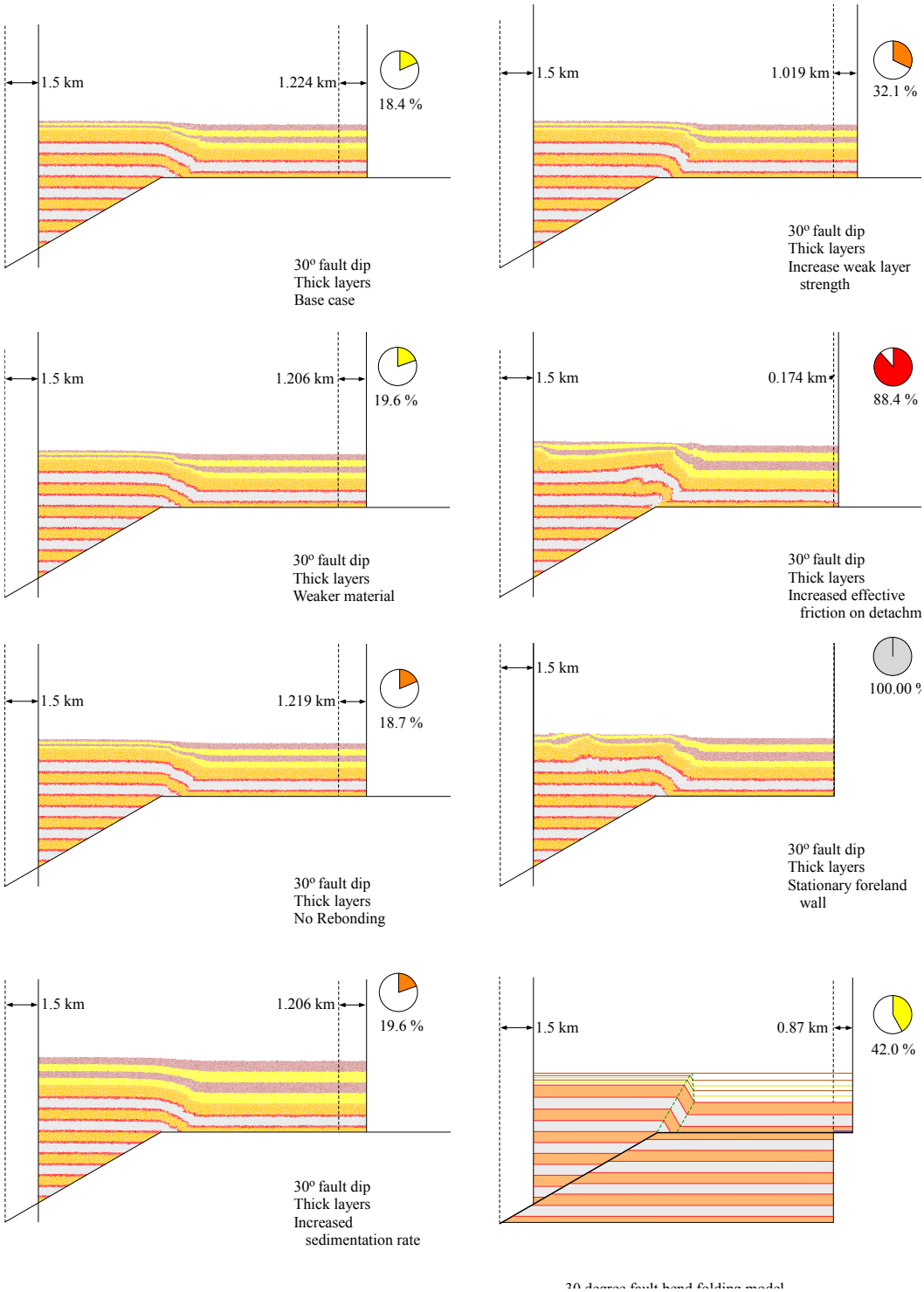


Figure A.6: Model results for 30° fault dip, thick mechanical layers. Annotation as described in Figure A.1.

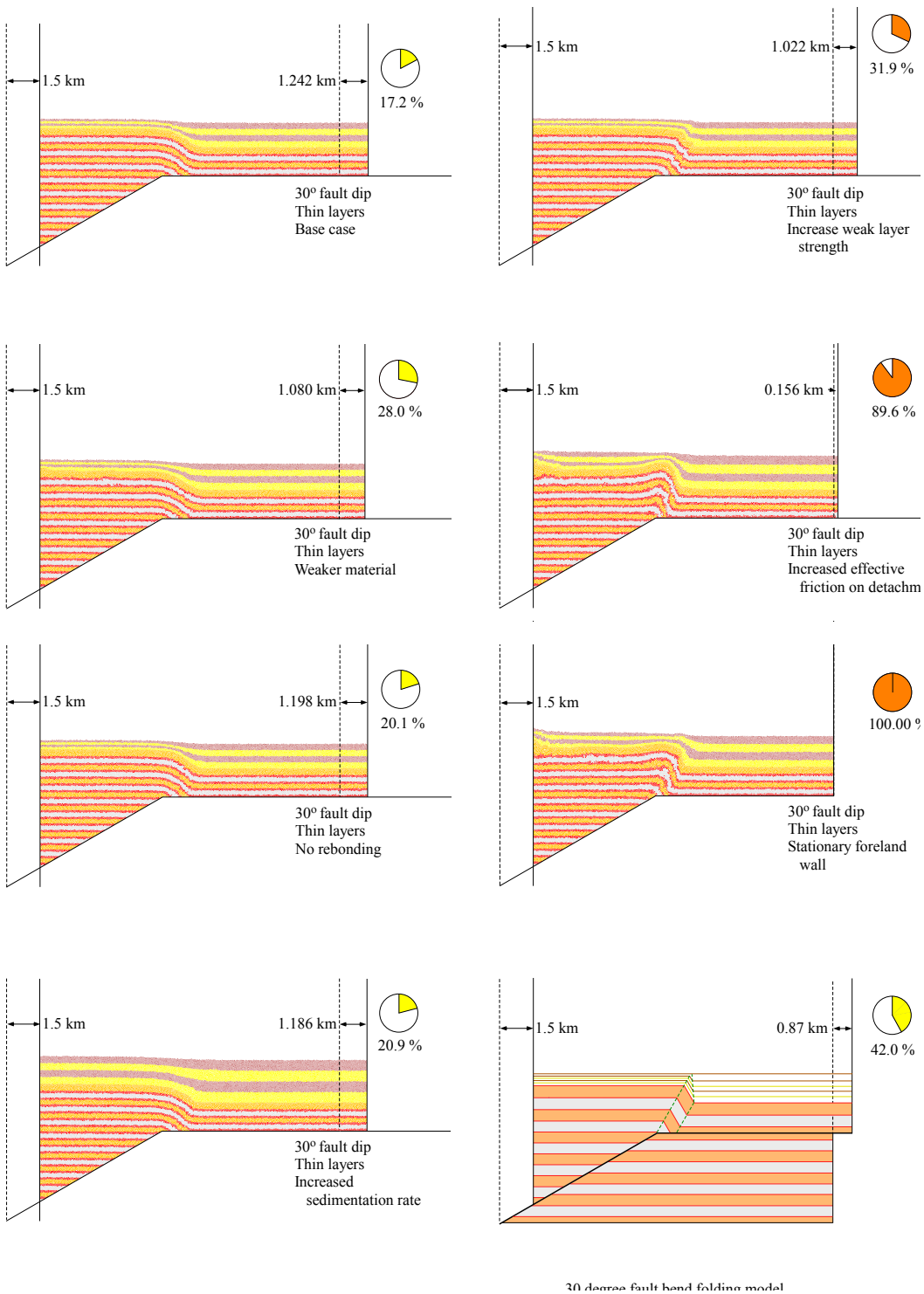


Figure A.7: Model results for 30° fault dip, thin mechanical layers. Annotation as described in Figure A.1.

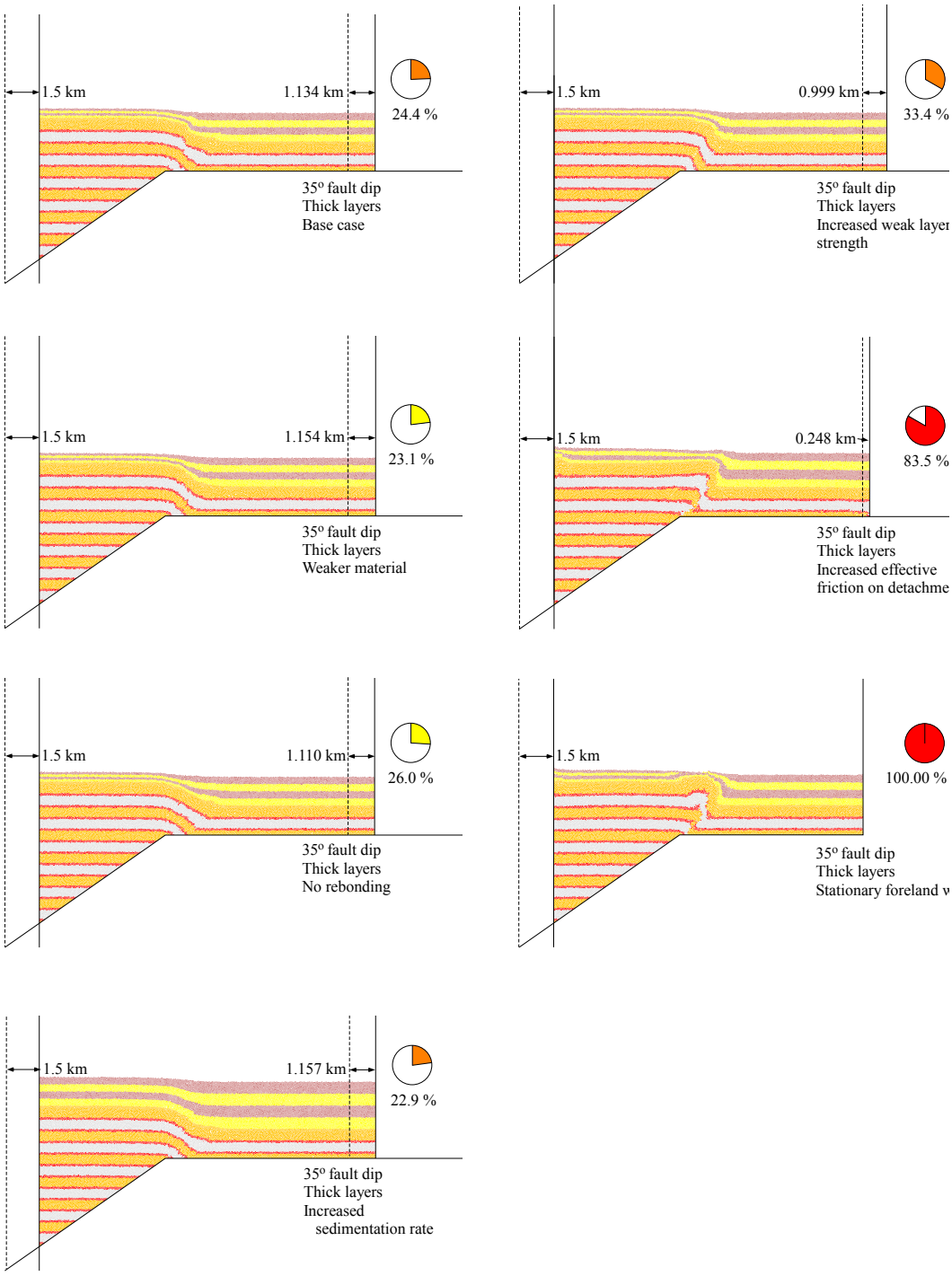


Figure A.8: Model results for 35° fault dip, thick mechanical layers. Annotation as described in Figure A.1.

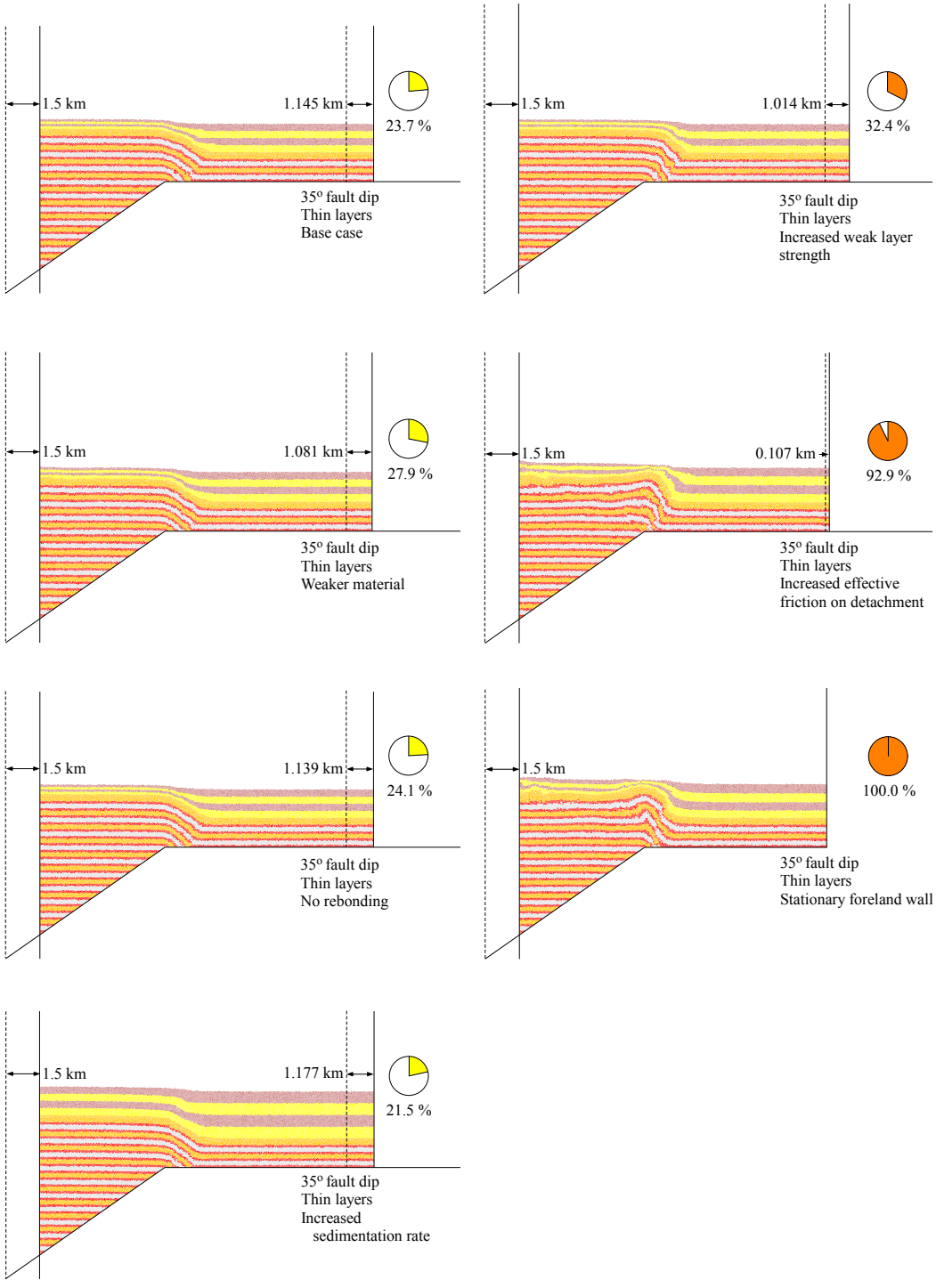


Figure A.9: Model results for 35° fault dip, thin mechanical layers. Annotation as described in Figure A.1.

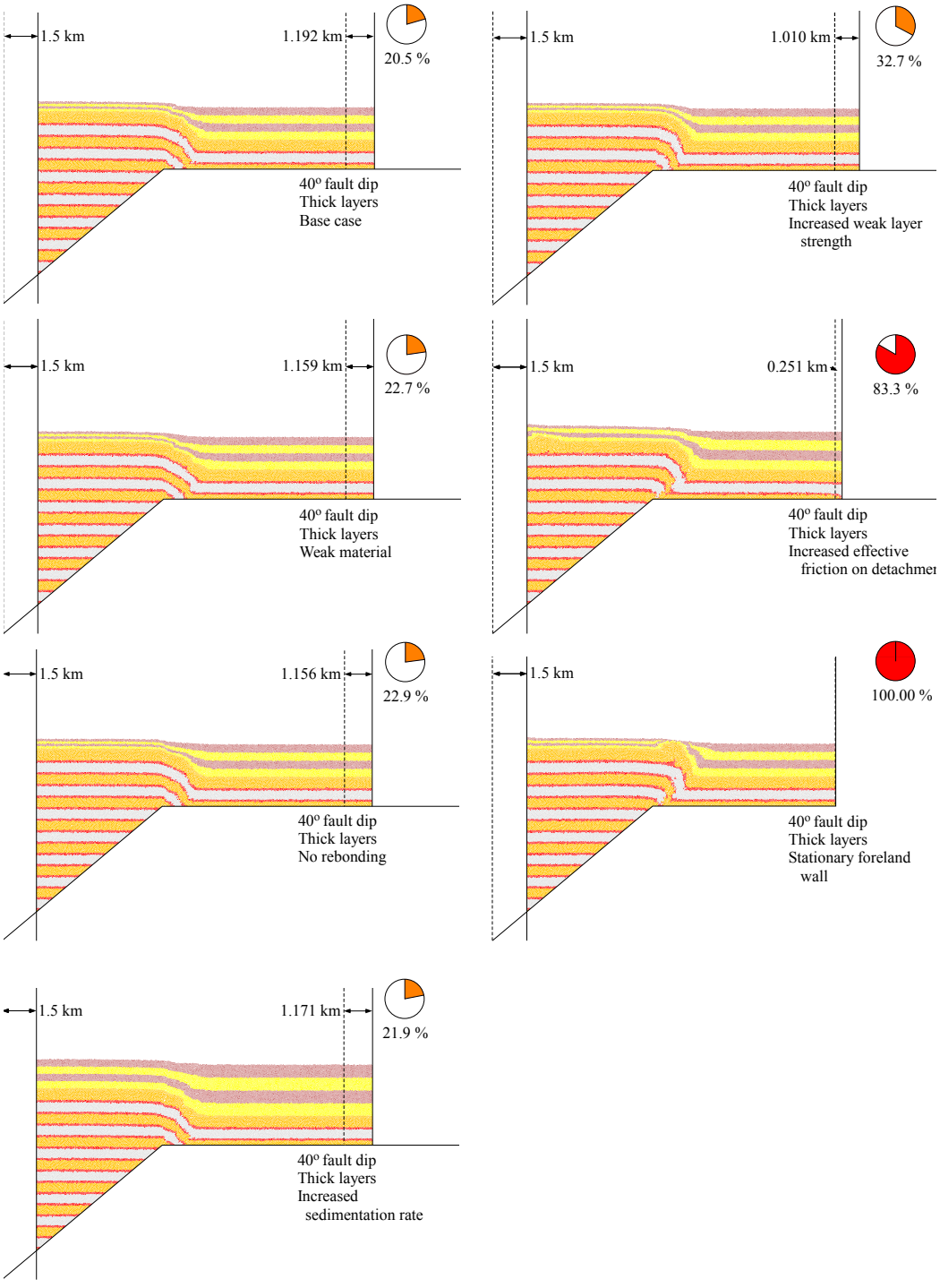


Figure A.10: Model results for 40° fault dip, thick mechanical layers. Annotation as described in Figure A.1.

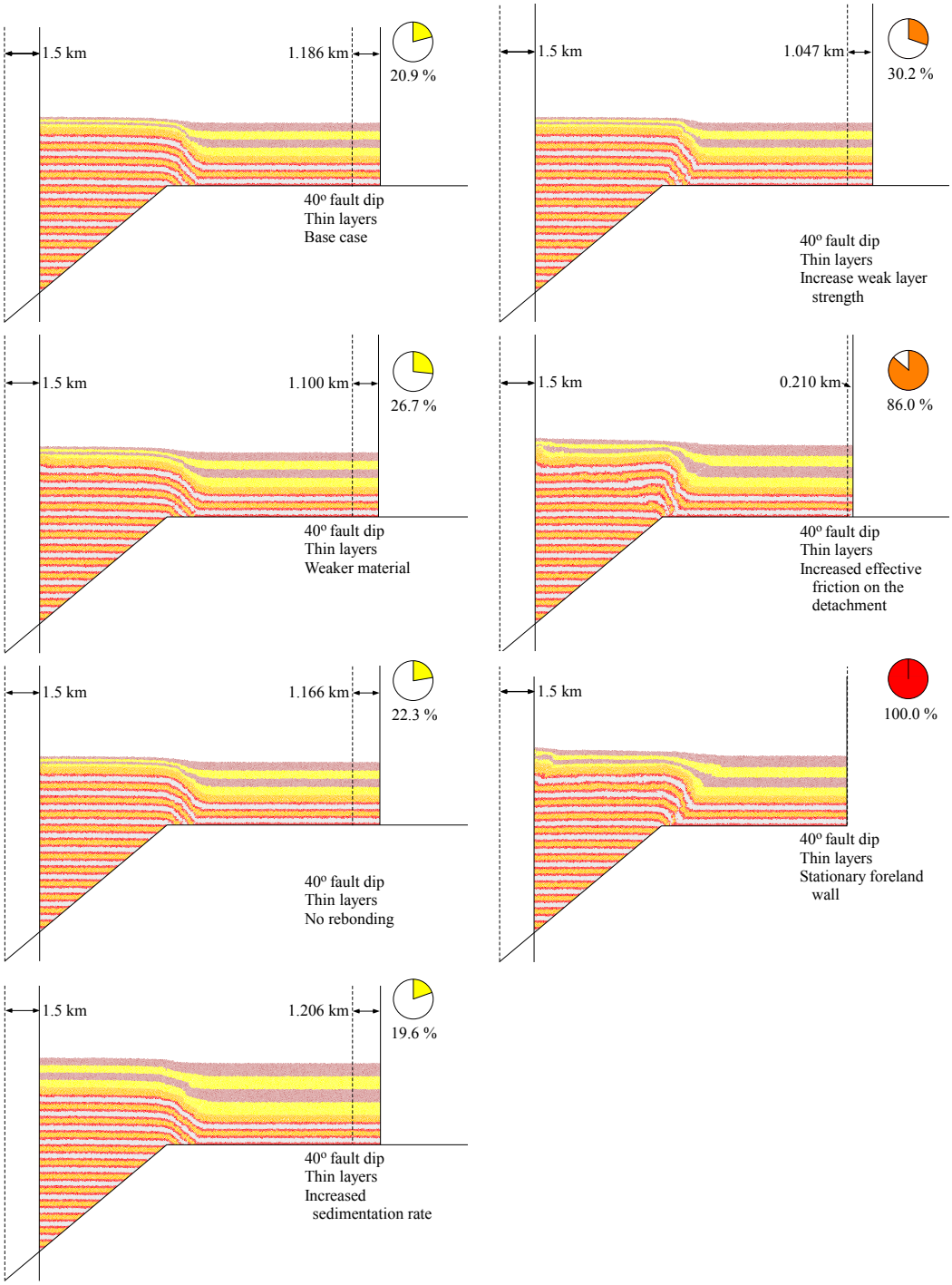


Figure A.11: Model results for 40° fault dip, thin mechanical layers. Annotation as described in Figure A.1.

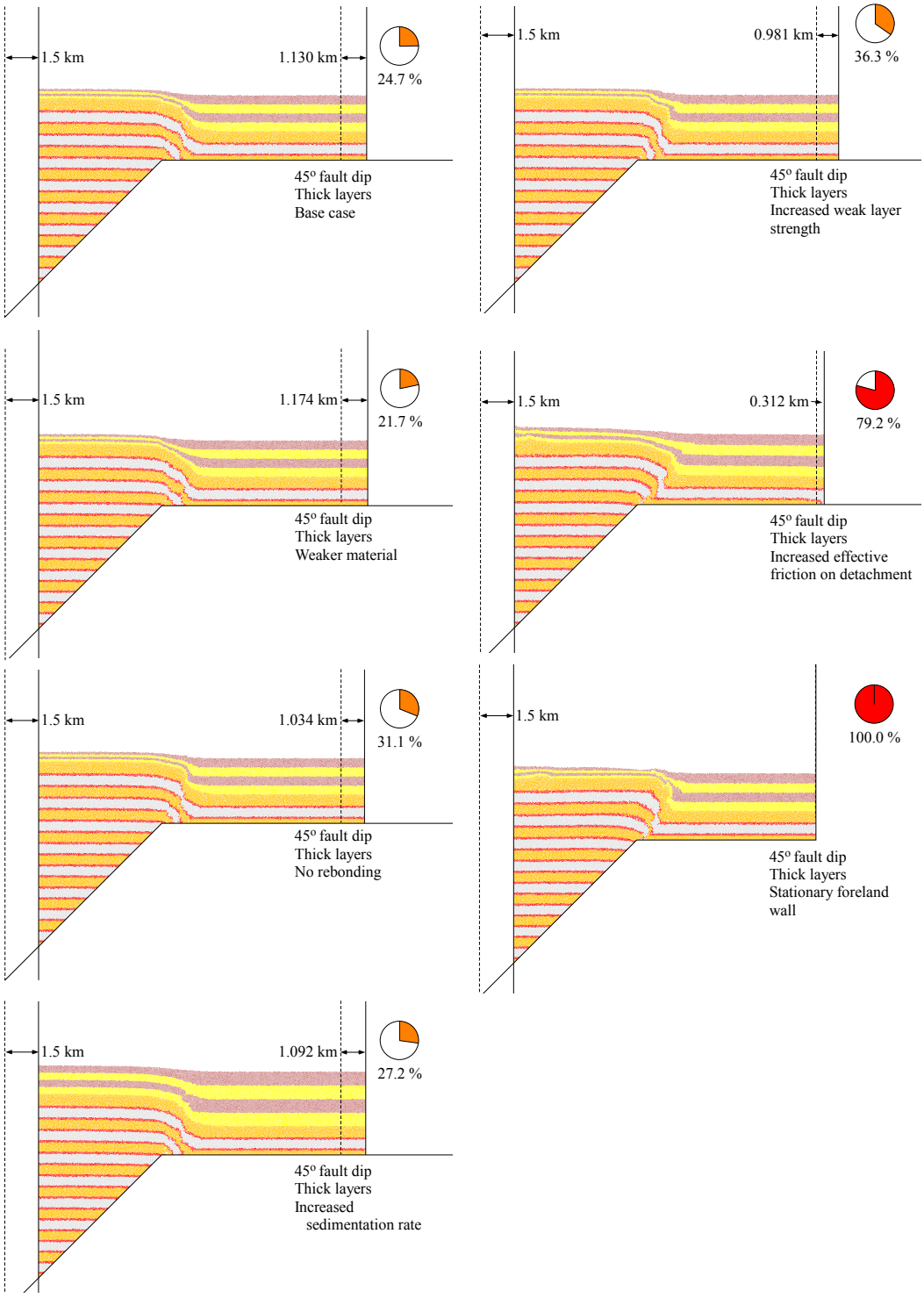


Figure A.12: Model results for 45° fault dip, thick mechanical layers. Annotation as described in Figure A.1.

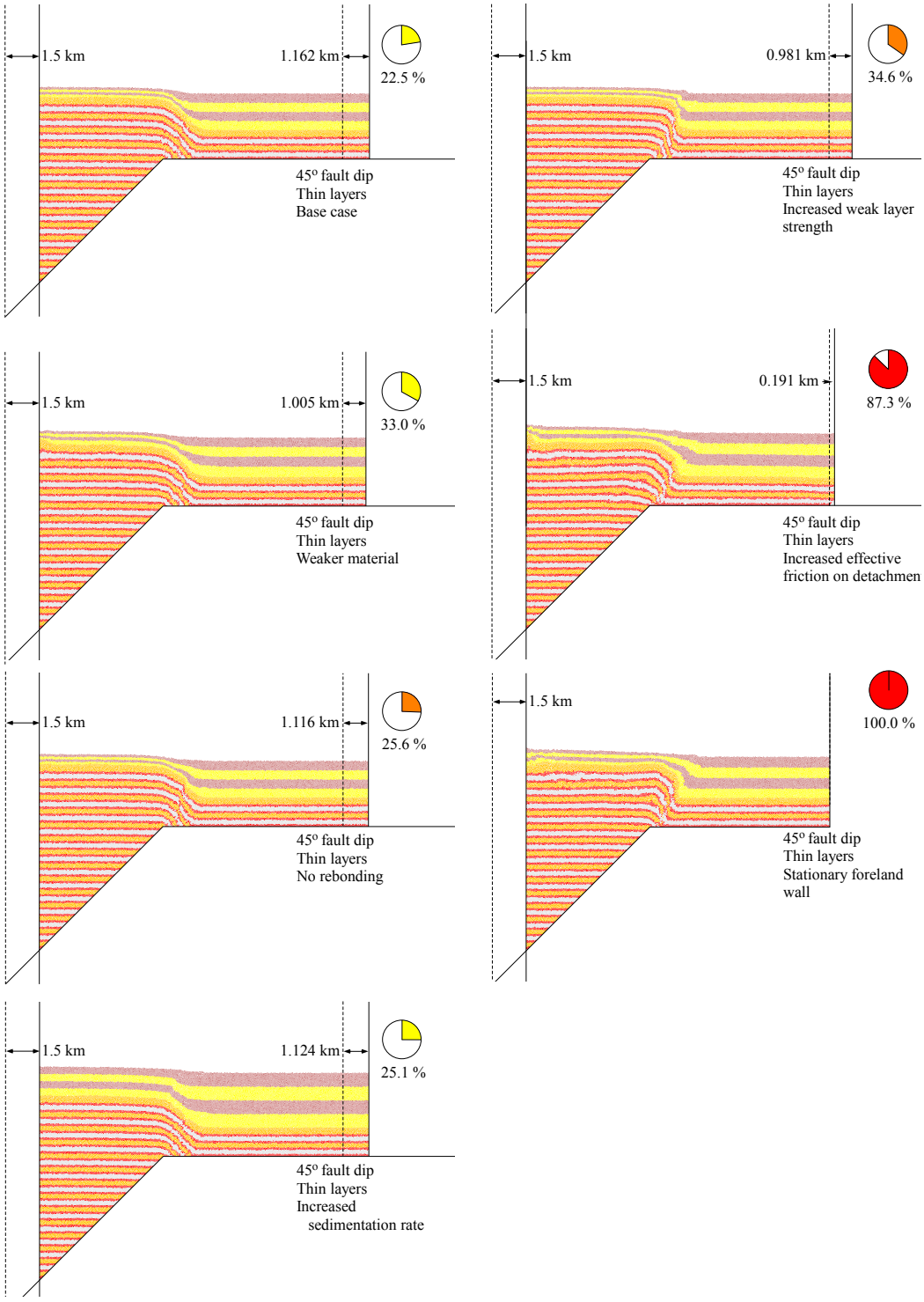


Figure A.13: Model results for 45° fault dip, thin mechanical layers. Annotation as described in Figure A.1.

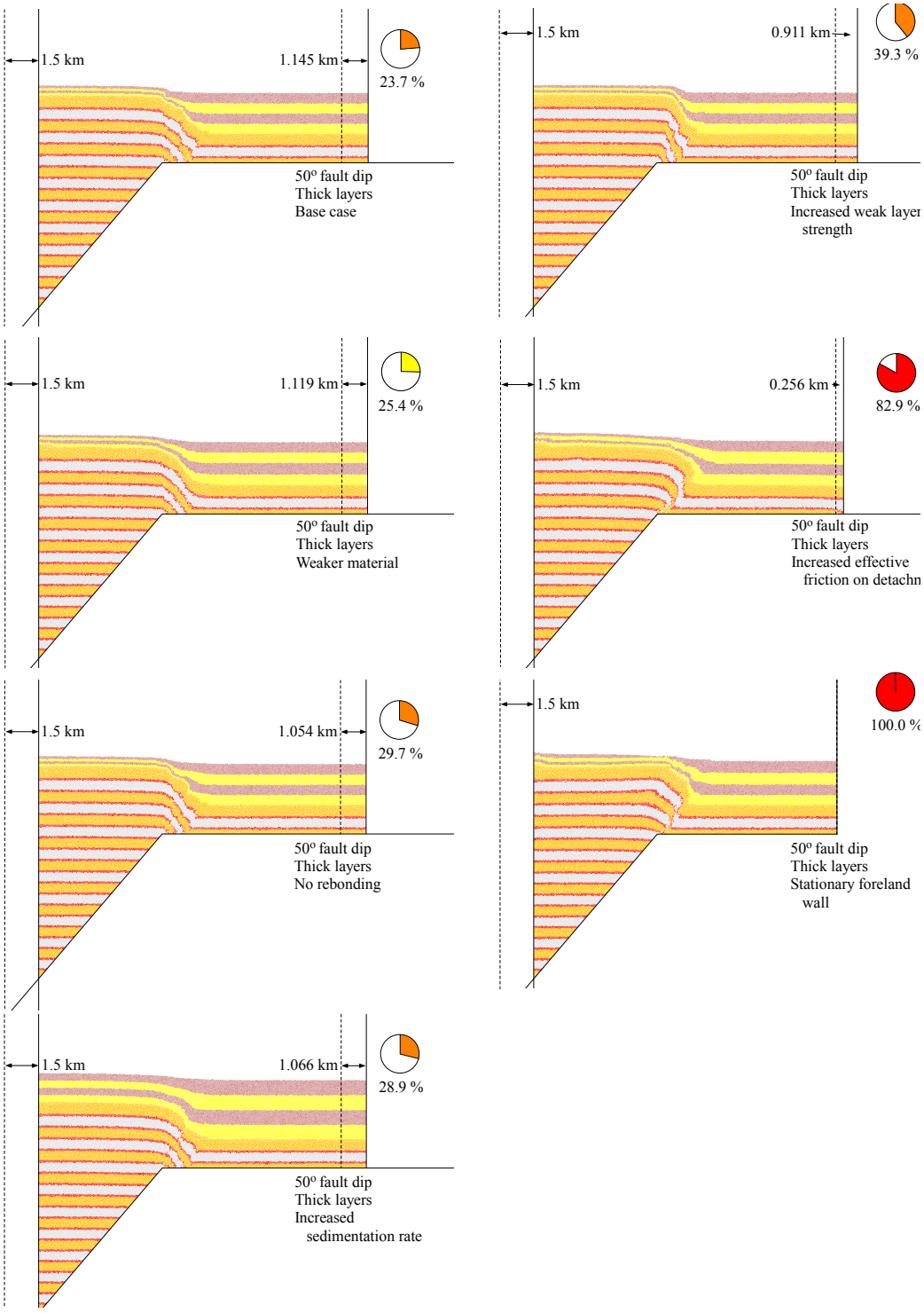


Figure A.14: Model results for 50° fault dip, thick mechanical layers. Annotation as described in Figure A.1.

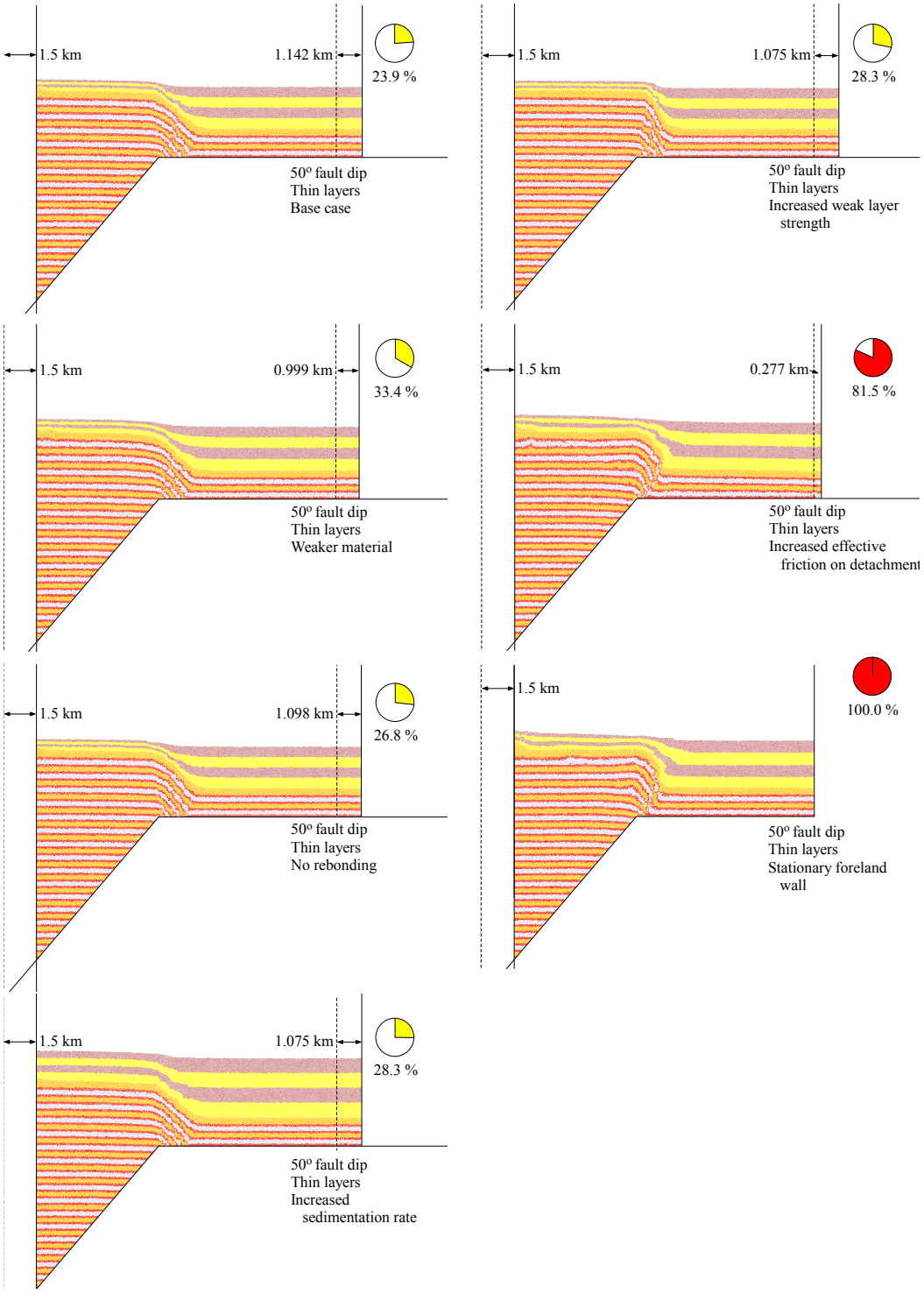


Figure A.15: Model results for 50° fault dip, thin mechanical layers. Annotation as described in Figure A.1.

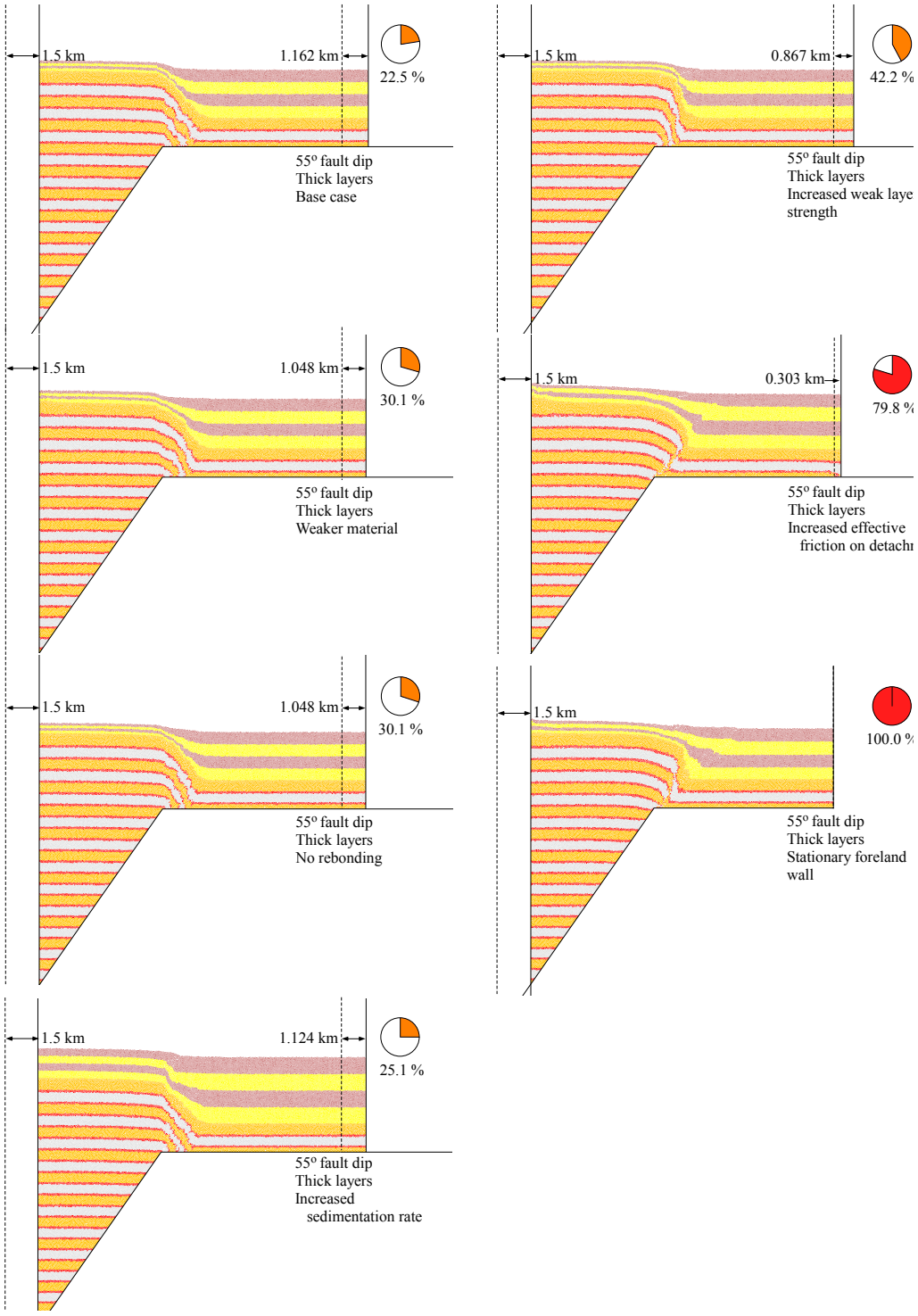


Figure A.16: Model results for 55° fault dip, thick mechanical layers. Annotation as described in Figure A.1.

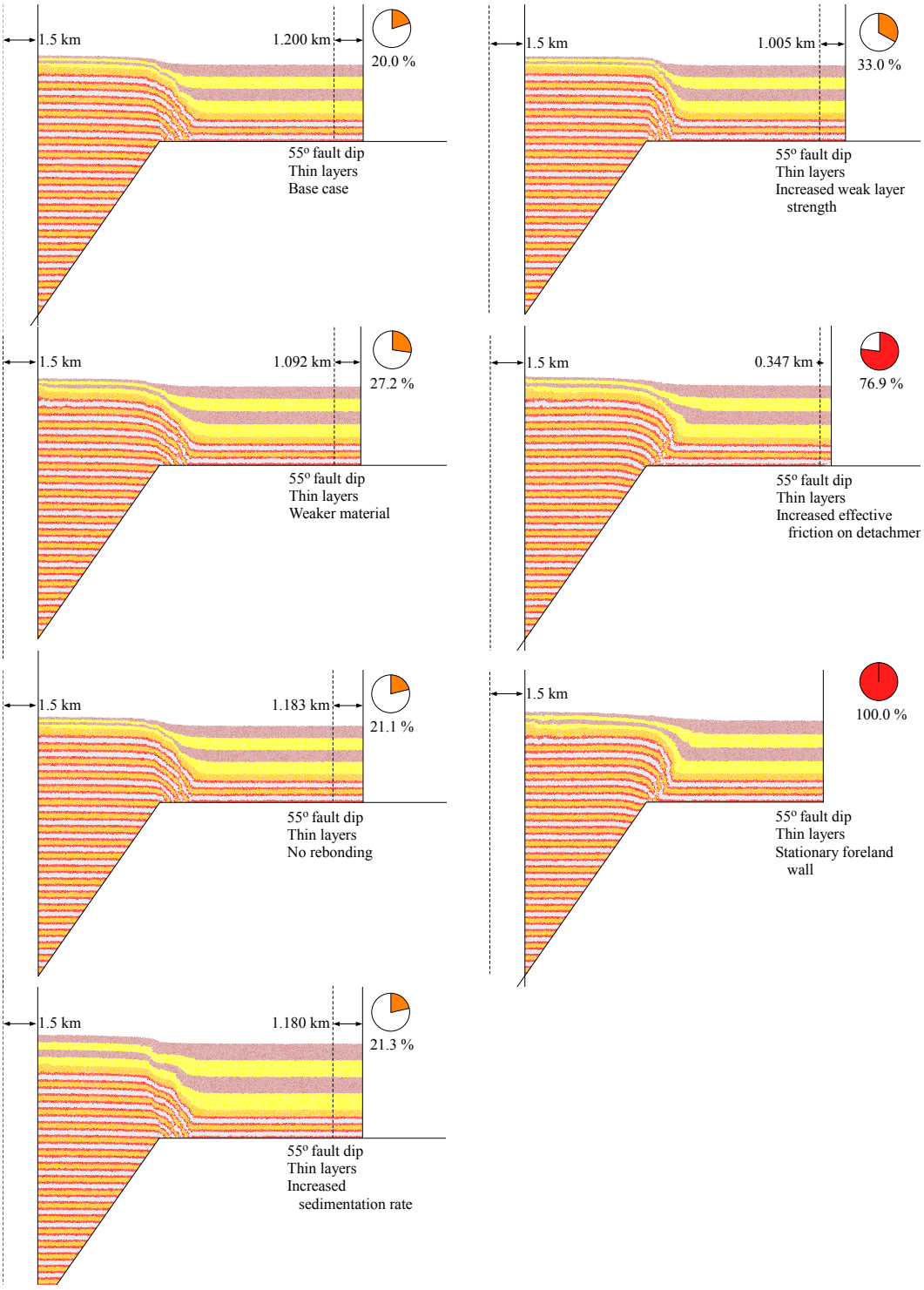


Figure A.17: Model results for 55° fault dip, thin mechanical layers. Annotation as described in Figure A.1.

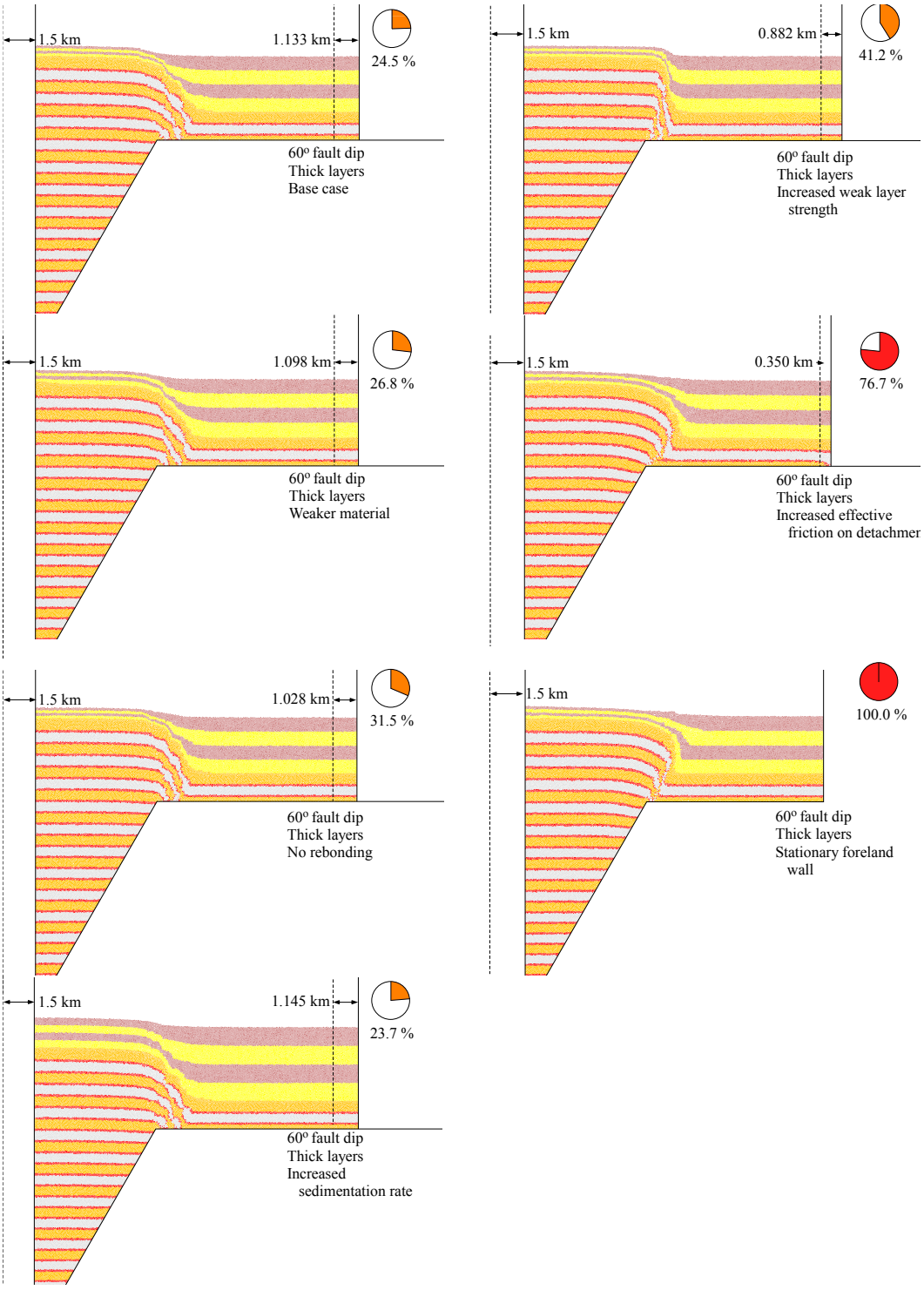


Figure A.18: Model results for 60° fault dip, thick mechanical layers. Annotation as described in Figure A.1.

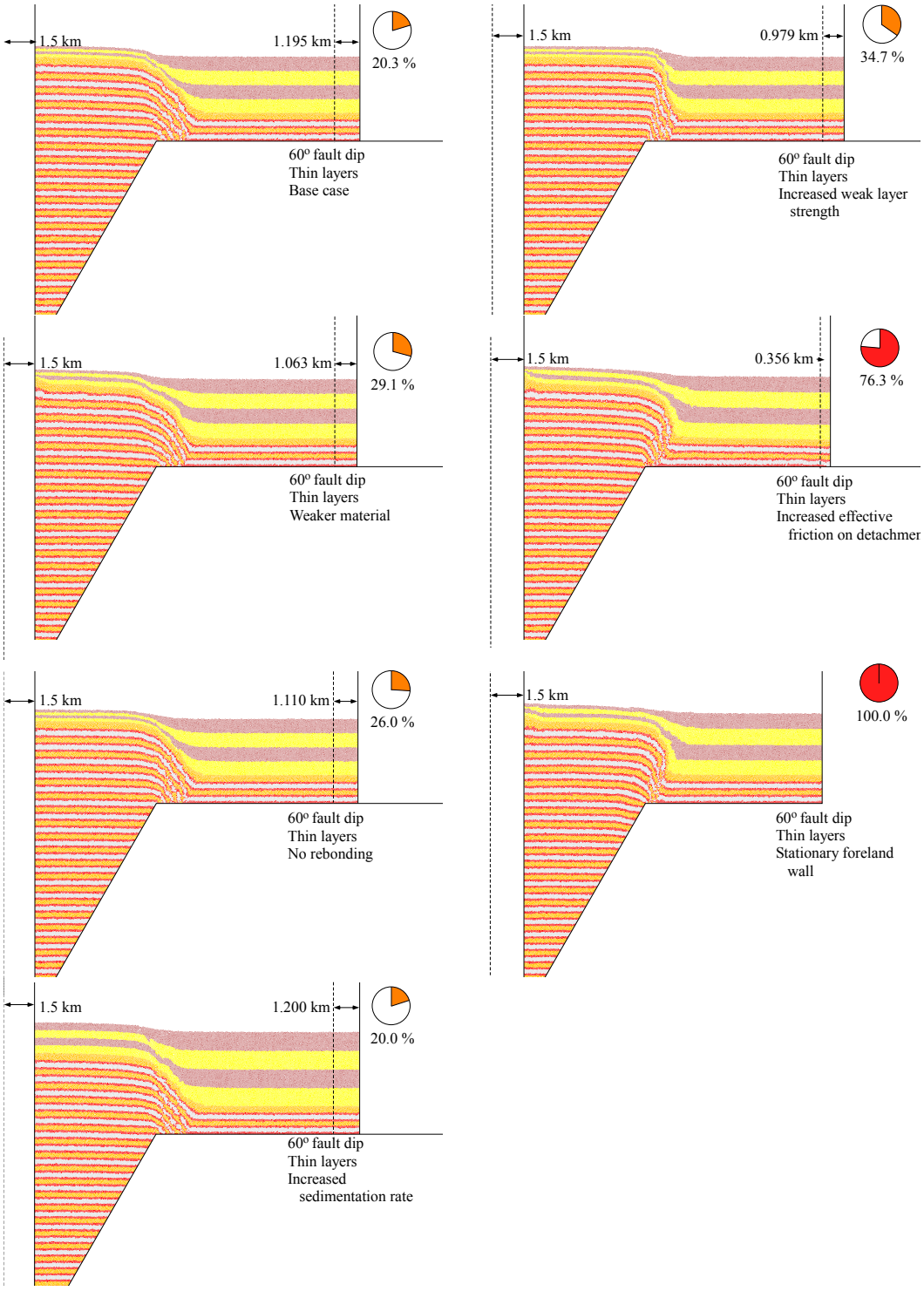


Figure A.19: Model results for 60° fault dip, thin mechanical layers. Annotation as described in Figure A.1.

| **20°<br>Thick Layers** | Shortening | % Def.<br>Int. | Limb<br>Dip | Disc.<br>Flt. | Active<br>A.S. | Notes | Code |
|---|---|---|---|---|---|---|---|
| Normal | 0.191 | 12.7% | 21 | no | anticlinal | fault-bend fold | 1 |
| Weaker | 0.219 | 14.6% | 19 | no | anticlinal | fault-bend fold | 1 |
| No rebonding | 0.183 | 12.2% | 22 | no | anticlinal | fault-bend fold | 1 |
| Increased<br>sedimentation rate | 0.189 | 12.6% | 22 | minor | mixed | fault-bend fold, wider limb | 1 |
| Increased weak<br>layer strength | 0.195 | 13.0% | 26 | no | anticlinal | fault-bend fold, more angular,<br>steeper limb | 1 |
| Increased eff.<br>friction on flat | 1.448 | 96.5% | – | minor | yes | asymmetric fold, minor break through,<br>defmn away from frontlimb | 5 |
| Stationary<br>foreland wall | 0 | 0.0% | – | minor | yes | asymmetric fold, minor break through,<br>defmn away from frontlimb | 5 |
| Kinematic model | 0.187 | 12.5% | 25 | minor | | | |

| **20°<br>Thin Layers** | Shortening | % Def.<br>Int. | Limb<br>Dip | Disc.<br>Flt. | Active<br>A.S. | Notes | Code |
|---|---|---|---|---|---|---|---|
| Normal | 0.235 | 15.7% | 23 | no | anticlinal | fault-bend fold | 1 |
| Weaker | 0.288 | 19.2% | 23 | no | anticlinal | fault-bend fold | 1 |
| No rebonding | 0.256 | 17.1% | 22 | no | anticlinal | fault-bend fold | 1 |
| Increased<br>sedimentation rate | 0.223 | 14.9% | 22 | no | anticlinal | fault-bend fold | 1 |
| Increased weak<br>layer strength | 0.256 | 17.1% | 30 | no | anticlinal | fault-bend fold | 1 |
| Increased eff.<br>friction on flat | 1.471 | 98.1% | – | no | mixed | distributed thickening,<br>discordant folding throughout hangingwall | 5 |
| Stationary<br>foreland wall | 1.5 | 100.0% | – | no | mixed | distributed thickening,<br>discordant folding throughout hangingwall | 5 |

Table A.1: Columns: 1. Model type; 2. Shortening (kilometers); 3. Percent shortening accommodated by internal model deformation (% Def. Int.); 4. Limb Dip (degrees); 5. Presence or Absence of discrete faulting (Disc. Flt.); 6. Which axial surface is active (Active A.S.); 7. Observations used to classify the structural style (Notes); and 8. the number corresponding to the structural style (Code), as described in Table A.10.

| **25°<br>Thick Layers** | Shortening | % Def.<br>Int. | Limb<br>Dip | Disc.<br>Flt. | Active<br>A.S. | Notes | Code |
|---|---|---|---|---|---|---|---|
| Normal | 0.209 | 13.9% | 27 | minor | anticlinal | fault-bend fold, very slight<br>discrete break at base of frontlimb | 1 |
| Weaker | 0.223 | 14.9% | 27 | no | anticlinal | fault-bend fold | 1 |
| No rebonding | 0.245 | 16.3% | – | minor | mixed | two limbs, shallow wide limb<br>toward hinterland, steep, narrow foreland | 1 |
| Increased<br>sedimentation rate | 0.221 | 14.7% | 27 | no | no | fault-bend fold | 1 |
| Increased weak<br>layer strength | 0.258 | 17.2% | 36 | minor | anticlinal | minor discrete faulting,<br>but general fault-bend fold shape | 1 |
| Increased eff.<br>friction on flat | 1.387 | 92.5% | – | yes | both | fault propagation fold,<br>breakthrough, active syncline | 4 |
| Stationary<br>foreland wall | 1.5 | 100.0% | – | minor | both | distributed uplifted<br>wedge in hanging wall | 5 |
| Kinematic model | 0.33 | 22.0% | 34 | | | | |
| **25°<br>Thin Layers** | Shortening | % Def.<br>Int. | Limb<br>Dip | Disc.<br>Flt. | Active<br>A.S. | Notes | Code |
| Normal | 0.247 | 16.5% | 32 | no | anticlinal | fault-bend fold | 1 |
| Weaker | 0.352 | 23.5% | 28 | no | anticlinal | fault-bend fold | 1 |
| No rebonding | 0.296 | 19.7% | 32 | no | anticlinal | fault-bend fold | 1 |
| Increased<br>sedimentation rate | 0.238 | 15.9% | 22 | no | no | fault-bend fold, wider,<br>gentler frontlimb | 1 |
| Increased weak<br>layer strength | 0.282 | 18.8% | 37 | no | anticlinal | fault-bend fold, steeper,<br>narrower frontlimb | 1 |
| Increased eff.<br>friction on flat | 1.401 | 93.4% | – | minor | mixed | steep frontlimb, significant<br>distributed deformation in hangingwall | 5 |
| Stationary<br>foreland wall | 1.5 | 100.0% | – | minor | synclinal | steep frontlimb, localized faulting,<br>but not from ramp, uplifted crest | 2 |

Table A.2: Twenty-Five Degrees. Columns as described in Table A.1.

| **30°<br>Thick Layers** | Shortening | % Def.<br>Int. | Limb<br>Dip | Disc.<br>Flt. | Active<br>A.S. | Notes | Code |
|---|---|---|---|---|---|---|---|
| Normal | 0.276 | 18.4% | 28 | minor | anticlinal | minor fault break through in<br>synclinal axial zone | 1 |
| Weaker | 0.294 | 19.6% | 30 | minor | anticlinal | minor fault break through in<br>anticlinal and synclinal axial zone | 1 |
| No rebonding | 0.281 | 18.7% | 30 | minor | both | more break through in syn and anti,<br>minor limb rot in synclinal growth | 2 |
| Increased<br>sedimentation rate | 0.294 | 19.6% | 28 | yes | anticlinal | localized faulting mid-frontlimb,<br>minor evidence of activity in growth | 2 |
| Increased weak<br>layer strength | 0.481 | 32.1% | 47 | yes | anticlinal | fault break through and<br>steep dip panel in syncline | 2 |
| Increased eff.<br>friction on flat | 1.326 | 88.4% | – | yes | synclinal | fault break through from ramp in syncline,<br>uplifted crest, steep frontlimb | 4 |
| Stationary<br>foreland wall | 1.5 | 100.0% | 37 | minor | both | some faulting, active syncline,<br>distributed thickening, less asym | 5 |
| Kinematic model | 0.63 | 42.0% | 60 | | | | |

| **30°<br>Thin Layers** | Shortening | % Def.<br>Int. | Limb<br>Dip | Disc.<br>Flt. | Active<br>A.S. | Notes | Code |
|---|---|---|---|---|---|---|---|
| Normal | 0.258 | 17.2% | 31 | no | anticlinal | fault-bend fold | 1 |
| Weaker | 0.42 | 28.0% | 30 | no | anticlinal | fault-bend fold | 1 |
| No rebonding | 0.302 | 20.1% | 33 | no | anticlinal | fault-bend fold | 1 |
| Increased<br>sedimentation rate | 0.314 | 20.9% | 33 | minor | mixed | fault-bend fold | 1 |
| Increased weak<br>layer strength | 0.478 | 31.9% | 50 | minor | mixed | thin, narrow frontlimb,<br>with minor break through mid-limb | 2 |
| Increased eff.<br>friction on flat | 1.344 | 89.6% | 66 | minor | both | steep, asymm front limb,<br>shallow backlimb, uplift, little discrete | 2 |
| Stationary<br>foreland wall | 1.5 | 100.0% | 80 | no | both | steep, asymm front limb, uplifted crest,<br>more asymmetric than above | 2 |

Table A.3: Thirty Degrees. Columns as described in Table A.1.

| **35°<br>Thick Layers** | Shortening | % Def.<br>Int. | Limb<br>Dip | Disc.<br>Flt. | Active<br>A.S. | Notes | Code |
|---|---|---|---|---|---|---|---|
| Normal | 0.366 | 24.4% | 34 | minor | mixed | two limbs separated by diffuse shear zone, varying thickness | 2 |
| Weaker | 0.346 | 23.1% | 42 | minor | anticlinal | rounded fold, very minor faulting, but continuous fold | 1 |
| No rebonding | 0.39 | 26.0% | 30 | no | anticlinal | very wide, shallow frontlimb | 1 |
| Increased sedimentation rate | 0.343 | 22.9% | 35 | minor | mixed | layer thickening in syncline, minor discrete faulting mid-limb | 2 |
| Increased weak layer strength | 0.501 | 33.4% | 63 | minor | mixed | narrow steep limb in foreland, minor shallow fold to hinterland | 2 |
| Increased eff. friction on flat | 1.252 | 83.5% | – | yes | synclinal | fault break through from ramp, active syncline | 4 |
| Stationary foreland wall | 1.5 | 100.0% | – | yes | synclinal | fault break through, more crestal uplift than above | 4 |
| **35°<br>Thin Layers** | Shortening | % Def.<br>Int. | Limb<br>Dip | Disc.<br>Flt. | Active<br>A.S. | Notes | Code |
| Normal | 0.355 | 23.7% | 33 | no | anticlinal | fault-bend fold | 1 |
| Weaker | 0.419 | 27.9% | 35 | no | anticlinal | fault-bend fold | 1 |
| No rebonding | 0.361 | 24.1% | 34 | no | anticlinal | fault-bend fold | 1 |
| Increased sedimentation rate | 0.323 | 21.5% | 32 | no | anticlinal | fault-bend fold | 1 |
| Increased weak layer strength | 0.486 | 32.4% | 46 | yes | mixed | steep, narrow frontlimb, locally faulted in syncline | 2 |
| Increased eff. friction on flat | 1.393 | 92.9% | – | minor | synclinal | asymmetric uplift, steep frontlimb, long, gentle back, limb rotation | 2 |
| Stationary foreland wall | 1.5 | 100.0% | – | minor | synclinal | gentler frontlimb, more asymmetry toward back, minor disc fault | 2 |

Table A.4: Thirty-Five Degrees. Columns as described in Table A.1.

| **40°<br>Thick Layers** | Shortening | % Def.<br>Int. | Limb<br>Dip | Disc.<br>Flt. | Active<br>A.S. | Notes | Code |
|---|---|---|---|---|---|---|---|
| Normal | 0.308 | 20.5% | – | minor | anticlinal | steep limb near syncline, shallower limb in anticline, minor faulting | 2 |
| Weaker | 0.341 | 22.7% | 36 | minor | anticlinal | localized faulting in syncline, limb rotation, two dip panels | 2 |
| No rebonding | 0.344 | 22.9% | – | minor | mixed | two dip panels, steep near syncline, gentle near anticline, limb rot. | 2 |
| Increased sedimentation rate | 0.329 | 21.9% | – | yes | anticlinal | fault breakthrough in syncline and mid-limb, active in early growth | 2 |
| Increased weak layer strength | 0.49 | 32.7% | – | minor | mixed | same two dip panels as above, but narrower and steeper than above | 2 |
| Increased eff. friction on flat | 1.249 | 83.3% | – | yes | synclinal | fault break from ramp, active syncline, limb rotation | 4 |
| Stationary foreland wall | 1.5 | 100.0% | – | yes | synclinal | fault break from ramp, active syncline, limb rot., rabbit-ear fold | 4 |
| **40°<br>Thin Layers** | Shortening | % Def.<br>Int. | Limb<br>Dip | Disc.<br>Flt. | Active<br>A.S. | Notes | Code |
| Normal | 0.314 | 20.9% | 45 | no | anticlinal | fault-bend fold | 1 |
| Weaker | 0.4 | 26.7% | 45 | no | anticlinal | fault-bend fold | 1 |
| No rebonding | 0.334 | 22.3% | 45 | no | anticlinal | fault-bend fold, slightly more rounded | 1 |
| Increased sedimentation rate | 0.294 | 19.6% | 38 | no | mixed | fault-bend fold, but evidence for mid-limb fault localization in growth | 2 |
| Increased weak layer strength | 0.453 | 30.2% | 53 | minor | anticlinal | more angular, steeper front limb | 1 |
| Increased eff. friction on flat | 1.29 | 86.0% | – | no | both | steep, irregular frontlimb, limb rotation, gently dipping backlimb, uplift | 2 |
| Stationary foreland wall | 1.5 | 100.0% | – | yes | synclinal | clear active syncline, fault break through from ramp, steep frontlimb | 4 |

Table A.5: Forty Degrees. Columns as described in Table A.1.

| **45°**<br>**Thick Layers** | Shortening | % Def.<br>Int. | Limb<br>Dip | Disc.<br>Flt. | Active<br>A.S. | Notes | Code |
|---|---|---|---|---|---|---|---|
| Normal | 0.37 | 24.7% | – | minor | mixed | localized shear in frontlimb,<br>strong layer thickness changes | 2 |
| Weaker | 0.326 | 21.7% | – | minor | mixed | localized layer thickness<br>changes, limb rotation | 2 |
| No rebonding | 0.466 | 31.1% | – | yes | syncline | localized fault breakthrough mid-limb,<br>strong layer thickness change | 2 |
| Increased<br>sedimentation rate | 0.408 | 27.2% | – | yes | mixed | localized faulting in frontlimb,<br>layer thickness changes | 2 |
| Increased weak<br>layer strength | 0.545 | 36.3% | 66 | minor | mixed | steep, narrow frontlimb, local<br>faulting and layer thickness changes | 2 |
| Increased eff.<br>friction on flat | 1.188 | 79.2% | – | yes | synclinal | fault-propagation fold, fault<br>prop from ramp, active syncline | 4 |
| Stationary<br>foreland wall | 1.5 | 100.0% | – | yes | synclinal | fault from ramp, active syn.,<br>rabbit ear fold along steep frontlimb | 4 |
| **45°**<br>**Thin Layers** | Shortening | % Def.<br>Int. | Limb<br>Dip | Disc.<br>Flt. | Active<br>A.S. | Notes | Code |
| Normal | 0.338 | 22.5% | 43 | no | anticlinal | fault-bend fold | 1 |
| Weaker | 0.495 | 33.0% | 46 | no | anticlinal | fault-bend fold | 1 |
| No rebonding | 0.384 | 25.6% | – | minor | mixed | localized faulting mid-front-limb,<br>limb rotation | 2 |
| Increased<br>sedimentation rate | 0.376 | 25.1% | 42 | minor | mixed | fault-bend fold, discrete<br>anticlinal a.s. in growth | 1 |
| Increased weak<br>layer strength | 0.519 | 34.6% | 74 | minor | mixed | very narrow, steep frontlimb,<br>some localized faulting and active syn. | 2 |
| Increased eff.<br>friction on flat | 1.309 | 87.3% | – | yes | syncline | fault prop up from ramp, active<br>syncline, fault-propagation fold | 4 |
| Stationary<br>foreland wall | 1.5 | 100.0% | – | yes | synclinal | same as above, but even more defined<br>discrete fault prop up from ramp | 4 |

Table A.6: Forty-Five Degrees. Columns as described in Table A.1.

| **50°<br>Thick Layers** | Shortening | % Def.<br>Int. | Limb<br>Dip | Disc.<br>Flt. | Active<br>A.S. | Notes | Code |
|---|---|---|---|---|---|---|---|
| Normal | 0.355 | 23.7% | 43 | minor | mixed | minor faulting in syncline and mid-limb,<br>local active syncline a.s. | 2 |
| Weaker | 0.381 | 25.4% | 49 | no | anticlinal | rounded-hinged fault-bend fold | 1 |
| No rebonding | 0.446 | 29.7% | 52 | minor | mixed | minor faulting in syncline and midlimb,<br>locally active synclinal a.s. | 2 |
| Increased<br>sedimentation rate | 0.434 | 28.9% | 50 | yes | mixed | discrete faulting in syncline and<br>mid-limb, local active syncline a.s. | 2 |
| Increased weak<br>layer strength | 0.589 | 39.3% | 61 | yes | mixed | discrete faulting in syncline and<br>mid-limb, local active syncline a.s. | 2 |
| Increased eff.<br>friction on flat | 1.244 | 82.9% | – | yes | synclinal | fault prop from ramp, active syncline,<br>very steep, rounded frontlimb | 4 |
| Stationary<br>foreland wall | 1.5 | 100.0% | – | yes | synclinal | more angular than above,<br>more offset on fault in the syncline | 4 |

| **50°<br>Thin Layers** | Shortening | % Def.<br>Int. | Limb<br>Dip | Disc.<br>Flt. | Active<br>A.S. | Notes | Code |
|---|---|---|---|---|---|---|---|
| Normal | 0.358 | 23.9% | 43 | minor | anticlinal | fault-bend fold | 1 |
| Weaker | 0.501 | 33.4% | 48 | minor | anticlinal | fault-bend fold, slightly steeper<br>and narrower limb than above | 1 |
| No rebonding | 0.402 | 26.8% | 45 | minor | anticlinal | fault-bend fold | 1 |
| Increased<br>sedimentation rate | 0.378 | 25.2% | 39 | yes | mixed | faulted and thinned frontlimb near<br>anticline, associated syncline | 1 |
| Increased weak<br>layer strength | 0.425 | 28.3% | 55 | minor | mixed | shallow limb near syncline, steep<br>limb near anticline, local faulting | 2 |
| Increased eff.<br>friction on flat | 1.223 | 81.5% | – | yes | syncline | fault prop up from ramp, active<br>syncline, rounded, steep frontlimb | 4 |
| Stationary<br>foreland wall | 1.5 | 100.0% | – | yes | synclinal | similar to above, but<br>narrower, steeper frontlimb | 4 |

Table A.7: Fifty Degrees. Columns as described in Table A.1.

| **55°**<br>**Thick Layers** | Shortening | % Def.<br>Int. | Limb<br>Dip | Disc.<br>Flt. | Active<br>A.S. | Notes | Code |
|---|---|---|---|---|---|---|---|
| Normal | 0.338 | 22.5% | 49 | minor | anticline | layer thickness changes and<br>localized faulting in frontlimb | 2 |
| Weaker | 0.44 | 29.3% | – | minor | anticline | steep, thinned limb near syncline,<br>gentler limb in anticline, rounded | 2 |
| No rebonding | 0.452 | 30.1% | – | minor | anticline | layer thickness changes, localized<br>faulting, more curved than above | 2 |
| Increased<br>sedimentation rate | 0.376 | 25.1% | 50 | yes | mixed | layer thickness changes, localized faulting | 2 |
| Increased weak<br>layer strength | 0.633 | 42.2% | 71 | minor | mixed | very steep frontlimb, very thinned<br>in middle, localized faulting | 2 |
| Increased eff.<br>friction on flat | 1.197 | 79.8% | – | yes | syncline | fault tied to ramp, prominent<br>active syncline, steep, rounded limb | 4 |
| Stationary<br>foreland wall | 1.5 | 100.0% | – | yes | syncline | fault break through tied to ramp,<br>similar to above but more angular | 4 |

| **55°**<br>**Thin Layers** | Shortening | % Def.<br>Int. | Limb<br>Dip | Disc.<br>Flt. | Active<br>A.S. | Notes | Code |
|---|---|---|---|---|---|---|---|
| Normal | 0.3 | 20.0% | 52 | minor | minor | minor faulting in frontlimb | 2 |
| Weaker | 0.408 | 27.2% | – | minor | no | minor faulting mid-frontlimb,<br>two limbs, steeper in syncline | 2 |
| No rebonding | 0.317 | 21.1% | – | minor | no | minor faulting mid-frontlimb,<br>two limbs, steeper in syncline | 2 |
| Increased<br>sedimentation rate | 0.32 | 21.3% | – | minor | minor | two limbs, layer thinning,<br>discontinuous faulting | 2 |
| Increased weak<br>layer strength | 0.495 | 33.0% | 62 | minor | minor | steep, thinned fronlimb, fault<br>localization, some limb rotation | 2 |
| Increased eff.<br>friction on flat | 1.153 | 76.9% | – | yes | yes | rounded fold, fault break<br>through, active syncline | 4 |
| Stationary<br>foreland wall | 1.5 | 100.0% | – | yes | yes | fault break through from ramp,<br>rounde fold, active syncline | 4 |

Table A.8: Fifty-Five Degrees. Columns as described in Table A.1.

| **60°<br>Thick Layers** | Shortening | % Def.<br>Int. | Limb<br>Dip | Disc.<br>Flt. | Active<br>A.S. | Notes | Code |
|---|---|---|---|---|---|---|---|
| Normal | 0.367 | 24.5% | – | yes | minor | multiple faults in frontlimb,<br>but overall fault-bend fold shape | 2 |
| Weaker | 0.402 | 26.8% | 51 | minor | minor | distributed faulting in fronlimb,<br>little localization | 2 |
| No rebonding | 0.472 | 31.5% | – | yes | minor | localized faulting and large layer<br>thickness changes in frontlimb | 2 |
| Increased<br>sedimentation rate | 0.355 | 23.7% | – | yes | minor | faulting and layer thickness<br>changes throughout frontlimb | 2 |
| Increased weak<br>layer strength | 0.618 | 41.2% | 74 | minor | minor | steep, thinned fronlimb, fault<br>localization, some limb rotation | 2 |
| Increased eff.<br>friction on flat | 1.15 | 76.7% | – | yes | yes | rounded fold, fault break<br>through, active syncline | 4 |
| Stationary<br>foreland wall | 1.5 | 100.0% | – | yes | yes | fault breakthrough throughout<br>pregrowth, rounded limb, active syn. | 4 |
| **60°<br>Thin Layers** | Shortening | % Def.<br>Int. | Limb<br>Dip | Disc.<br>Flt. | Active<br>A.S. | Notes | Code |
| Normal | 0.305 | 20.3% | 50 | minor | no | minor faulting and<br>thinning of frontlimb | 2 |
| Weaker | 0.437 | 29.1% | – | minor | minor | gentle limb near anticline, steep,<br>thinned limb near syncline | 2 |
| No rebonding | 0.39 | 26.0% | 51 | minor | no | minor faulting and<br>thinning of frontlimb | 2 |
| Increased<br>sedimentation rate | 0.3 | 20.0% | 46 | yes | yes | minor localized faulting and<br>layer thickness changes in limb | 2 |
| Increased weak<br>layer strength | 0.521 | 34.7% | 68 | minor | minor | highly thinned,<br>narrow, convex limb | 2 |
| Increased eff.<br>friction on flat | 1.144 | 76.3% | – | yes | yes | fault break up from ramp,<br>rounded fold | 4 |
| Stationary<br>foreland wall | 1.5 | 100.0% | – | yes | yes | fault break up from ramp,<br>less rounded than above | 4 |

Table A.9: Sixty Degrees. Columns as described in Table A.1.

| Classification | Code | Description |
|---|---|---|
| Fault-bend fold | 1 | active anticlinal axial surface, minor, uniform changes in layer thickness, no localized faulting significant displacement on upper detachment |
| Transitional structure | 2 | minor localized folding or faulting in frontlimb, variable layer thinning and thickening, locally active synclinal or anticlinal axial surface, some displacement on upper detachment also include structures in which an active anticlinal axial surface is observed, but little to no localized faulting in the frontlimb |
| Fault-propagation fold | 4 | active synclinal axial surface, fault propagating through frontlimb, little displacement on upper detachment |
| Other | 5 | significant deformation outside of front-limb area associated with slip on weak layers, resulting in distributed uplift and deformation |

Table A.10: Description of classification criteria for different fault-related folding styles.

# Bibliography


Albertz, M., Lingrey, S., Sanz, P., 2011. Critical state finite element models of contractional fault-related folding: Structural and mechanical analyses (Abs.). *American Geophysical Union*.

Allmendinger, R., 1998. Inverse and forward numerical modeling of trishear fault propagation folds. *Tectonics* 17 (4), 640–656.

Allmendinger, R., Shaw, J., 2000. Estimation of fault-propagation distance from fold shape: Implications for earthquake hazard assessment. *Geology* 28 (12), 1,099–1,102.

Antonellini, M., Pollard, D., 1995. Distinct element modeling of deformation bands in sandstone. *Journal of Structural Geology* 17, 1,165–1,182.

Armstrong, P., Bartley, J., 1993. Displacement and deformation associated with a lateral thrust termination, southern Golden Gate Range, southern Nevada, USA. *Journal of Structural Geology* 15 (6), 721–735.

Atwater, T., 1989. Plate Tectonic History of the northeast Pacific and western North America. *The Eastern Pacific Ocean and Hawaii*, Geological Society of America, Geology of North America Series, N, pp. 21–72.

Avbovbo, A., 1978. Tertiary lithostratigraphy of Niger Delta. *American Association of Petroleum Geologists Bulletin* 62 (2), 295–300.

Barazangi, M., Isacks, B., 1976. Spatial distribution of earthquakes and subduction of the Nazca plate beneath South America. *Geology* 4, 686–692.

Barrier, L., Nalpas, T., Gapais, D., Proust, J., Casas, A., Bourquin, S., 2002. Influence of syntectonic sedimentation on thrust geometry Field examples from the Iberian Chain (Spain) and analogue modelling. *Sedimentary Geology* 146, 91–104.

Benesh, N., 2010. *The Mechanics of Fault-bend folding and tear-fault systems in the Niger Delta*. Harvard University, Cambridge, MA, PhD Thesis.

Benesh, N., Plesch, A., Shaw, J., Frost, E., 2007. Investigation of growth fault bend folding using discrete element modeling: Implications for signatures of active folding above blind thrust faults. *Journal of Geophysical Research – Solid Earth* 112, B03S04.

Bergen, K., Shaw, J., 2010. Displacement profiles and displacement-length scaling relationships of thrust faults constrained by seismic reflection data. *Geological Society of America Bulletin* 122 (7-8), 1209–1219.

Berger, P., Johnson, A., 1980. First-order analysis of deformation of a thrust sheet moving over a ramp. *Tectonophysics* 70, T9–T24.

Bieniawski, Z., 1984. *Rock mechanics design in mining and tunnelling*. AA Balkema, The Netherlands.

Bilotti, F., Brickner, T., Elliott, T., Morgan, C., Readhead, R., 2005. Salt weld detached fault-propagation folds. *Seismic Interpretation of Contractional Fault-related folds*, AAPG Seismic Atlas, Studies in Geology 53 Edition, The American Association of Petroleum Geologists, Tulsa, Oklahoma, pp. 96–99.

Bilotti, F., Shaw, J., 2005. Deep-water Niger Delta fold and thrust belt modeled as a critical-taper wedge: The influence of elevated basal fluid pressure on structural styles. *American Association of Petroleum Geologists Bulletin* 89, 1475–1491.

Bonini, M., Sokoutis, D., Mulugeta, G., Katrivanos, E., 2000. Modelling hanging wall accommodation above rigid thrust ramps. *Journal of Structural Geology* 22, 1,165–1,179.

Briggs, S., Davies, R., Cartwright, J., Morgan, R., 2006. Multiple detachment levels and their control on fold styles in the compressional domain of the deepwater west Niger Delta. *Basin Research* 18 (4), 435–450.

Brun, J., Nalpas, T., 1996. Graben inversion in nature and experiments. *Tectonics* 15 (2), 677–687.

Burbridge, D., Braun, J., 2002. Numerical models of the evolution of accretionary wedges and fold-and-thrust belts using the distinct element method. *Geophysical Journal International* 148, 542–561.

Burchfiel, B., Zhiliang, C., Yuping, L., Royden, L., 1995. Tectonics of the Longmen Shan and adjacent regions, central China. *International Geology Review* 37, 661–735.

Byerlee, J., 1978. Friction of rocks. *Pure and Applied Geophysics* 116, 615–626.

Cardozo, N., Allmendinger, R., Morgan, J., 2005. Influence of mechanical stratigraphy and initial stress state on the formation of two fault-propagation folds. *Journal of Structural Geology* 27, 1,954–1,972.

Cardozo, N., Bhalla, K., Zehnder, A., Allmendinger, R., 2003. Mechanical models of fault propagation folds and comparison to the trishear kinematic model. *Journal of Structural Geology* 25, 1–18.

Carena, S., Suppe, J., 2002. Three-dimensional imaging of active structures using earthquake aftershocks: the Northridge thrust, California. *Journal of Structural Geology* 24, 887–904.

Chester, J., Chester, F., 1990. Fault-propagation folds above thrusts with constant dip. *Journal of Structural Geology* 12 (7), 903–910.

Chester, J., Logan, J., Spang, J., 1991. Influence of layering and boundary conditions on fault-bend and fault-propagation folding. *Geological Society of America Bulletin* 103, 1,059–1,072.

Connors, C., Denson, D., Kristiansen, G., Angstadt, D., 1998. Compressive anticlines of the mid-outer slope, central Niger Delta. *American Association of Petroleum Geologists Bulletin* 82 (10), 1,903.

Corredor, F., Shaw, J., Bilotti, F., 2005a. Structural styles in the deep-water fold and thrust belts of the Niger Delta. *American Association of Petroleum Geologists Bulletin* 89, 753–780.

Corredor, F., Shaw, J., Suppe, J., 2005b. Shear fault-bend fold, Deep-water Niger Delta . *Seismic Interpretation of Contractional Fault-related folds*, AAPG Seismic Atlas, Studies in Geology 53 Edition, The American Association of Petroleum Geologists, Tulsa, Oklahoma, pp. 87–92.

Cundall, P., Strack, O., 1979. A discrete numerical model for granular assemblies. *Geotechnique* 29, 47–65.

Dahlen, F., Suppe, J., Davis, D., 1984. Mechanics of fold-and-thrust belts and accretionary wedges: cohesive Coulomb theory. *Journal of Geophysical Research – Solid Earth* 89 (B12), 10,087–10,101.

Dahlstrom, C., 1970. Structural geology in the eastern margin of the Canadian Rocky Mountains. *Canadian Petroleum Geology Bulletin* 18, 332–406.

Dahlstrom, C., 1990. Geometric constraints derived from the law of conservation of volume and applied to evolutionary models for detachment folding. *American Association of Petroleum Geologists Bulletin* 74, 336–344.

Damuth, J., 1994. Neogene gravity teconics and depositional processes on the deep Niger-Delta continental margin. *Marine and Petroleum Geology* 11, 320–346.

Davis, D., Suppe, J., Dahlen, F., 1983. Mechanics of fold-and-thrust belts and accretionary wedges. *Journal of Geophysical Research – Solid Earth* 88 (B2), 1,153–1,178.

Demets, C., Gordon, R., Argus, D., Stein, S., 1990. Current plate motions. *Geophysical Journal International* 101, 425–478.

Dolan, J., Christofferson, S., Shaw, J., 2003. Recognition of paleoearthquakes on the Puente Hills blind thrust fault, California. *Science* 300, 115–118.

Doust, H., Omatsola, E., 1990. Niger Delta. *Divergent/Passive Margin Basins*, AAPG Memoir 48 Edition, The American Association of Petroleum Geologists, Tulsa, Oklahoma, pp. 201–238.

Ellis, M., Dunlap, W., 1988. Displacement variation along thrust faults: implications for the development of large faults . *Journal of Structural Geology* 10 (2), 188–192.

Ephard, J.-L., Groshong, R., 1995. Kinematic model of detachment folding including limb rotation, fixed hinges, and layer-parallel strain. *Tectonophysics* 247, 85–103.

Erickson, S., 1996. Influence of mechanical stratigraphy on folding vs faulting. *Journal of Structural Geology* 18 (4), 443–450.

Erickson, S., Strayer, L., Suppe, J., 2001. initiation and reactivation of faults during movement over a thrust-fault ramp: numerical mechanical models. *Journal of Structural Geology* 23, 11–23.

Erickson, S., Wiltschko, D., 1991. Spatially heterogeneous strength in thrust fault zones. *Journal of Geophysical Research – Solid Earth* 96 (B5), 8,427–8,439.

Erslev, E., 1991. Trishear fault-propagation folding. *Geology* 19, 617–620.

Erslev, E., Mayborn, K., 1997. Multiple geometries and modes of fault-propagation folding in the Canadian Rockies. *Journal of Structural Geology* 19 (3-4), 321–335.

Finch, E., Hardy, S., Gawthorpe, R., 2003. Discrete element modeling of contractional fault-propagation folding above rigid basement fault blocks. *Journal of Structural Geology* 25, 515–528.

Finch, E., Hardy, S., Gawthorpe, R., 2004. Discrete-element modeling of extensional fault-propagation folding above rigid basement fault blocks. *Basin Research* 16, 486–506.

Fischer, M., Jackson, P., 1999. Stratigraphic controls on deformation patterns in fault-related folds: a detachment fold example from the Sierra Madre Oriental, northeast Mexico. *Journal of Structural Geology* 21, 613–633.

Fischer, M., Woodward, N., Mitchell, M., 1992. The kinematics of break-thrust folds. *Journal of Structural Geology* 14 (4), 451–460.

Fox, F., 1959. Structure and accumulation of hydrocarbons in the southern foothills, Alberta, Canada. *American Association of Petroleum Geologists Bulletin* 43, 1–28.

Gillcrist, R., Coward, M., Mugnier, J., 1987. Structural inversion and its controls: examples from the Alpine foreland and French Alps. *Geodinamica Acta* 1 (1), 5–34.

Goff, D., Wiltschko, D., Fletcher, R., 1996. Decollement folding as a mechanism for thrust-ramp spacing. *Journal of Geophysical Research – Solid Earth* 101 (B5), 11,341–11,352.

Gold, R., Cowgill, E., Wang, X.-F., Chen, X.-H., 2006. Application of trishear fault-propagation folding to active reverse faults: examples from the Dalong fault, Gansu Province, NW China. *Journal of Structural Geology* 28, 200–219.

Guo, Y., Morgan, J., 2004. Influence of normal stress and grain shape on granular friction: Results of discrete element simulations. *Journal of Geophysical Research – Solid Earth* 109, B12305.

Harding, T., 1973. Newport-Inglewood trend, California–an example of wrenching style deformation. *American Association of Petroleum Geologists Bulletin* 57 (1), 97–116.

Harding, T., 1985. Seismic characteristics and identification of negative flower structures, positive flower structures, and positive structural inversion. *American Association of Petroleum Geologists Bulletin* 69 (4), 582–600.

Hardy, S., Finch, E., 2005. Discrete-element modelling of detachment folding. *Basin Research* 17, 507–520.

Hardy, S., Finch, E., 2006. Discrete element modelling of the influence of cover strength on basement-involved fault-propagation folding. *Tectonophysics* 415, 225–238.

Hardy, S., Finch, E., 2007. Mechanical stratigraphy and the transition from trishear to kink-band fault-propagation fold forms above blind basement thrust faults: A discrete-element study. *Marine and Petroleum Geology* 24, 75–90.

Hardy, S., McClay, K., Munoz, J., 2009. Deformation and fault activity in space and time in high-resolution numerical models of doubly vergent thrust wedges. *Marine and Petroleum Geology* 26, 232–248.

Hardy, S., Poblet, J., 2005. A method for relating fault geometry, slip rate and uplift data above fault-propagation folds. *Basin Research* 17, 417–424.

Hedlund, C., 1997. Fault-propagation, ductile strain, and displacement-distance relationships. *Journal of Structural Geology* 19 (3-4), 249–256.

Hedlund, C., Anastasio, D., Fisher, D., 1994. Kinematics of fault-related folding in a duplex, Lost River Range, Idaho, USA. *Journal of Structural Geology* 16 (4), 571–584.

Heim, A., 1919. *Geologie der Schweiz*. Tauchnitz, Liepzig, Germany.

Hill, R., 1967. *The Mathematical Theory of Plasticity*. Clarendon Press, Oxford, England.

Hubbard, J., Shaw, J., Klinger, Y., 2010. Structural setting of the 2008 Mw 79 Wenchuan, China Earthquake. *Bulletin of the Seismological Society of America* 100 (5B), 2713–2735.

Hubert-Ferrari, A., Suppe, J., Gonzales-Mieres, R., Wang, X., 2007. Mechanisms of active folding of the landscape. *Journal of Geophysical Research – Solid Earth* 112, B03S09.

Hughes, A., Shaw, J., 2012. Fault displacement-distance relationships as indicators of contractional fault-related folding style, to be published in AAPG Bulletin.

Hyndman, R., Hamilton, T., 1993. Queen Charlotte area Cenozoic tectonics and volcanism and their association with relative plate motions along the northeastern Pacific margin. *J. Geophys. Res.* 98, 14,257–14,277.

Hyndman, R., Spence, G., Yuan, T., Davis, E., 1994. Regional Geophysics and structural framework of the Vancouver Island margin accretionary prism. *Proceedings of the Ocean Drilling Program, Initial Reports*, Ocean Drilling Program, College Station, Texas, p. 609.

Itasca, 1999. *PFC2D: Theory and Background, User's Guide, Command Reference, FISH in PFC2D*. Itasca Consulting Group, Minneapolis, MN.

Jaeger, J., Cook, N., 1976. *Fundamentals of Rock Mechanics*, 2nd ed Edition. Chapman and Hall, London, England.

Jamison, W., 1987. Geometric analysis of fold development in overthrust terranes. *Journal of Structural Geology* 9 (2), 207–219.

Johnson, K., Johnson, A., 2002. Mechanical models of trishear-like folds. *Journal of Structural Geology* 24, 277–287.

Jordan, T., Allmendinger, R., 1986. The Sierras Pampeanas of Argentina: A modern analog of Rocky Mountain foreland deformation. *American Journal of Science* 286, 737–764.

Julian, F., Wiltschko, D., 1983. Deformation mechanisms in a terminating thrust anticline, Sequatchie Valley, Tennessee. *Geological Society of America Programs with Abstracts* 15, 606.

Kame, N., Rice, J., Dmowska, R., 2003. Effects of prestress state and rupture velocity on dynamic fault branching. *Journal of Geophysical Research – Solid Earth* 108 (B5), 2265.

Kanamori, H., 1977. The energy release in great earthquakes. *Journal of Geophysical Research – Solid Earth* 82, 2,981–2,987.

Kattenhorn, S., 1994. *Outcrop-scale fault-related folds, Valley and Ridge Province, Appalachians: Comparison to kinematic model predictions*. The University of Akron, Akron, Ohio, MS Thesis.

Kattenhorn, S., Pollard, D., 2001. Integrating 3-D seismic data, field analogs, and mechanical models in the analysis of segmented normal faults in the Wytch Farm oil field, southern England, United Kingdom. *American Association of Petroleum Geologists Bulletin* 85 (7), 1183–1210.

Kleyn, A., 1983. *Seismic Reflection Interpretation*. Applied Science Publishers, London, England.

Mansfield, C., Cartwright, J., 1996. High resolution fault displacement mapping from three-dimensional seismic data: evidence for dip linkage during fault growth. *Journal of Structural Geology* 18 (2-3), 249–263.

Masini, M., Bulnes, M., Poblet, J., 2010. Cross-section restoration: A tool to simulate deformation Application to a fault-propagation fold from the Cantabrian fold and thrust belt, NW Iberian Peninsula. *Journal of Structural Geology* 32, 172–183.

McClay, K., 1989. Analogue models of inversion tectonics. *Geological Society Special Publication*, 44 Edition, pp. 41–59.

McConnell, D., 1994. Fixed hinge, basement-involved fault-propagation folds, Wyoming. *Geological Society of America Bulletin* 106, 1583–1593.

McConnell, D., Kattenhorn, S., Benner, L., 1997. Distribution of fault slip in outcrop-scale fault-related folds, Appalachian Mountains. *Journal of Structural Geology* 19 (3-4), 257–267.

Meng, Q., Wang, E., Hu, J., 2005. Mesozoic sedimentary evolution of the northwest Sichuan Basin: Implication for continued clockwise rotation of the South China block. *Geological Society of America Bulletin* 117, 396–410.

Minster, J., Jordan, T., 1978. Present day plate motion. *J. Geophys. Res.* 83, 5331–5354.

Mitra, S., 1990. Fault-propagation folds: Geometry, kinematic evolution and hydrocarbon traps. *American Association of Petroleum Geologists Bulletin* 74, 921–945.

Mora, P., Place, D., 1993. A lattice solid model for the non-linear dynamics of earthquakes. *International Journal of Modern Physics* C(4), 1,059–1,074.

Mora, P., Place, D., 1994. Simulation of the frictional stick-slip instability. *Pure and Applied Geophysics* 143, 61–87.

Mora, P., Place, D., 1998. Numberical simulation of earthquake faults with gouge: toward a comprehensive explanation for the heat flow paradox. *Journal of Geophysical Research – Solid Earth* 103 (B9), 21,067–21,089.

Morgan, J., 1999. Numerical simulations of granular shear zones using the distinct element method 2 Effects of particle size distribution and interparticle friction on mechanical behavior. *Journal of Geophysical Research – Solid Earth* 104 (B2), 2,721–2,732.

Morgan, J., Boettcher, M., 1999. Numerical simulations of granular shear zones using the distinct element method 1 Shear zone kinematics and the micromechanics of localization. *Journal of Geophysical Research – Solid Earth* 104 (B2), 2,703–2,719.

Morgan, J., McGovern, P., 2005a. Discrete element simulations of gravitational volcanic deformation 2 Mechanical analysis . *Journal of Geophysical Research – Solid Earth* 110, B05403.

Morgan, J., McGovern, P., 2005b. Discrete element simulations of gravitational volcanic deformation: deformation structures and geometries. *Journal of Geophysical Research – Solid Earth* 110, B05402.

Morley, C., 1986. Vertical strain variations in the Osen-Roa thrust sheet, Northwestern Oslo fjord, Norway. *Journal of Structural Geology* 8 (6), 621–632.

Mosar, J., Suppe, J., 1992. Role of shear in fault-propagation folding. *Thrust Tectonics*, Chapman and Hall, London, England, pp. 123–132.

Muraoka, H., Kamata, H., 1983. Displacement distribution along minor fault traces. *Journal of Structural Geology* 5 (5), 483–495.

Narr, W., Suppe, J., 1994. Kinematics of basement-involved compressive structures. *American Journal of Science* 294, 802–860.

Poblet, J., Lisle, R., 2011. *Kinematic evolution and structural styles of fold-and-thrust belts*, Vol 349 Edition. Geological Society, London, Special Publications, London, England.

Poblet, J., McClay, K., Storti, F., Munoz, J., 1997. Geometries of syntectonic sediments associated with single layer detachment folds. *Journal of Structural Geology* 19, 369–381.

Pratt, T., Shaw, J., Dolan, J., Christofferson, S., Williams, R., Odum, J., Plesch, A., 2002. Shallow seismic imaging of folds above the Puente Hills blind-thrust fault, Los Angeles, California . *Geophys. Res. Lett.* 29 (9), 1304.

Rich, J., 1934. Mechanics of low-angle overthrust faulting as illustrated by Cumberland thrust block, Viginia, Kentucky, and Tennessee. *American Association of Petroleum Geologists Bulletin* 18, 1584–1596.

Riddihough, R., 1984. Recent movements of the Juan de Fuca plate system. *J. Geophys. Res.* 89, 6,980–6,994.

Rodgers, J., 1950. Mechanics of Appalachian folding as illustrated by Sequatchie anticline, Tennessee and Alabama. *American Association of Petroleum Geologists Bulletin* 34, 672–681.

Rodgers, J., 1990. Fold-and-thrust belts in sedimentary rocks Part 1: Typical examples. *American Journal of Science* 290, 321–359.

Rodgers, J., 1991. Fold-and-thrust belts in sedimentary rocks Part 22: Other examples, especially variants. *American Journal of Science* 291, 825–886.

Roering, J., Cooke, M., Pollard, D., 1997. Why blind thrust faults do not propagate to the Earth's surface: Numerical modeling of coseismic deformation associated with thrust-related anticlines. *Journal of Geophysical Research – Solid Earth* 102 (B6), 11,901–11,912.

Rowan, J., Ratliff, R., 1988. Use of fault cut-offs and bed travel distance in balanced cross-sections: Discussion 1. *Journal of Structural Geology* 10 (3), 311–316.

Rowan, M., Linares, R., 2009. Fold-evolution matrices and axial-surface analysis of fault-bend folds: Application to the Medina anticline, Eastern Cordillera, Colombia. *American Association of Petroleum Geologists Bulletin* 84 (6), 741–764.

Royden, L., Burchfiel, B., King, R., Wang, E., Chen, Z., Shen, F., Liu, Y., 1997. Surface deformation and lower crustal flow in eastern Tibet. *Science* 276, 788–790.

Saltzer, S., Pollard, D., 1992. Distinct element modelling of structures formed in sedimentary overburden by extensional reactivation of basement normal faults. *Tectonics* 11, 165–174.

Salvini, F., Storti, F., 2001. Distribution of deformation in parallel fault-related folds with migrating axial surfaces: comparison between fault-propagation and fault-bend folding. *Journal of Structural Geology* 23, 25–32.

Serafim, J., Pereira, J., 1983. Considerations on the geomechanical classification of Beniawski. *International symposium on engineering geology and underground construction* Lisbon, Portugal, II33–42.

Seyferth, M., Henk, A., 2006. A numerical sandbox: high-resolution distinct element models of halfgraben formation. *International Journal of Earth Sciences* 95, 189–203.

Shaw, J., Bilotti, F., Brennan, P., 1999. Patterns of imbricate thrusting. *Geological Society of America Bulletin* 111 (8), 1,140–1,154.

Shaw, J., Connors, C., Suppe, J., 2005. *Seismic Interpretation of Contractional Fault-related Folds*, AAPG Seismic Atlas, Studies in Geology 53 Edition. American Association of Petroleum Geologists, Tulsa, Oklahoma.

Shaw, J., Novoa, E., Connors, C., 2004. Structural controls on growth stratigraphy in contractional fault-related folds. *Thrust Tectonics and Hydrocarbon Systems*, AAPG Memoir 82 Edition, American Association of Petroleum Geologists, pp. 400–412.

Shaw, J., Plesch, A., Dolan, J., Pratt, T., Fiore, P., 2002. Puente Hills blind-thrust system, Los Angeles, California. *Bulletin of the Seismological Society of America* 92 (8), 2,946–2960.

Shaw, J., Suppe, J., 1994. Active faulting and growth folding in the eastern Santa Barbara Channel, California. *Geological Society of America Bulletin* 106, 607–626.

Sherriff, R., 1977. Limitations on resolution of seismic reflections and geologic detail derivable from them. *Seismic Stratigraphy–Applications to Hydrocarbon Exploration*, AAPG Memoir 26 Edition, American Association of Petroleum Geologists, p. xxx.

Smart, K., Krieg, R., Dunne, W., 1999. Deformation behavior during blind thrust translation as a function of fault strength. *Journal of Structural Geology* 21, 855–874.

Spang, J., McConnell, D., 1997. Effect of initial fault geometry on the development of fixed-hinge, fault-propagation folds. *Journal of Structural Geology* 19 (12), 1,537–1,541.

Spratt, D., Dixon, J., Beattie, E., 2004. Changes in structural style controlled by lithofacies contrast across transverse carbonate bank margins–Canadian Rocky Mountains and scaled physical models. *Thrust Tectonics and Hydrocarbon Systems*, AAPG Memoir 82 Edition, American Association of Petroleum Geologists, pp. 259–273.

Storti, F., Poblet, J., 1997. Growth stratal architectures associated to decollement folds and fault-propagation folds Inferences on fold kinematics. *Tectonophysics* 282, 353–373.

Strayer, L., Erickson, S., Suppe, J., 2004. Influence of growth strata on the evolution of fault-related folds–Distinct-element models. *Thrust Tectonics and Hydrocarbon Systems*, AAPG Memoir 82 Edition, American Association of Petroleum Geologists, pp. 413–437.

Strayer, L., Suppe, J., 2002. Out-of-plane motion of a thrust sheet during along-strike propagation of a thrust ramp: a distinct element approach. *Journal of Structural Geology* 24, 637–650.

Suppe, J., 1983. Geometry and kinematics of fault-bend folding. *American Journal of Science* 283, 684–721.

Suppe, J., 1985. *Principles of structural geology*. Prentice hall, New Jersey.

Suppe, J., Chou, G., Hook, S., 1992. Rates of folding and faulting determined from growth strata. *Thrust Tectonics*, Chapman and Hall, London, England, pp. 105–121.

Suppe, J., Connors, C., Zhang, Y., 2004. Shear fault-bend folding. *Thrust Tectonics and Hydrocarbon Systems*, AAPG Memoir 82 Edition, American Association of Petroleum Geologists, pp. 303–323.

Suppe, J., Medwedeff, D., 1984. Fault-propagation folding (Abs.). *Geological Society of America* 16, 670.

Suppe, J., Medwedeff, D., 1990. Geometry and kinematics of fault-propagation folding. *Eclogae Geologicae Helvetiae* 83, 409–454.

Tavani, S., Storti, F., Salvini, F., 2005. Rounding hinges to fault-bend folding: geometric and kinematic implications. *Journal of Structural Geology* 27, 3–22.

Tavani, S., Storti, F., Salvini, F., 2006. Double-edge fault-propagation folding: geometry and kinematics. *Journal of Structural Geology* 28, 19–35.

Thorbjornsen, K., Dunne, W., 1997. Origin of a thrust-related fold: Geometric vs kinematic tests. *Journal of Structural Geology* 19, 303–319.

Wells, D., Coppersmith, K., 1994. New empirical relationships among magnitude, rupture length, rupture width, rupture area, and surface displacement. *Bulletin of the Seismological Society of America* 84, 974–1,002.

Wickham, J., 1995. Fault displacement-gradient folds and the structure at Lost Hills, California (USA). *Journal of Structural Geology* 17 (9), 1,293–1,302.

Williams, G., Chapman, T., 1983. Strains developed in the hanging-walls of thrusts due to their slip/propagation rate: a dislocation model. *Journal of Structural Geology* 5 (6), 563–571.

Willis, B., Willis, R., 1934. *Geologic Structures*. McGraw-Hill, New York, NY.

Wiltschko, D., 1979a. A mechanical model for thrust sheet deformation at a ramp. *J. Geophys. Res.* 84, 1,091–1,104.

Wiltschko, D., 1979b. Partitioning of energy in a thrust sheet and implications concerning driving force. *J. Geophys. Res.* 84, 6,050–6,058.

Woodward, N., Rutherford Jr, E., 1989. Structural lithic units in external orogenic zones. *Deformation of Crustal Rocks*, 158 Edition, Tectonophysics, pp. 247–267.

Woodward, N., Walker, K., CT, L., 1988. Relationships between early Paleozoic facies patterns and structural trens in the Saltville thrust family, Tennessee Valley and Ridge, southern Appalachians. *Geological Society of America Bulletin* 100, 1,758–1,769.

Wu, J., McClay, K., 2011. Two-dimensional analog modeling of fold and thrust belts: Dynamic interactions with syncontractional sedimentation and erosion. *Thrust fault-related folding*, AAPG Memoir 94 Edition, American Association of Petroleum Geologists, pp. 301–333.

Wu, S., Bally, A., 2000. Slope tectonics; comparisons and contrasts of structural styles of salt and shale tectonics of the northern Gulf of Mexico with shale tectonics of offshore Nigeria in Gulf of Guinea. *Atlantic Rifts and Continental Margins*, Geophysical Monograph 115 Edition, American Geophysical Union, pp. 151–172.

Yue, L.-F., Suppe, J., Hung, J.-H., 2005. Structural geology of a classic thrust belt earthquake: the 1999 Chi-Chi earthquake Taiwan (Mw=76). *Journal of Structural Geology* 27, 2,058–2,083.

Zapata, T., Allmendinger, R., 1996. Growth stratal records of instantaneous and progressive limb rotation in the Precordillera thrust belt and Bermejo basin, Argentina. *Tectonics* 15 (5).